Fabrication and Characterization of ZnO and GaN Devices for Electronic and Photonic Applications

by

Fei Tong

A dissertation submitted to the Graduate Faculty of
Auburn University
in partial fulfillment of the
requirements for the Degree of
Doctor of Philosophy

Auburn, Alabama
December 14, 2013

Keywords: ZnO nanorods, Photovoltaics, Conjugated Polymer, AlGaN/GaN HEMT

Approved by

Minseo Park, Chair, Professor of Physics
Sarit Dhar, Assistant Professor of Physics
Michael Hamilton, Assistant Professor of Electrical and Computer Engineering

Abstract

The research work presented in this dissertation is based on two direct and wide band gap semiconductors: ZnO and GaN. On the first part of the dissertation, the synthesis of ZnO nanorod array via the low temperature solution growth method on flexible In_2O_3-PET and rigid ITO-glass substrates were discussed. The analysis of the morphology, crystal quality, and optical property of ZnO nanorods synthesized with the solution growth process were investigated. Due to the high surface-to-volume ratio of ZnO nanorod, to alleviate the some of the drawbacks such as carrier mobility and thickness dilemma of organic solar cells, ZnO nanorod array were integrated into organic solar cells. In this ZnO nanorod array integrated bulk heterojunction organic solar cells, ZnO nanorods play an important role in rapid collecting and transporting charge carriers. Power conversion efficiency (η) of 1.8% is achieved in our ZnO nanorods integrated bulk heterojunction organic solar cells on flexible In_2O_3-PET substrates.

On the second part of the dissertation, Aluminum gallium nitride/gallium nitride high electron mobility transistors (AlGaN/GaN HEMTs) were fabricated. RoundHEMT technology, which greatly simplifies the microelectronic fabrication process compared to traditional open fingers HEMT, was employed. Device testing and characterization under both room temperature and high temperature up to 300 °C were performed. The results show that the device can operate even at 300 °C with minimal degradation. Moreover, we propose a simple and novel spectroscopic photo I-V method of diagnosing the homogeneity of electrically-active defect distribution in the large area AlGaN/GaN HEMT epi structure grown on 6" silicon wafers.

Acknowledgments

The author would like to give her deepest appreciation to Prof. Minseo Park for his guidance, advice and support through the entire research work during her Ph.D. period at Auburn University. The author also would like to give thanks to the committee members, Dr.Sarit Dhar, Dr. Michael Hamilton and Dr. Helen Koo for their participation in evaluating the work.

Additionally, the author would like to thank Dr. Claude Ahyi for his kind help and discussion every time. Thanks to Tamara Isaacs-Smith for her training in microelectronics fabrication and assistance with the experimental setups. Thanks to Dr. Dong-Joo Kim for using his lab and equipment at Material Engineering Department. Thanks to Dr. Yaqi Wang, for his training on Raman and Photoluminescence (PL) measurements. Thanks to Dr. Zengjun Chen and Dr. Mingyu Li for discussion of problems met in device fabrication procedures.

The author would also like to thank Korea Institute of Industrial Technology (KITECH) for financial support, thank Sungkoo Lee, Eunhee Lim and Kyeong K. Lee from KITECH.

In addition, the author would like to thank Dr. Hui Xu, Dr. Siddharth Alur, and Dr. Resham Thapa, Mr. Kyusang Kim, Dr. Yogesh Sharma, Mr. Aaron Modic, Dr. Hosang Ahn, and Ms. Hyejin Park for discussion of the problems encountered in the research.

Finally the author would like to thank her parents, Yuxiang Tong and Huili Wang for their continuous love and support.

Table of Contents

List of Tables

List of Figures

List of Abbreviations

BHJ	Bulk Heterojunction
CCD	Charged Coupled Detector
C-V	Capacitance Voltage
FWHM	Full Width at Half Maximum
I-V	Current-Voltage
LED	Light Emitting Diode
HEMT	High Electron Mobility Transistor
P3HT	Poly (3-hexylthiophene-2,5-diyl)
PCBM	(6,6)-phenyl C61 butyric acid methyl ester
PCE	Power Conversion Efficiency
PL	Photoluminescence
RF	Radio Frequency
RPM	Revolutions per Minute
RTA	Rapid Thermal Annealing
TCE	Trichloroethylene
UV	Ultra-Violet
WBG	Wide Band Gap
XRD	X-ray diffraction

CHAPTER 1

Introduction

1.1 Organic-Inorganic Hybrid Solar Cells - The Big Picture

In the application of sunlight energy transfer, inorganic semiconductor, such as Si, has been vastly used in the fabrication of photovoltaic devices. Although the inorganic solar cell technology is relatively mature and has yield a power conversion efficiency larger than 10%, it still suffer the one of the big drawbacks - high cost. To solve this issue, a great attention has been paid to the organic solar cells which also have many other advantages besides being cheaper.

Organic solar cells, which offer the advantage of flexibility, light weight, and tunable band gap is very promising in the applications of sunlight energy conversion. However, there are also drawbacks in organic solar cell technology such as thickness dilemma, life time issues, exciton loss and carrier charge loss. Researchers worldwide discover that by introducing in the inorganic nanomaterial semiconductor, which will greatly help in the charge collection, transportation and device stability.

In this work, the nanomaterial that we have introduced into the organic solar cells is ZnO nanorods. And in this chapter, to understand how ZnO nanorod arrays can improve the organic PVs, we will first discuss how organic solar cells work, then we will discuss the development of inorganic-organic solar cells and the synthesis of organic solar cells.

1.2 ZnO Nanorods for Photovoltaic Application

1.2.1 Organic Solar Cells

Although inorganic crystalline semiconductor based solar cell technology such as Si solar cells has become relatively mature, it still suffers from a relatively high cost originated from the consumption of high quality silicon wafers.[1] Compared with their inorganic counterparts, organic solar cells technology are very attractive and promising due to following several reasons: flexible, light weight, low consumption of organic materials since films can be very thin, low cost, suitable for larger roll-to-roll manufacturing , tunable energy band gaps, and the organic PVs can be fabricated on fabrics and thus can be integrated into clothing and solar cell tents.[1]

In order to understand how nanomaterial such as ZnO nanorods can be integrated into and improve the device performance of organic solar cells, we will first study the optoelectronic processes of how the organic solar cells work.

Optoelectronic Processes in Organic Semiconductors

In organic conjugated polymeric materials, the electrons at the outer orbit are responsible for the optoelectronic process.[1] Analogous to the valence band and the conduction band in inorganic semiconductors, in organic semiconductor materials, the highest occupied molecular orbital (HOMO) refers to a highest energy level, and the lowest unoccupied molecular orbital (LUMO) refers to a lowest energy level.

Electrons from the HOMO are donated, mostly available for bonding and are most weakly held electrons; LUMO receives electrons and is the lowest energy orbital available.[1] Stable conduction bands and valence bands with bandwidth larger than 0.1eV, which are typical in inorganic semiconductors, are rare in organic semiconductors.[2] In organic semiconductors, free charge carriers transfer among different orbitals instead of transporting in bands as they do in inorganic semiconductors. Excitons are excited states of the molecule and bound electron-hole pairs, which can be treated as chargeless particles capable of diffusion.

Figure 1.2.1.1 and Figure 1.2.1.2 shows a schematic diagram of a Wannier exciton in inorganic semiconductors and a Frenkel exciton in organic semiconductors, respectively.[3] In inorganic semiconductors, Wannier excitons are loose electron-hole pairs with binding energy less than 0.03 eV and with size greater than 10nm.[1,4,5] In organic semiconductors, Frenkel excitons, with binding energy larger than 1eV, in order to be dissociated, they require extra energy such as the electric field formed at the donor acceptor interface.

Photovoltaic Processes in Organic Solar Cells

There are generally five different steps in the photovoltaic processes of the excitonic organic solar cells: first step is light absorption and exciton generation; secondly, the exciton diffuses to donor/acceptor interface; and thirdly, the exciton dissociates and thus charge separates at donor/acceptor interface; fourthly, charges are transported to the electrode; and finally, charges are collected in the electrode.[1]

Currently, none of the photovoltaic processes in organic solar cells have been optimized. Due to the loss of photons, excitons, and carriers, the power conversion efficiency is small (typically less than 7%).[1] However, there are lots of areas for improvement.

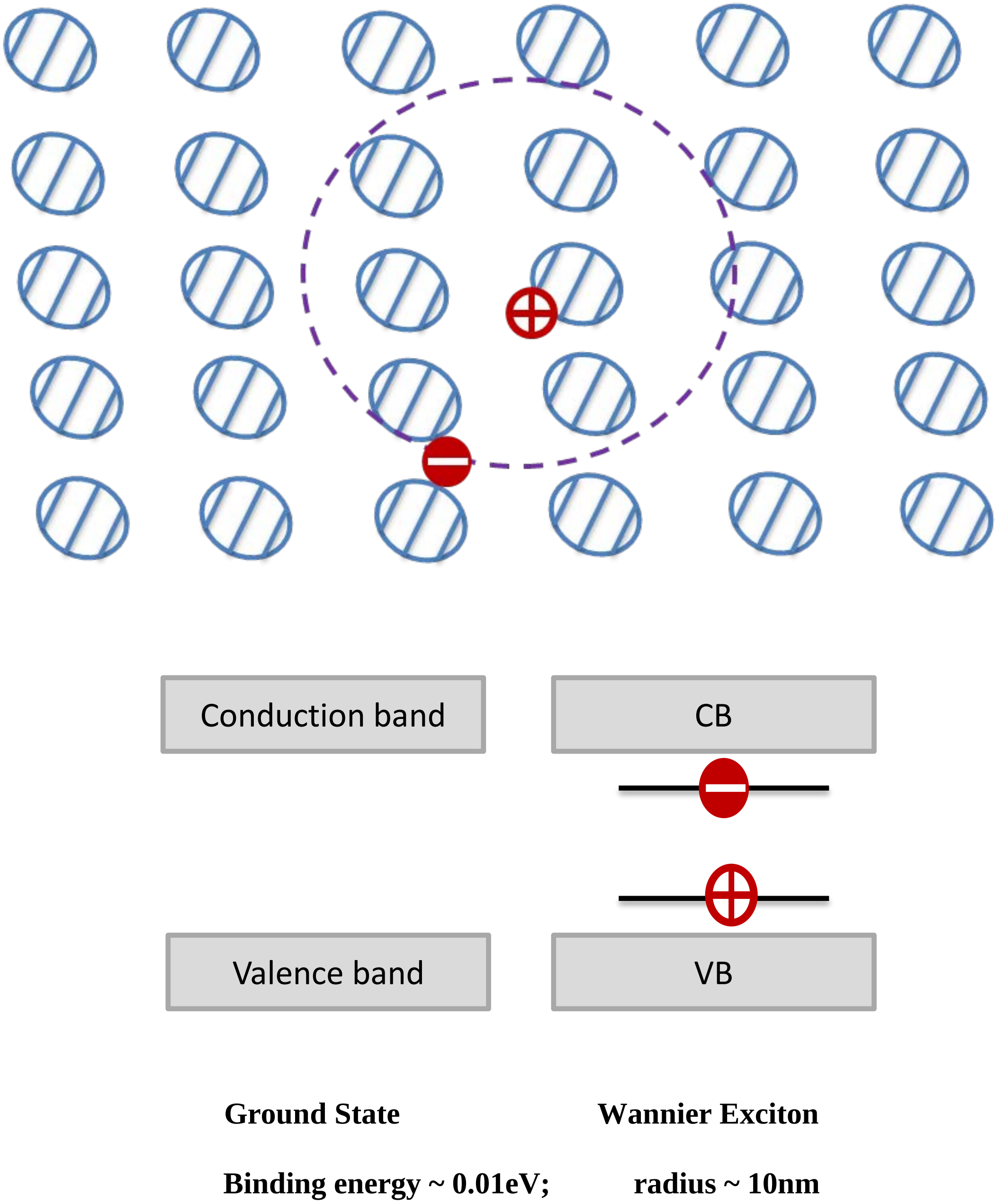

Figure 1.2.1.1. Inorganic Wannier excitons.[3]

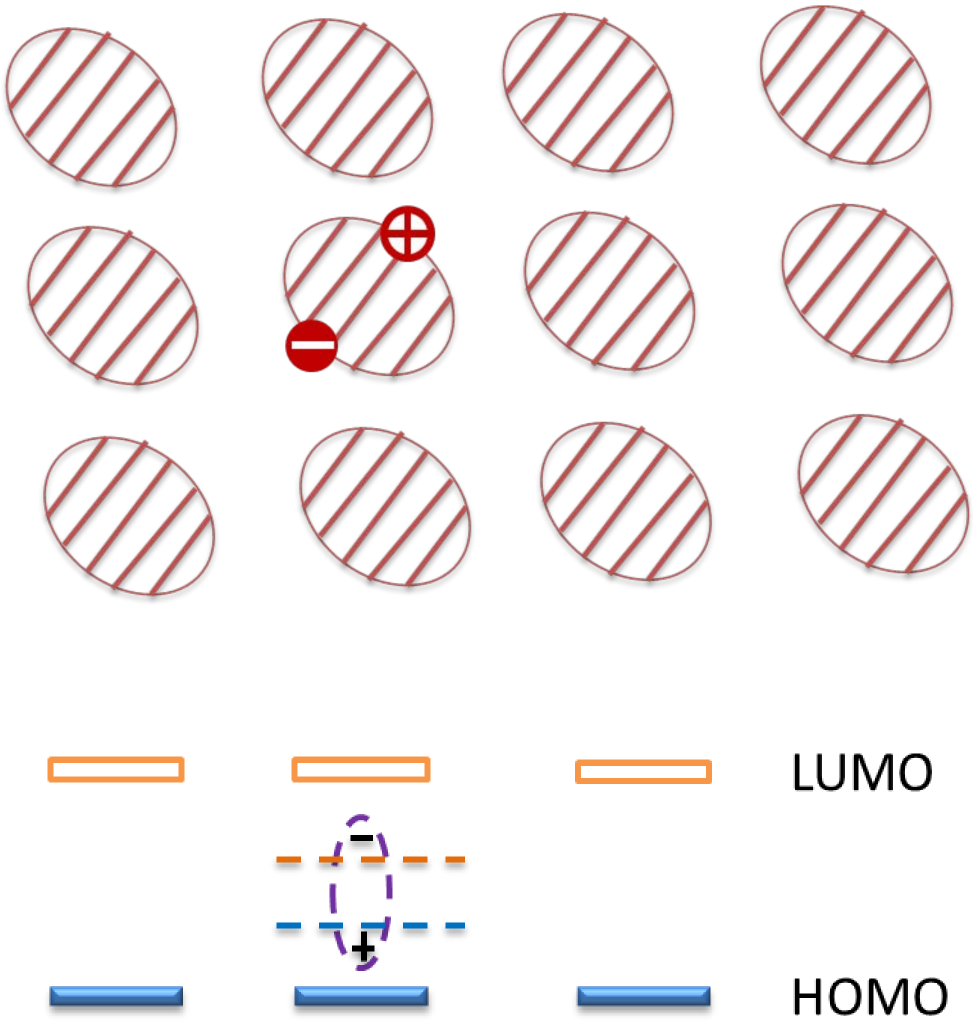

Frenkel Exciton

Binding energy ~ 1eV; radius ~ 1nm

Figure 1.2.1.2. Organic Frenkel excitons. [2,3]

Types of Organic Solar Cells

Single layer organic photovoltaic cell

Analogous to inorganic Schottky cells, the single layer organic solar cells is considered as the first generation organic solar cells. They are made by sandwiching a single layer of organic semiconducting materials between two different electrodes. Figure 1.2.1.3 (a) shows an example of such an organic solar cell. Single-layer organic photovoltaic cells have very small power conversion efficiencies since the carriers are mainly generated in the Schottky junction. [1]

Double layer organic photovoltaic cells

Analogous to the double layer *p* / *n* junction inorganic solar cells, the second generation organic solar cells are donor/acceptor (*p* / *n* junction) double layer cells (Figure 1.2.1.3 (b)). In 1986, C.W. Tang demonstrated the first double layer organic solar cells[6].

When generated exciton in either donor or acceptor layer diffuses to a donor/acceptor interface, charge separation take place where electrons transfer to the acceptor LUMO, and holes transfer to the donor HOMO.[1] Compared to single layered organic cells, the electrons and holes can transfer to their respective electrodes more easily and quickly due to the electric field formed at the organic donor/acceptor interface. Since electrons and holes move in two separate layers, charge recombination is less likely to occur than in single-layer cells.[1] However, double layer structure leads to thicker layer, which results in the loss of excitons; that is, excitons are wasted before they reach the donor/acceptor interface. To solve this thickness dilemma, in the next part, we will see the development of the next generation organic solar cells.

Bulk heterojunction (BHJ) photovoltaic cells

The third generation organic photovoltaic cell, which also is characterized as "bulk heterojunction (BHJ)" cells, is shown in figure 1.2.1.3 (c). By mixing or blending a donor semiconductor material and an acceptor semiconductor material, the dispersed donor/acceptor heterojunction layer in BHJ cells are realized.

The donor organic semiconductor material is usually a conjugated polymer (e.g. Poly (3-hexylthiophene-2,5-diyl) (P3HT)) and the acceptor semiconducting material is usually a fullerene (e.g. (6,6)-phenyl C61 butyric acid methyl ester (PCBM)).

In such BHJ cells, donor/acceptor interface are located randomly everywhere in the bulk photo active layer, excitons generated in either acceptor or donor material may get to the interface and break easily.[1]

Researchers worldwide have studied the organic bulk heterojunction solar cells which contains blend of conjugated polymer P3HT and fullerene PCBM, and achieved about 5% efficiencies.[7,8] Liu *et al.* [9] have reported the fabrication of flexible solar cells based on conjugated polymer and ZnO nanoparticulate thin films. Their flexible solar cells with a structure of PET/ITO/ZnO/regioregular poly(3-hexylthiophene-2,5-diyl) (P3HT):[6,6]-phenyl-C61-butyric acid methyl ester (PCBM)/Ag have shown a photovoltaic performance with open circuit voltage of 0.56 V, short-circuit current density of 12.55 mA cm^{-2}, fill factor of 0.36 and power conversion efficiency of 2.51%. They concluded that the exciton dissociation occurs at the interface between P3HT:PCBM instead of that between ZnO and P3HT.

The much improved device performance and power conversion efficiencies of BHJ cells over the previous generation double layer solar cells results from less exciton loss and thus the photoactive layer films can be made thicker than double layer cells which can lead to more photon absorption. However, there are still issues in charge transport to the electrodes and carrier loss in bulk heterojunction cells. In the next two sections, we will discuss how to improve the device performance: introducing nanomaterials such as ZnO nanorods into the organic BHJ heterostructure.

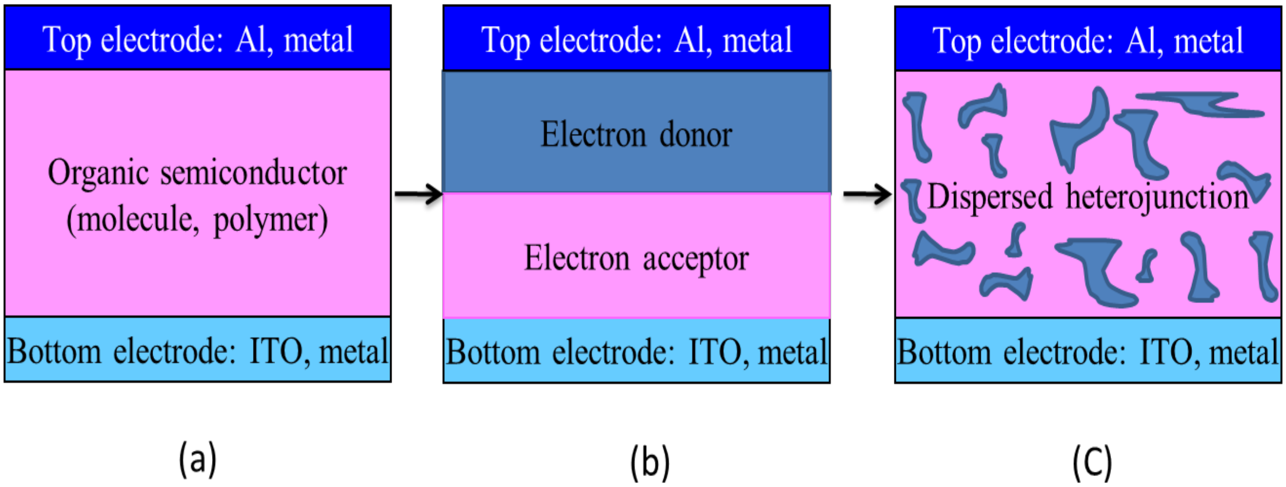

Figure 1.2.1.3 (a) Single layer, (b) Double layer donor/acceptor heterojunction and (c) Bulk heterojuction organic solar cells

1.2.2 Organic-Inorganic Hybrid Solar Cells

As described in the previous section, organic photovoltaic systems are affected by low carrier mobility, poor material morphology and stability, thickness dilemma, limited optical absorption and rapid degradation in operation. Inorganic nanomaterials, which have high carrier mobility, high surface to volume ratio and high absorption coefficient can alleviate some of these drawbacks of organic solar cells and can improve the organic photovoltaic systems to perform better commercially.[10]

Researchers worldwide are incorporating inorganic nanostructured semiconductor materials in the application of organic-inorganic hybrid solar cells. There are mainly four key areas of organic-inorganic hybrid photovoltaic systems: metal oxide-organic, carbon nanotube-organic, semiconductor nanowire-organic, and semiconductor nanocrystal organic systems.[10]

This dissertation mainly focuses on semiconductor nanocrystal organic systems, in particular, ZnO nanorods and conjugated polymer hybrid photovoltaic systems. Hybrid ZnO-conjugated polymer PV devices using ZnO nanorod arrays instead of planar films as the electron-transport layer have shown significant improvements in performance that have been attributed to increased heterojunction surface area. ZnO nanorod arrays are considered suitable to the application for hybrid photovoltaic devices.

Our work emphasizes on solution process on the synthesis of ZnO nanorods which remain the merits of organic solar cells which is solution processable. Since flexibility is the future trend of the electronics, we also fabricate the hybrid PV systems on flexible substrates – In_2O_3-PET to keep the important advantages of organic solar cells – flexibility and light weight. The details of the fabrication steps of the organic-inorganic solar cells will be discussed in Chapter 3.

1.2.3 ZnO and ZnO nanorods

As direct gap semiconductors, which have a strong interaction with light due to the law of momentum conservation, ZnO and GaN are widely used in photonic devices applications. Table 1.2.3 summarizes the crystal properties of GaN and ZnO.

Material	Crystal structure	Bandgap (eV)	Static dielectric constant	Lattice constant (*Å)*	Density (gm/cm^3)
GaN	Wurtzite	3.44	$\varepsilon_\parallel$=10.4, $\varepsilon_\perp$=9.5	a=3.175, b=5.158	6.095
ZnO	Wurtzite	3.37	$\varepsilon_\parallel$=8.75, $\varepsilon_\perp$=7.8	a=3.253, b=5.213	5.675

Table 1.2.3 Crystal properties of GaN and ZnO.[11]

GaN and ZnO have the same crystal structure – Wurtzite structure (Figure 1.2.3). As a II-VI semiconductor, ZnO is a promising candidate for short-wavelength optoelectric applications such as ultraviolet (UV) laser, light-emitting diodes (LEDs) and laser diodes. The Synthesis Routes of ZnO includes vapor phase synthesis, metal-organic chemical vapor deposition (MOCVD), and solution-based synthesis. In our experiment, we employed the solution growth method which offers the advantage of low temperature and simplicity, the details of this method will be discussed in Chapter 2. ZnO are naturally n type semiconductor, there are difficulties in p-type doping. Right now, the primary issue to achieve LEDs based on ZnO is the ability to achieve reliable p-type material.

As one of the one dimensional (1-D) nanostructures of ZnO, ZnO nanorods have very important features: each unit is made of a single crystal and very large surface to volume ratio.

These features make it quite suitable in integrating into photonic devices such as organic semiconductors which will be discussed in the next section. Vast and intensive research worldwide has been focused on fabricating 1-D nanostructures such as ZnO nanorods. Due to the simple formation and device application, ZnO nanorods have been widely studied.

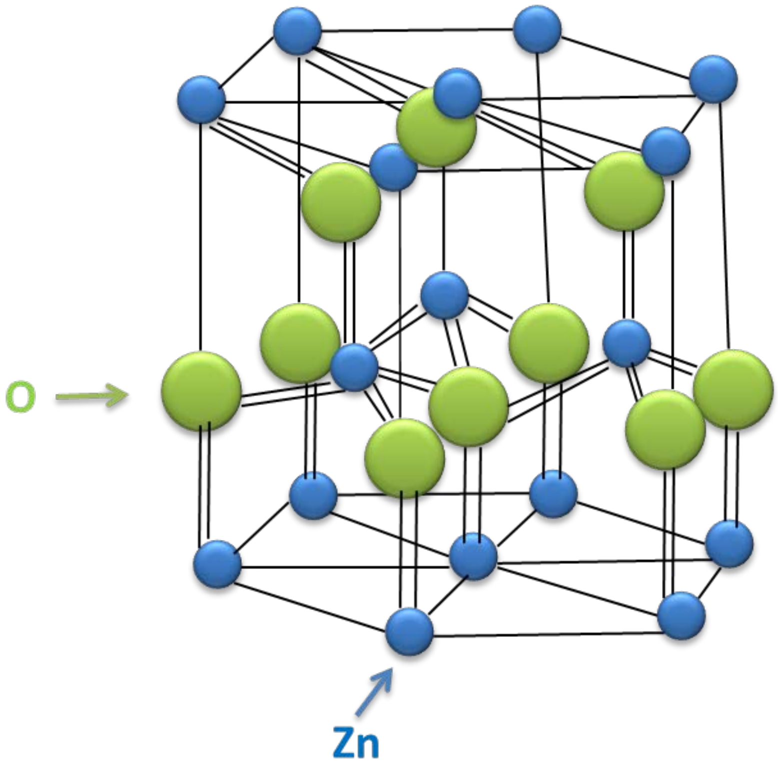

Figure 1.2.3. Wurtzite structure of ZnO

1.2.4 Synthesis of ZnO Nanorods

Due to the high surface-to-volume ratio provided by the one-dimensional (1D) nanostructure, ZnO nanorod arrays are considered suitable for the application for hybrid photovoltaic devices.[12,13,14,15] Current research on conjugated polymer infiltrated ZnO nanorod array hybrid solar cells reports power conversion efficiencies ranging from 0.2% [16] to 2.7% [12]; these have only been fabricated on rigid glass substrates rather than on flexible plastic substrates.

The driving force for research activities in the synthesis of nanostructured functional materials is the ability to control a material's properties by controlling the size and shape of the crystals and their arrangement into 1, 2 and 3 dimensional structures extending over several length scales. These developments can lead to new applications in diverse fields including energy conversion and storage. The future of these technologies is strictly dependent on the availability of optimized synthesis routes that allow the processing and manipulation of functional metal oxides in a precise manner.

Zinc oxide is a semiconductor with a wide direct band gap of 3.37 eV and a large exciton binding energy of 60 meV, which makes the material useful for optoelectronic applications.[17,18] Nanostructures of ZnO such as ZnO nanowires and nanorods have received increased attention due to their excellent electrical and optical properties.[19]

One-dimensional (1D) ZnO nanorods have received increased attention due to their high surface-to-volume ratio and their excellent electrical and optical properties.[20] ZnO nanorod array have become increasingly important, as they have been found to contribute greatly towards improving electron transport speed in organic-inorganic hybrid solar cells.[12,20,21]

In the past few years, ZnO nanorods have been synthesized via various physical and chemical methods including, metal-organic chemical vapor deposition (MOCVD),[22,23,24] vapor phase synthesis, [25,26,27] and solution-based synthesis [28,29,30,31]. Among these methods, solution-based method has the advantages of low costs, simplicity, low growth temperature, and easy coating of large surfaces. Intensive research has been focused on the solution growth process of ZnO nanorods on ITO coated glass substrates. Guo *et al.* [32] have systematically studied the effect of processing conditions such as pre-treatment of the substrates, growth temperature, deposition time and the concentration of the precursors on the morphology and alignment ordering of ZnO nanorod arrays during solution process. Our group[33] has systematically studied the effect of precursor solution concentration on quality of ZnO nanorods grown on ITO/PET substrates by low-temperature solution method.

1.3 AlGaN/GaN High Electron Mobility Transistors

1.3.1 AlGaN/GaN Heterostructures

Polar Materials: GaN and AlN

Spontaneous polarization:

As group III-Nitrides, GaN, AlN and InN have wurzite crystal strucutures and they are polar materials since there's net polarization due to a shift in the cation and anion sublattices.[11] This arrangement generates a "spontaneous polarization" effect in the crystal. In heterostrucures, spontaneous polarization effect is of great importance. For example, there's no net polarization in unstrained zinc blend structures because of the arrangement of cation and anion.[11] Figure 1.3.1.1 shows the crystal structure and spontaneous polarization in GaN.

The spontaneous polarization values of GaN, AlN, and InN are summarized in Table 1.3.1 summarizes. From this table we can see that the spontaneous polarization of AlN, GaN and InN are all negative and it is higher in AlN than in GaN.[34]

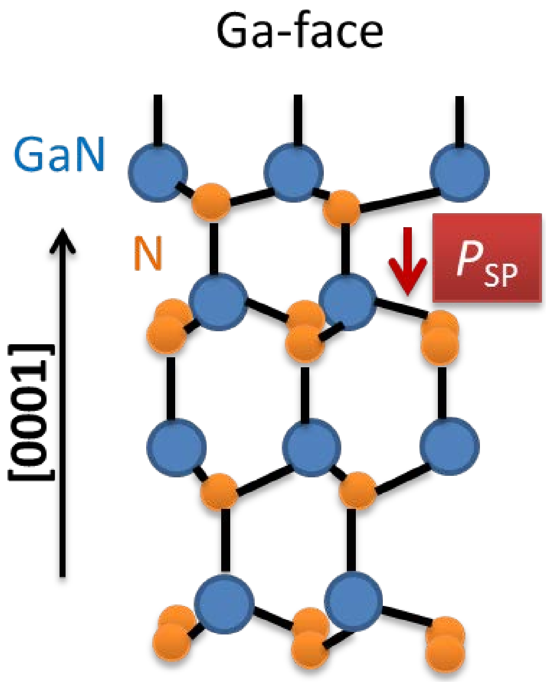

Figure 1.3.1.1 Crystal structure and spontaneous polarization in GaN

	Spontaneous Polarization (Cm^{-2})
GaN	-0.029
AlN	-0.081
InN	-0.032

Table 1.3.1 Spontaneous polarization values of GaN, AlN, and InN.[35]

Piezoelectric polarization:

Besides spontaneous polarization, GaN and AlN also exhibit piezoelectric polarization effect in the material. Nitrides lack inversion symmetry and exhibit piezoelectric polarization when strained along the [0001] direction.[36] The piezoelectric coefficient of nitrides is almost an order of magnitude higher than the other III-V materials.[37] The interface polar charge can cause a built-in electric field and can act as dopant which can be of great importance in designing devices. Figure 1.3.1.2 shows the spontaneous polarization, P_{SP}, and piezoelectric polarization, P_{PE}, in AlGaN/GaN.

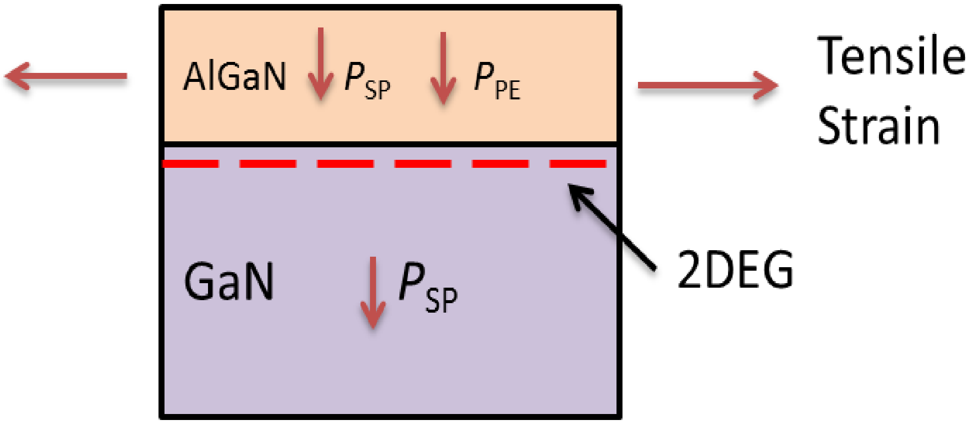

Figure 1.3.1.2 Spontaneous polarization P_{SP} and piezoelectric polarization P_{PE} in AlGaN/GaN Heterostructure.

In summary, AlGaN/GaN heterostructures have interface polarization charges due to both spontaneous polarization and piezoelectric effect. To screen the net positive charge formed at the

AlGaN/GaN heterointerface, a 2 dimensional electron gas (2DEG) is formed. The density of the 2DEG can be as high as 10^{13} cm^{-2}.[11] Figure 1.3.1.3 shows the band diagram and polarization charge of AlGaN/GaN HEMT.

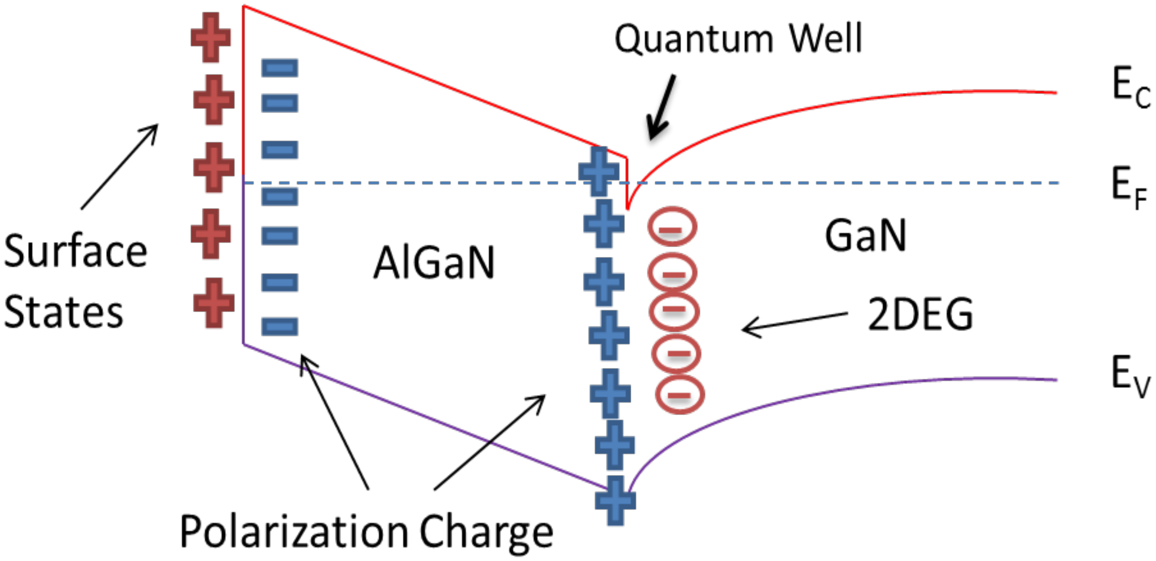

Figure 1.3.1.3 Band diagram and polarization charge of AlGaN/GaN HEMT.

1.3.2 AlGaN/GaN HEMT Basics and Applications

Nitride based semiconductor devices have attracted most attention in the application of high power electronics, solid state lighting, and high power amplifiers. The wide band gap (3.44 eV) of GaN, makes it suitable for high voltage, high-power and high-temperature microwave applications because of its high electric breakdown field and intrinsic carrier concentration. Besides the wide energy band gap, high critical electric field (4 MV/cm) and high electron saturation velocity make GaN and its alloys one of the most promising materials for power electronic device application.[38,39]

The basic concept of High Electron Mobility Transistor (HEMT) is that two semiconducting materials with different band gaps brought together in close contact to form a heterojunction.[40] In the case of AlGaN/GaN HEMT, AlGaN can be formed by alloying GaN with AlN, which makes the construction of AlGaN/GaN heterostructure readily realizable. Two dimensional electron gas (2DEG) density as high as 10^{13} cm^{-2} can, which is the heart of HEMT, formed at the AlGaN/GaN junction (at GaN side but close to interface of AlGaN).

AlGaN/GaN HEMTs are similar to normally-on MOSFETs but eliminate the need of substrate doping. And compared to AlGaAs/GaAs HEMTs, which requires intentional doping to form charge sheet at the junction, 2DEG in AlGaN/GaN HEMT doesn’t need doping since spontaneous and piezoelectric polarization generated 2DEG. Thus among the various HEMT materials and device technologies, the AlGaN/GaN HEMT seems the most promising for the applications of high power electronics, RF power transistors, and high power amplifiers. Figure 1.3.2 shows the basic AlGaN/GaN HEMT structure.

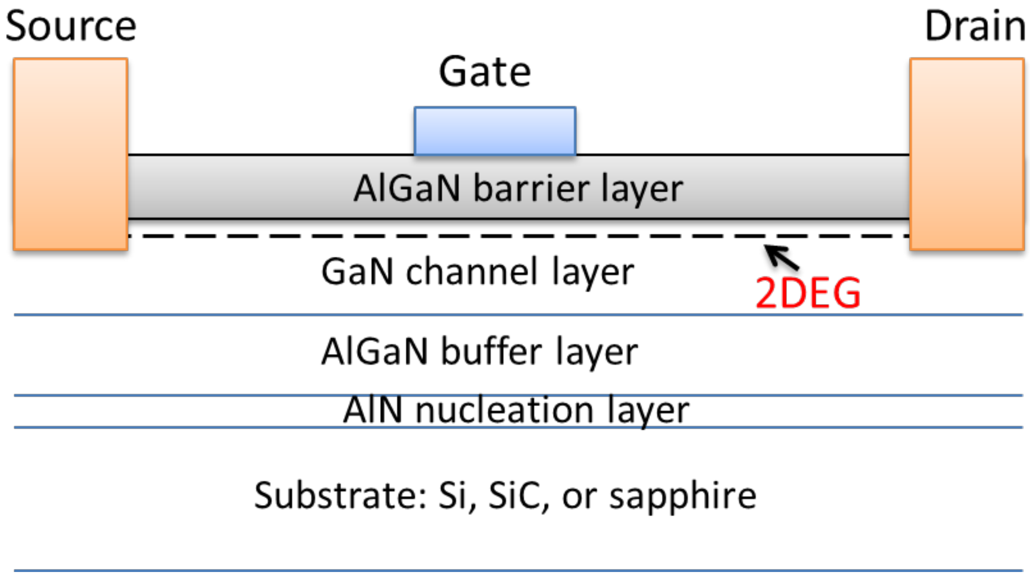

Figure 1.3.2 Basic AlGaN/GaN HEMT structure

1.3.3 GaN-on-Si Wafers

As a typical form of high power electronic device, High electron mobility transistor (HEMT) is a typical form of is built based on AlGaN/GaN heterostructures. Among the various substrates of bulk GaN, sapphire, Si, and SiC which are available for the growth of AlGaN/GaN HEMT, GaN and SiC substrates are expensive and have small diameters (usually below 4 inch), sapphire substrates with large diameter wafers are very expensive and also have low thermal conductivity, the Si substrate has attracted great attention due to the drastic reduction in manufacturing cost, high crystal quality and availability of large diameter wafers.[41] Moreover, uue to the large mismatch in lattice parameters and thermal expansion coefficients between GaN and Si, it is of necessity to deposit carefully designed and graded (with different Al composition) AlGaN buffer layers between GaN and Si.

Typical device structures are shown in Figure 1.3.3. The wafer is AlGaN/GaN HEMT epi structures on 6” p-type Si (111) wafer.

Chumbes *et al.*[42] have fabricated AlGaN/GaN High electron mobility transistors on Si(111) substrates and with a gate length of 0.3 µm, their device ehibit a source to drain current as high as 0.66 A/mm when biased at 1V. Lu *et al.*[43] have studied the breakdown mechanism in AlGaN/GaN HEMTs on Si Substrate. Bouzid *et al.*[44] have applied the AlGaN/GaN HEMTs on Si Substrate for the microwave power applications above 30 GHz.

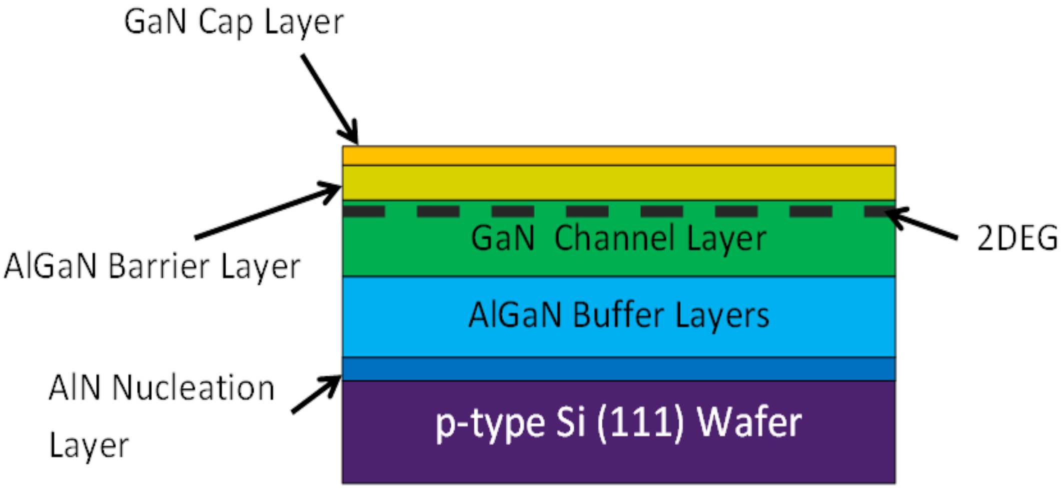

Figure 1.3.3 Schematics of the AlGaN/GaN HEMT wafer

1.2.4 Round HEMT Technology

In recent years, RoundHEMT technology was proposed for simple and fast fabrication and investigation of modulation doped AlGaN/GaN HEMTs.[45] Compared to the traditional rectangular HEMT structure, the microelectronic fabrication procedure of the RoundHEMT is greatly simplified since it doesn't require the mesa etching for the source and drain region.

Marso *et al.*[46] has reported the optimization of the device performance of AlGaN/GaN HEMT by using the RoundHEMT technology. With gate length of 0.2 µm and source-to-drain distance of 4 µm, their best device yields a source to drain current I_{DS} of 0.7 A/mm.

With RoundHEMT technology, only two photolithographic and metallization steps are needed for the microelectronic fabrication steps. In the layout of RoundHEMT, as shown in Figure 1.2.4, the drain contact of the round HEMT is placed inside the gate ring. The source metallization encloses the gate, eliminating the need of mesa etching (Figure 1.3.4). This design confines the current flow from source to drain under the gate, just like the role of mesa. Comparison to the conventional open fingers HEMT fabrication, where mesa etching and contact pads are required, the RoundHEMT technology is a significant improvement in simplifying the fabrication steps.

In our work, round AlGaN/GaN HEMT were fabricated using standard ohmic contact technology (Ti/Al/T/Au metallization with annealing at 850 °C for 30 sec) for the device characterization and performance. Right now, our smallest scale device has gate length of 40 µm and and source-to-drain distance of 10 µm, and the yield I_{DS} is about 0.02 A/mm with zero gate bias. We plan to scale down the device dimension and thus the I_{DS} and transconductance will be increased.

In Chapter 4, detailed micro fabrication steps and device characterization of the round HEMT were discussed. The RoundHEMT concept is a powerful technique for the fast evaluation of the correlation between layer parameters and transistor properties.

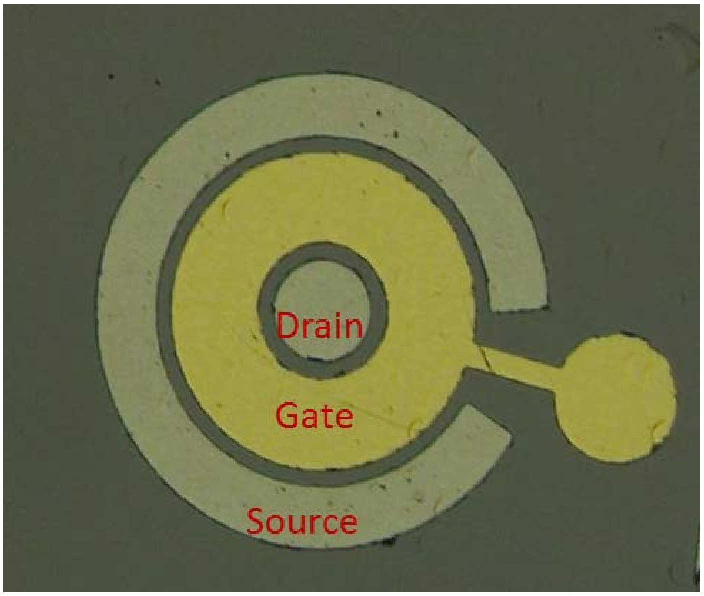

Figure 1.3.4 Optical micrograph of Round HEMT (photo credit: Chungman Yang)

1.4 Major Findings and Novelty Statement

My major findings/novelty statement in organic-inorganic hybrid solar cells research is as follows:

- Low-temperature aqueous solution growth of uniformly aligned ZnO nanorod arrays on the flexible substrates and systematic investigation of the effect of precursor solution concentration on the quality of ZnO nanorods grown on flexible In_2O_3-PET substrates. Results are published in ISRN Nanomaterials **2012**, 651468, (2012).
- Innovative fabrication and characterization of ZnO nanorods and conjugated polymer hybrid flexible solar cells. And power conversion efficiency of 1.8% was achieved of the PV device. Results are published in Semiconductor Science and Technology **27**, 105005 (2012).

And my major findings/novelty statement in AlGaN/GaN HEMTs research is as follows:

- We have proposed a simple diagnostic technique to evaluate the “electrical” homogeneity of the large area AlGaN/GaN HEMT/Si wafer. This method can be considered as a simplified version of photoionization spectroscopy.
- Fabrication and characterization of the round AlGaN/GaN HEMT devices from various areas of the 6” GaN-on-Si HEMT epitaxy wafer was conducted and the characterization results were analyzed.
- Operating the fabricated round AlGaN/GaN HEMT devices at high temperatures. The results show that the devices can operate up to 300 °C with minimal degradation.

CHAPTER 2

Fabrication and Characterization of ZnO Nanorods

2.1 Introduction

Before we fabricate ZnO nanorods integrated organic Bulk heterojunction solar cells, we need to first introduce the ZnO nanorods in. In the fabrication process of the organic-inorganic photovoltaic devices, ZnO nanorod arrays need to be first introduced inside the device structure. If it is ZnO nanoparticles, it can be added at the same time as the organic active layer or dispersed into organic polymeric layer. However in the case of nanorod arrays, they have to be first grown on the substrate or back electrode.

And as mentioned in Chapter 1, to remain the merits of the advantage of all solution process of organic solar cells (especially flexible organic PVs), we employ the low temperature solution growth method to synthesis the ZnO nanorod arrays.

Moreover, since the size and shape of nanorods are important in the final device performance, we did systematical study of the morphology, crystal quality and optical quality of the ZnO nanorods that is grown in different time and precursor concentration.

In this chapter, the detailed synthesis process via solution growth method will be discussed. Figure 2.1 shows the flow chart of the overall synthesis process of ZnO nanorods on ITO-glass and In_2O_3-PET substrates.

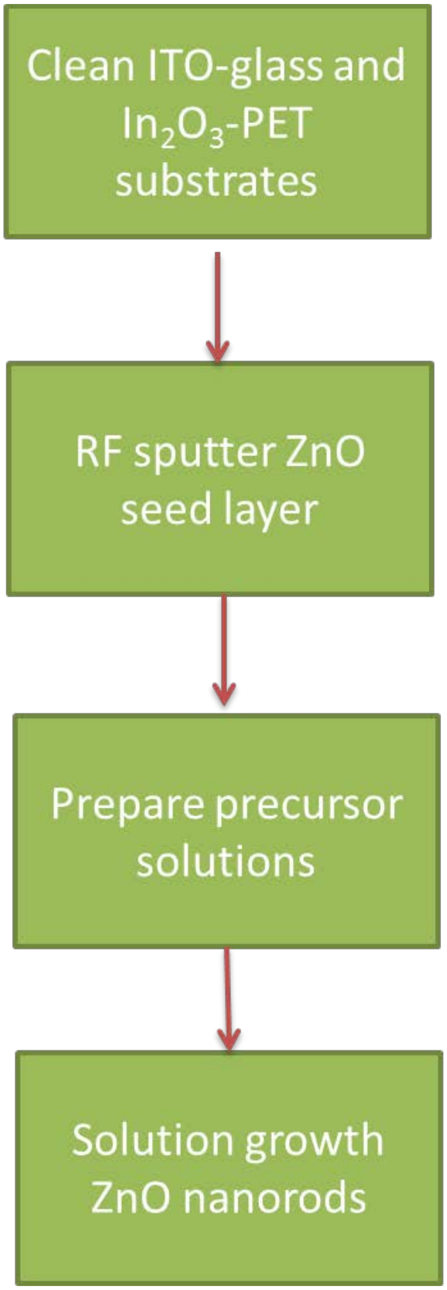

Figure 2.1 Flow chart of the synthesis process of ZnO nanorods on ITO-glass and In_2O_3-PET substrates.

2.2 ITO-glass and In_2O_3-PET Substrates

The substrates used in this study for growing ZnO nanorods and fabricating photovoltaics were transparent conducting oxide (TCO) coated substrates (indium tin oxide (ITO) coated glass and indium oxide (In_2O_3) coated polyethylene terephthalate (PET) flexible film).Due to the low electrical resistivity and transparency in the visible and high infrared reflectivity[47], ITO-glass and In_2O_3-PET are widely used substrates in organic electronics[48], such as in the fabrication of organic electronics such as organic solar cells and organic/polymer LEDs. In this study, special attention was given to the flexible, conducting In_2O_3 coated PET substrate, which has advantages of light weight, flexibility, and low cost.

ITO-coated glass substrates with sheet resistance of 15 Ω square^{-1} were purchased from Kintec Inc.. The configuration of the purchased 1 inch × 1 inch ITO-glass substrate was Glass / SiO2 buffer (~23 nm) / ITO, in which the ITO film is RF magnetron sputtered. The In_2O_3-PET substrates, with a sheet resistance of 4-10 Ω square^{-1}, were purchased from Delta Technologies, LTD. These substrates have a multi-layer of sputtered In_2O_3/Au/Ag on an optical grade 0.2 mm thick PET film, and exhibit transmittance/resistance characteristics similar to those of the ITO coated glass substrates. The flexible substrates were cut into 1 inch × 1 inch pieces. Prior to RF magnetron sputter deposition, both the ITO-glass and In_2O_3-PET substrates were cleaned in an ultrasonic agitation bath (as shown in Figure 2.2.1) in a sequence of detergent solution, acetone, isopropanol alcohol, and deionized water for 5 min each, followed by nitrogen blow drying. Finally, a ¼ inch Kapton tape, which is made from Kapton polyimide film with silicone adhesive and compatible with a wide temperature range of 269°C (452°F), was used to cover an area of the as-cleaned substrates to define the ITO electrode area (Figure 2.2.2).

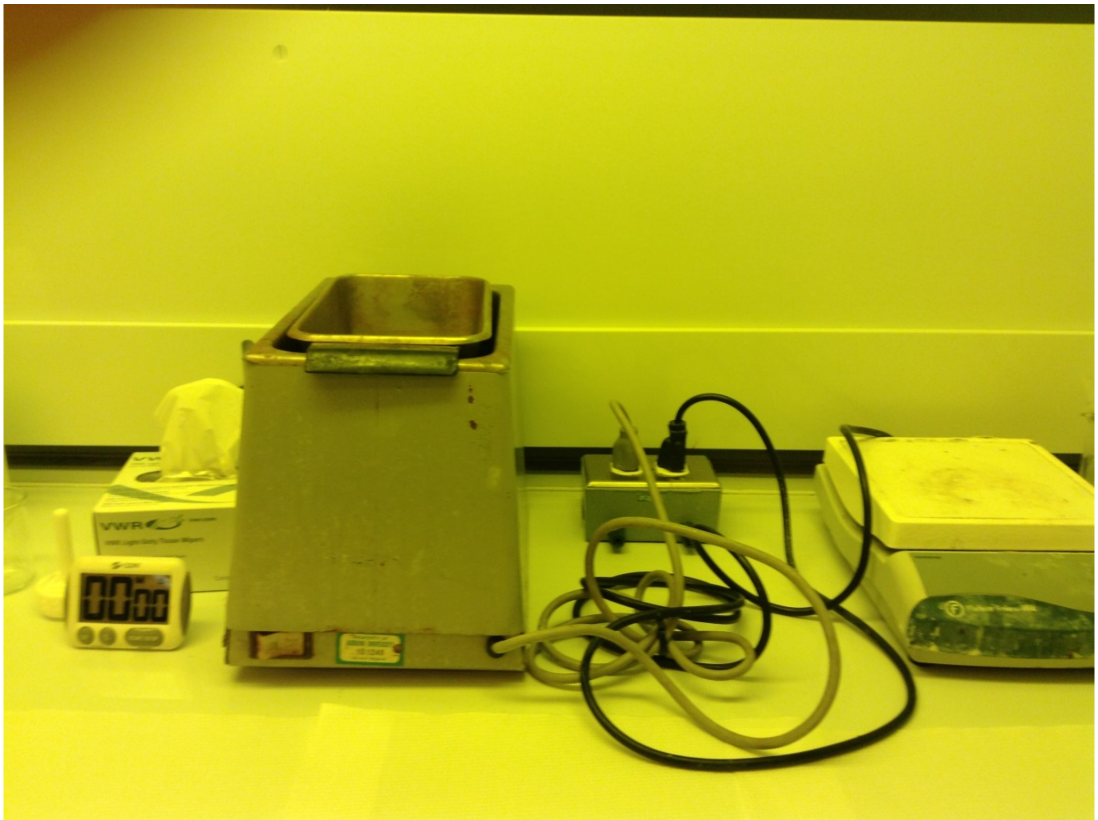

Figure 2.2.1 Ultrasonic agitation bath

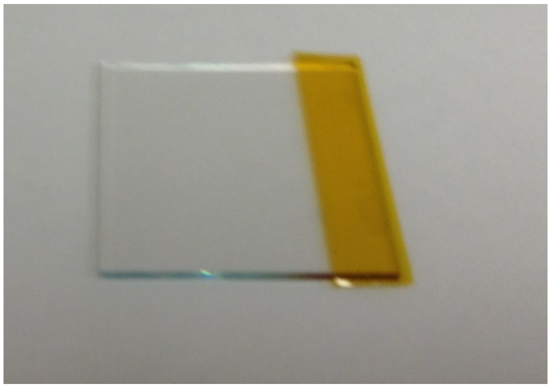

Figure 2.2.2 Cleaned ITO/glass covered by kapton tape

2.3 RF Sputter ZnO Seed Layer

The zinc oxide nanorods were prepared by a two-step process which was similar to the procedure reported in the literature. [49, 50] In the first step, ZnO seed layer with an approximate thickness of 40 nm were radio-frequency (RF) sputtered on the as-cleaned ITO-glass and In_2O_3-PET substrates. In the second step, ZnO nanorods were synthesized via low temperature solution growth method, which is discussed in section 2.4. Figure 2.3 shows the RF magnetron sputter system used in this experiment.

The Zinc Oxide target (99.999% pure) with 3 inch diameter and 0.125 inch thickness was purchased from Kurt J. Lesker Inc.. Firstly, a ~40nm thick ZnO seed layer was sputtered on the ITO-glass or In_2O_3-PET substrates. The additional role of this ZnO seed layer is that it serves as a hole blocking barrier in the later fabrication of the photovoltaics which is discussed in Chapter 3. The sputtering was performed for 25 min under the Ar (ultra high purity) and O_2 flow rates of 20 sccm and 2 sccm, respectively.

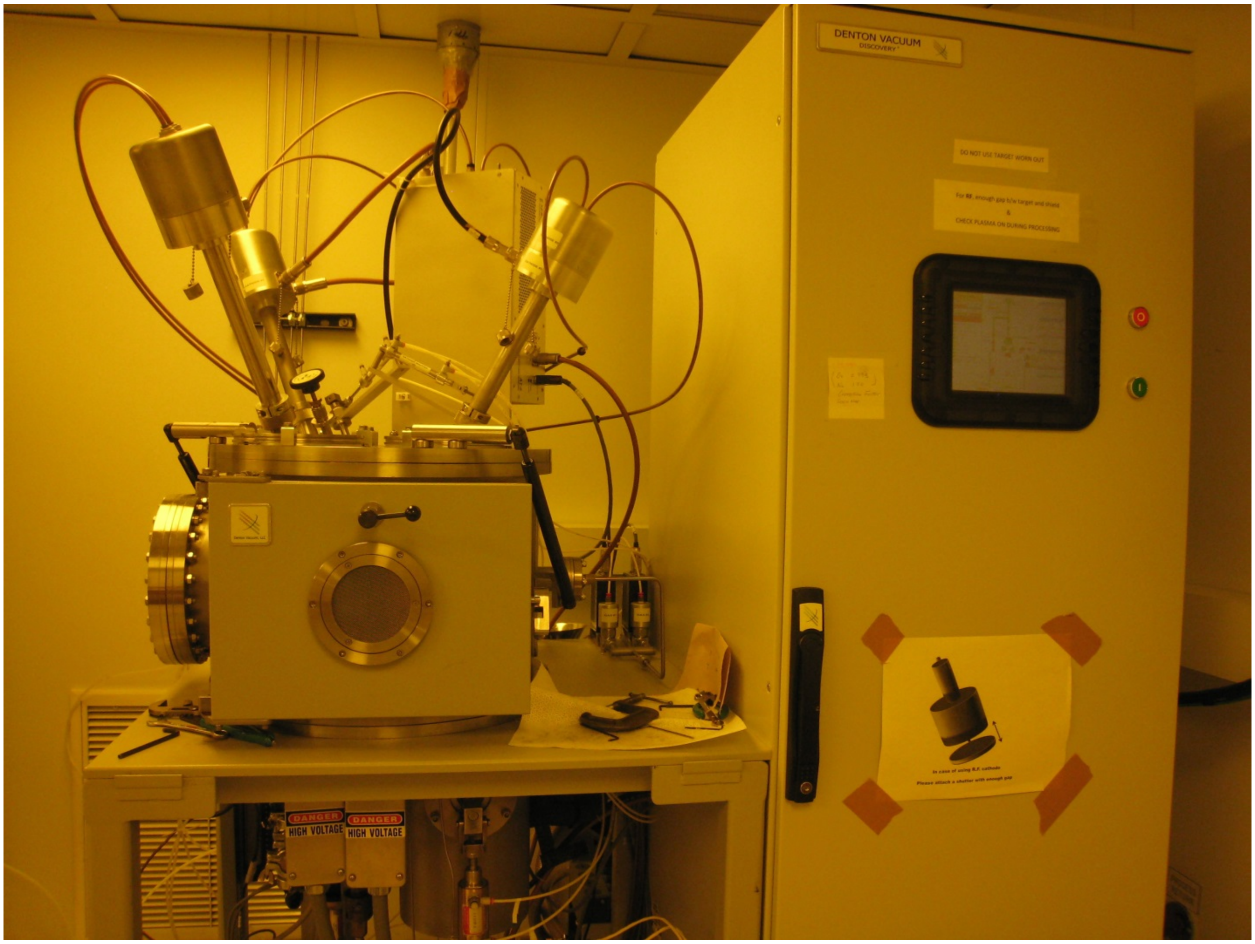

Figure 2.3 RF magnetron sputter system.

2.4 Synthesis of ZnO Nanorods via Low Temperature Solution Growth Method

As mentioned in the previous section, in the second step, an aqueous solution which contained zinc nitrate hexahydrate ($Zn(NO_3)_2{\cdot}6H_2O$, Crystalline/Certified, Fisher Chemical, f.w.=297.49), and the same mole of hexamethylenetetramine (HMT, Sigma-Aldrich, M.W.=140.19) in 400 mL distilled water mixture was prepared in a beaker. As shown in Figure 2.4.1, initially, an Apex series balance (APX-60, Denver instrument) was used to measure the desired amount of $Zn(NO_3)_2{\cdot}6H_2O$ and HMT. And then the beaker was sealed by plastic wrap and was stirred using a stirrer (as shown in Figure 2.4.2) for 10 min at room temperature.

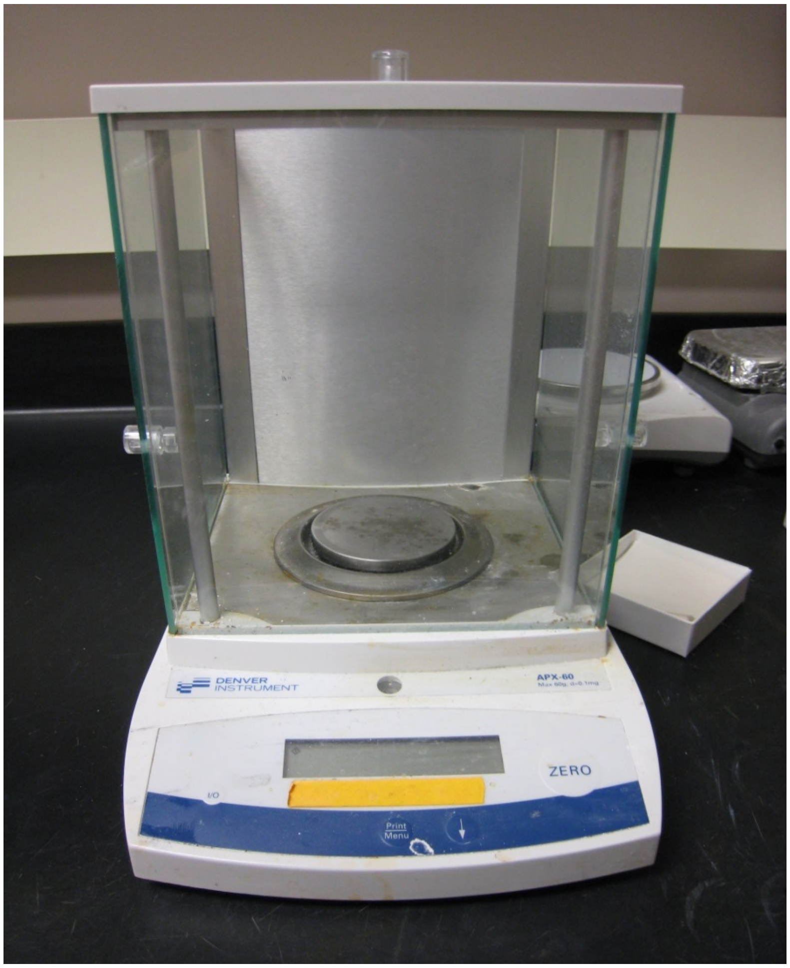

Figure 2.4.1 Apex series balance (APX-60, Denver instrument)

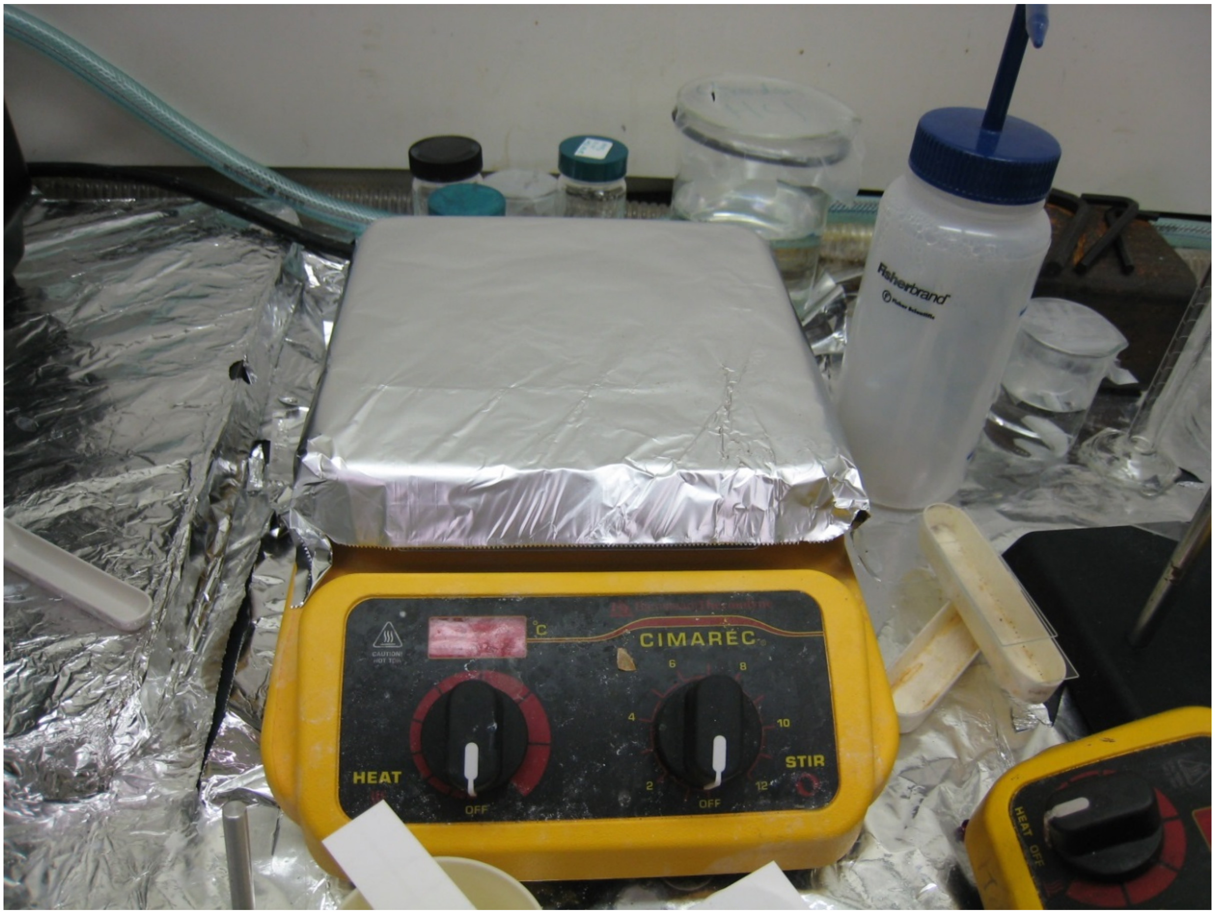

Figure 2.4.2 Stirrer hot plate.

Subsequently, the as-sputtered ITO-glass and In_2O_3-PET substrates with the dense ZnO seed layers were suspended horizontally upside-down in a beaker which contains the aqueous solution of equimolar of Zinc Nitrate Hexahydrate and HMT. The ITO or In_2O_3 side of the sample was facing down and the distance between the sample and the bottom of the beaker is about 1cm. Figure 2.4.3 shows the schematic presentation of the solutions with the samples. Then the solution with the substrates (still sealed by plastic wrap) was transferred to an isothermal hot water bath (IsoTemp 202 Water Bath, Fisher Scientific) (as shown in Figure 2.4.4). The solution synthesis process of ZnO nanorods was conducted at 85 °C for 2 hours. The temperature of the water was elevated to 85°C before dipping the aqueous solution into the hot water bath. After 2 hours of solution growth, the substrates were rinsed with distilled water for several times and then dried in air at room temperature.

The effect of time duration and solution concentration on the growth of the ZnO nanorods was systematically studied by scanning electron microscopy, X-ray diffraction, micro-Raman spectroscopy, and photoluminescence spectroscopy, which are discussed in the following sections in this chapter. For example, to grow about 300nm ZnO nanorods on ITO coated glass substrates, the solution process condition is 0.01M, 80min at 85°C (Figure 2.4.5). And at the same condition, it will take about 100 min on In_2O_3-PET substrate (Figure 2.4.6). The ZnO nanorods with an average diameter of 40~50 nm and average length of 300~400 nm plays an important role in rapid collection and transportation of the photo-generated electrons.

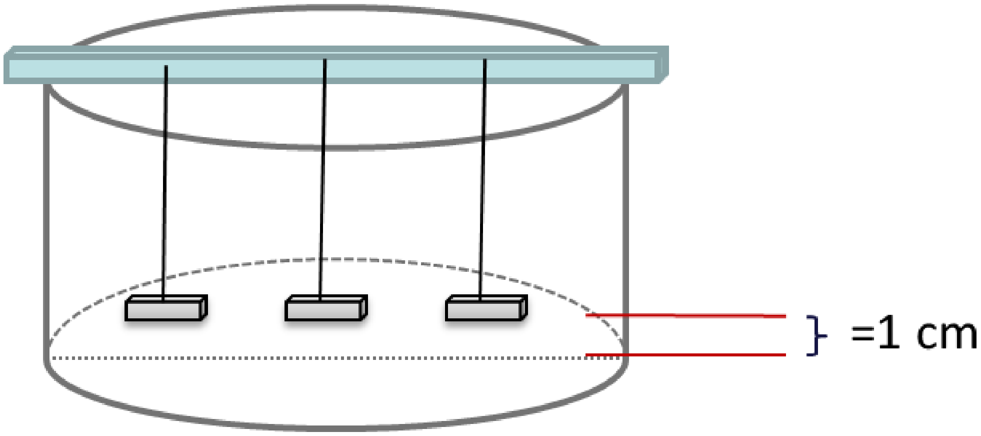

Figure 2.4.3 Schematic presentation of the solutions with the samples.

Figure 2.4.4 Isothermal hot water bath (IsoTemp 202 Water Bath, Fisher Scientific).

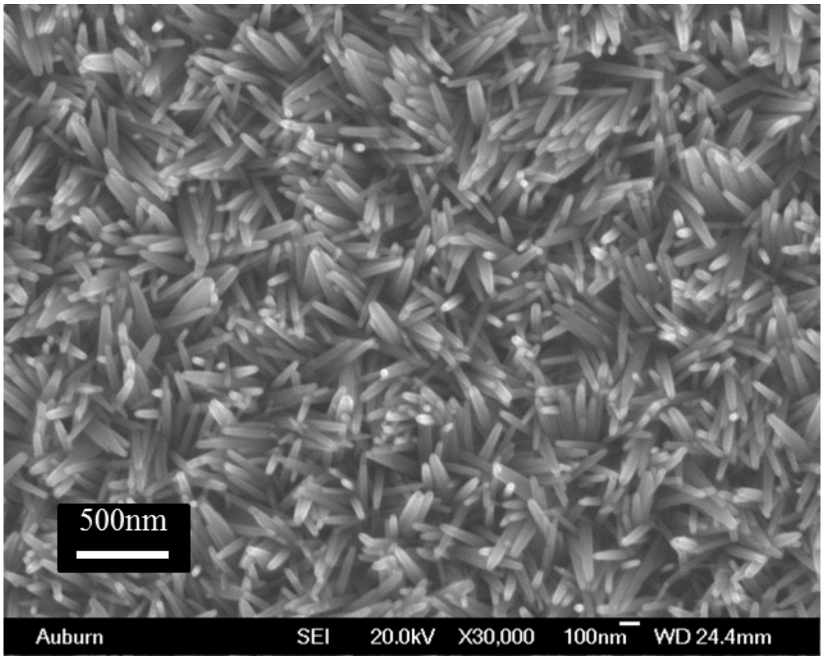

Figure 2.4.5 SEM graph of ZnO nanorods sythesized on ITO-glass.

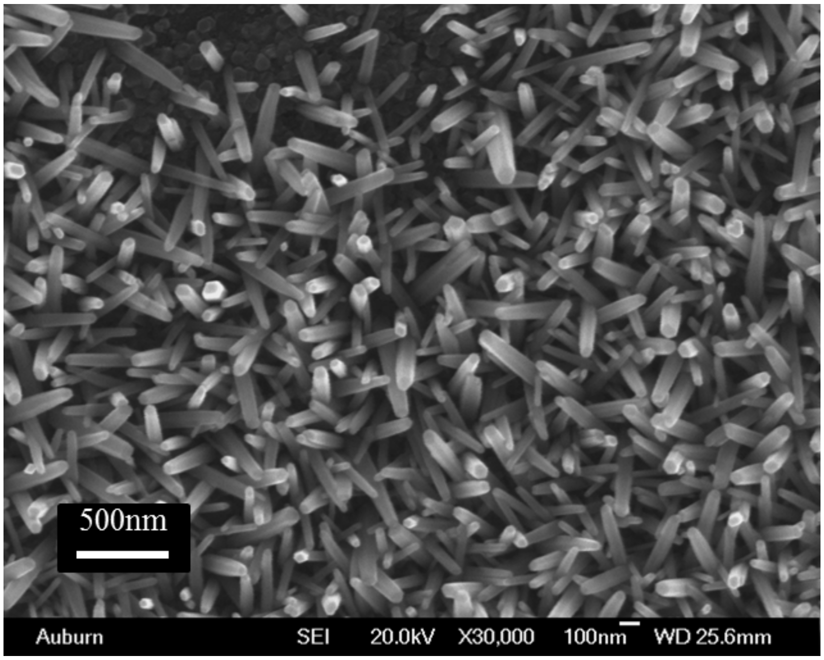

Figure 2.4.6 SEM graph of ZnO nanorods sythesized on In_2O_3-PET.

2.5 Scanning Electron Microscopy

As the saying goes, a picture is worth a thousand words. Scanning electron microscopy (SEM) is a very important and useful tool in study the morphology of the crystals. Field emission-scanning microscope (FE-SEM, JEOL JSM-7000F) was used to observe the morphology of the ZnO nanorods synthesized on both ITO coated rigid and flexible substrates. Since flexibility is the future trend of the electronics, we focus on the study of the effect of precursor concentration dependence on the growth of ZnO nanorods on flexible substrates. And for the concentration effect study, five different concentrations (50mM, 37.5mM, 25mM, 18.75mM, and 12.5mM) solutions of the Zinc Nitrate Hexahydrate and HMT in distilled water were prepared. And the growth time was fixed at 2 hr.

Figure 2.5.1 and Figure 2.5.2 shows the top view, high magnification (×10,000) and higher magnification (×30,000) magnification, respectively, of the SEM images of ZnO nanorods grown under the five different solution concentrations on In_2O_3-PET substrates.

As can be seen in these images, highly uniform and densely packed arrays of ZnO nanorods were successfully synthesized under various solution concentrations. The nanorods covered the entire surface uniformly with the hexagonal shape. For higher concentrations, for example, for 50 mM, the nanorods grow very straight since the density is so high; whereas for the lower concentrations, the ZnO nanorods are titled, and thus we can also measure the height of the nanorods from these top view SEM images. However, for the highest concentration 50 mM, we need to look at the cross section SEM image to have a better idea of the height. Figure 2.5.3 shows the cross-sectional view of the 50 mM sample.

In summary, arrays of ZnO nanorods with hexagonal shapes were successfully formed under various solution concentrations. Based on the SEM images, average values of the length, diameter, and aspect ratio of the nanorods are summarized in Table 2.5.1 and are plotted in Figure 2.5.4 as a function of solution concentration. It was found that the diameter and length of the ZnO nanorod increases as the precursor solution concentration increases. The average diameter and length of the nanorod increased almost lineally from about 174 nm to 397 nm and from 600 nm to 1200 nm, respectively, upon increase of the solution concentration from 12.5 mM to 50 mM. It was found that the diameter, length, and density of the ZnO nanorods could be well controlled by changing the solution concentration during growth. It also appears that the coverage of the nanorod array on the substrate increases as the precursor solution concentration increases. In addition, the nanorods grown with higher concentration precursor solution exhibited higher degree of alignment than the nanorods with lower concentration ones.

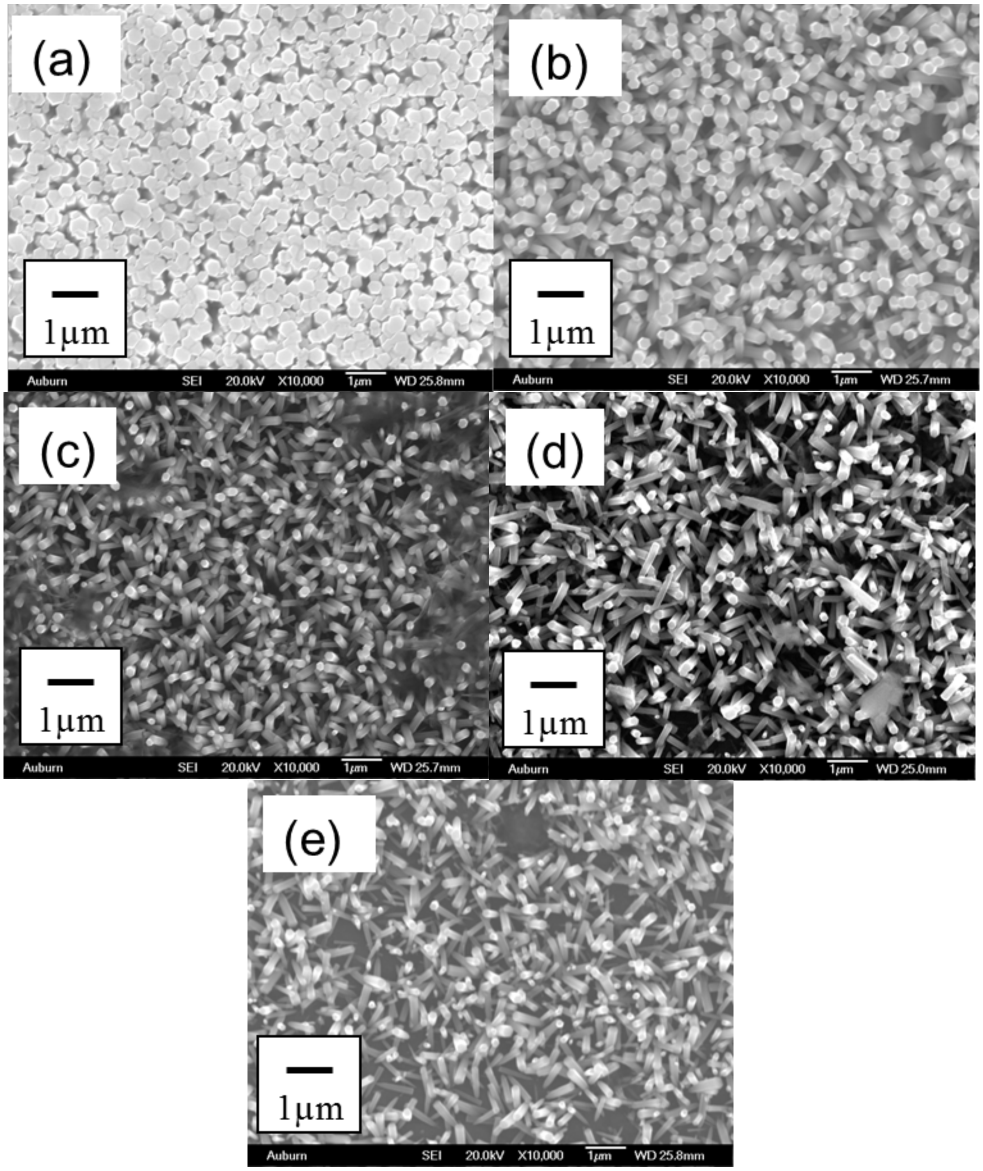

Figure 2.5.1 Top view SEM images (magnification: ×10,000) of ZnO nanorods synthesized on In_2O_3-PET substrates under different solution concentrations (scale bar – 1μm): (a) 50mM, (b) 37.5mM, (c) 25mM, (d) 18.75mM, (e) 12.5mM.

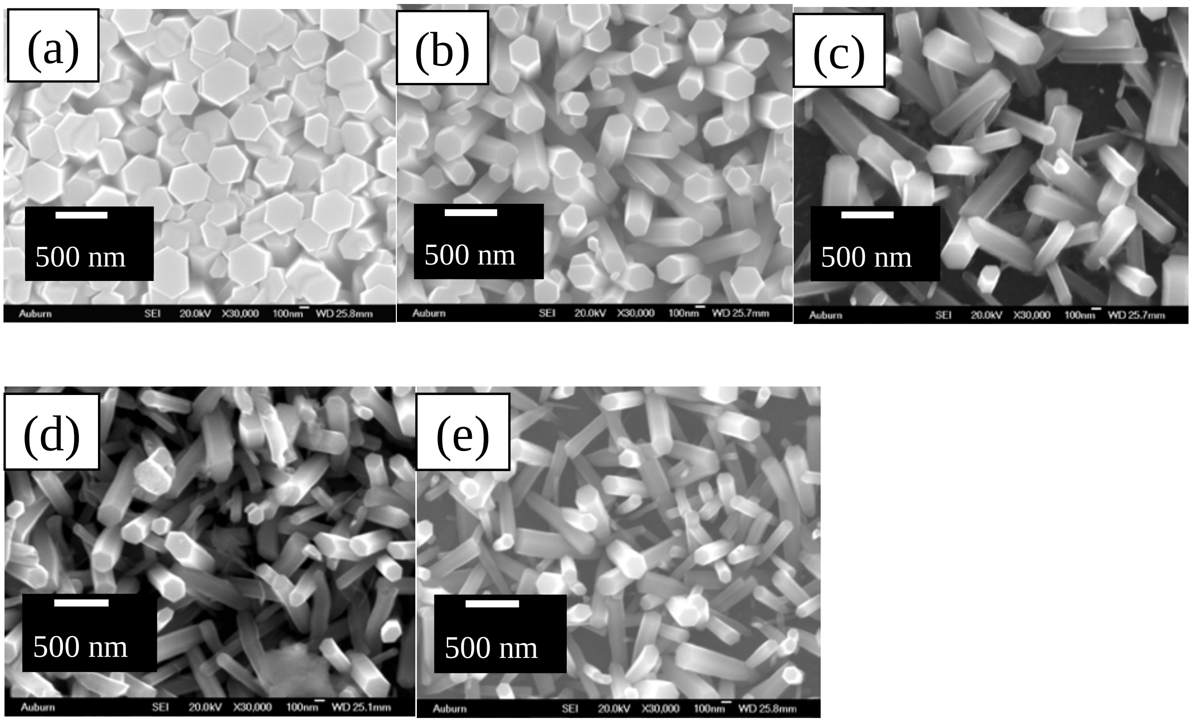

Figure 2.5.2 Top view SEM images (higher magnification: ×30,000) of ZnO nanorods synthesized on In_2O_3-PET substrates under different solution concentrations (scale bar – 500 nm): (a) 50mM, (b) 37.5mM, (c) 25mM, (d) 18.75mM, (e) 12.5mM.

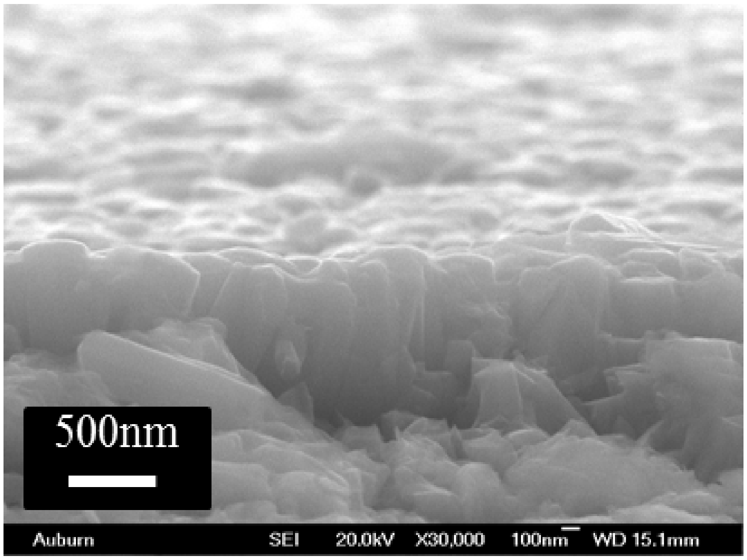

Figure 2.5.3 Cross sectional view SEM image of ZnO nanorods under solution concentration of 50mM (scale bar – 500 nm).

Solution con. (mM/L)	**50**	**37.5**	**25**	**18.75**	**12.5**
Average Diameter (nm)	397.4	265.8	251.1	225	173.6
Average length (nm)	1876.5	1148.5	875	780.9	600
Aspect ratio L/D	4.72	4.32	3.48	3.47	3.46

Table 2.5.1 The average diameter, length and aspect ratio ((length/diameter)) of ZnO nanorods on In_2O_3-PET flexible substrates under different solution concentrations

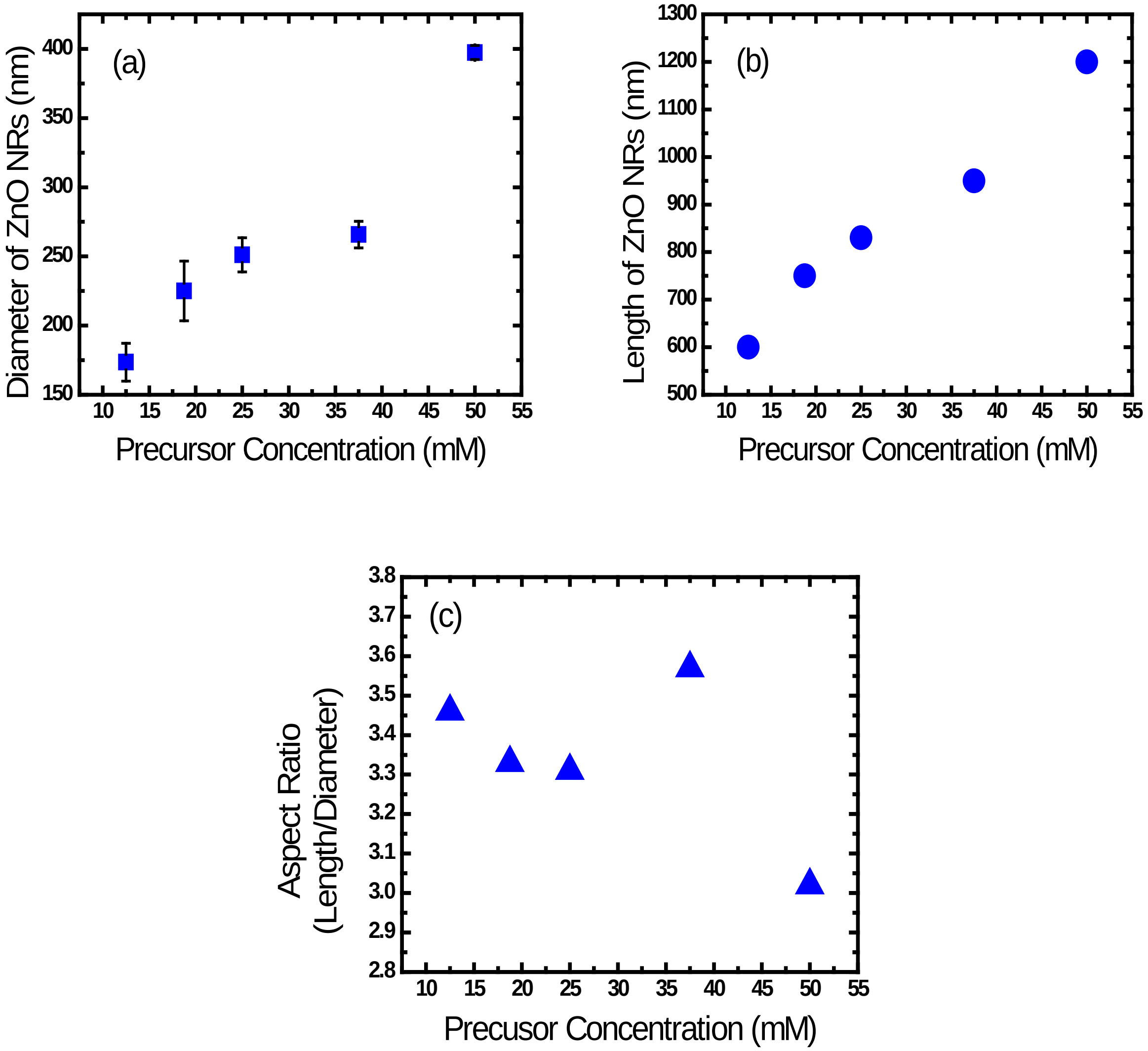

Figure 2.5.4 The plots of (a) average nanorod diameter, (b) average nanorod length, and (c) aspect ratio as a function of the solution concentration.

2.6 X-Ray Diffraction

X-ray diffraction is one of the most common tools for material characterization due to its reliability, simplicity and nondestructive nature. [51] The atoms of the crystal diffract the X-ray beam into many specific directions and from which we can determine the information of the crystal structure.

Bruker D8 X-ray Diffractometer was used to characterize the crystalline quality and orientation of the ZnO nanorods on In_2O_3-PET substrates. The XRD patterns of ZnO nanorods grown under different solution concentrations on In_2O_3-PET substrates are shown in Figure 2.6.1.

The XRD pattern of each sample was originated both from the ZnO nanorods and the In_2O_3-PET substrates. The X-ray diffraction result is in agreement with the standard diffraction pattern of hexagonal phase ZnO Wurtzite structure from the Joint Committee on Powder Diffraction Standards (JCPDS 36-1451)[52]. The diffraction peaks corresponding to the lattice planes (100), (002), (101), (102), (110), and (103) are indexed. In the case of the sample with the concentration of 50mM, the sharp and distinct diffraction peak at $2\theta=34.41°$ due to ZnO (002) crystal plane shows the strongest intensity, indicating its strong c-axis orientation and the nanorods are preferentially oriented perpendicularly to the substrate. The notable difference in the full-width at half-maximum (FWHM) strongly supports our speculation that ZnO nanorod crystal promotes along the [001] direction[53]. It was observed that the (002) diffraction peak becomes weak for concentration less that 25 mM, whereas the (100) peak becomes strong, showing its tendency toward random orientation. The (102) and (103) peak nearly disappear when the concentration is lower than 25 mM. Samples grown with solution concentration of 18.75 mM and 12.5 mM have worse morphology and thus results in the random orientation of nanorod arrays as observed in Figure 2.5.1.

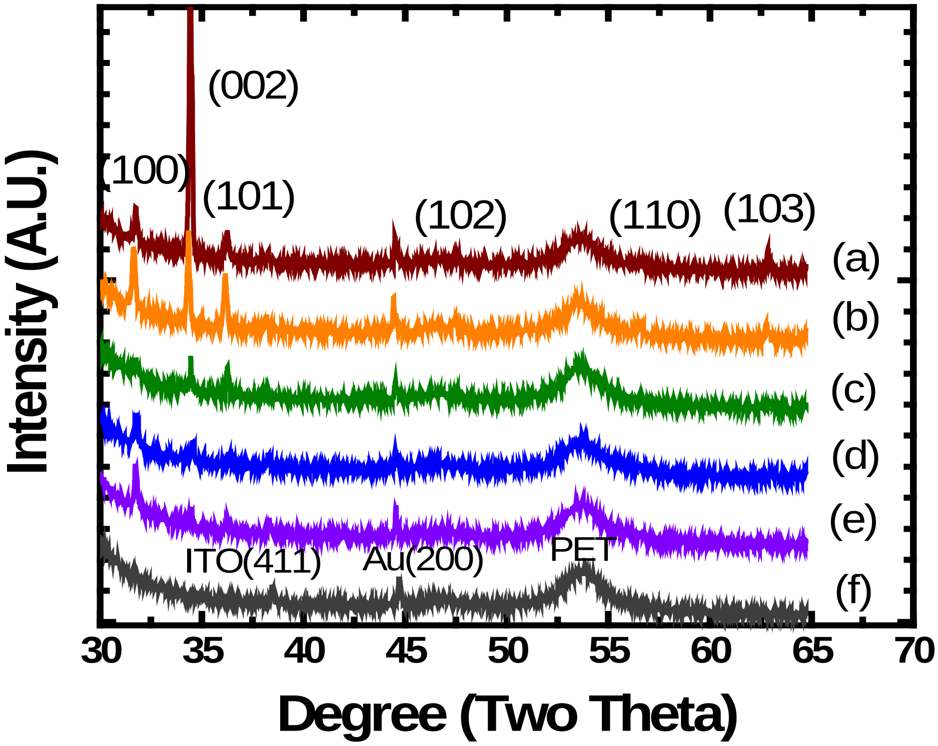

Figure 2.6.1 XRD patterns of ZnO nanorods grown on In_2O_3-PET substrates under different solution concentrations: (a) 50 mM, (b) 37.5 mM, (c) 25 mM, (d) 18.75 mM, (e) 12.5 mM and (f) bare In_2O_3-PET substrates.

2.7 Raman Spectroscopy and Photoluminescence

Raman characterization of electronic properties of materials is especially of great interest because it is a non-contact method and has a superior spatial resolution to the other methods. Room temperature Raman spectroscopy was conducted using the 441.563 nm He-Cd laser line (80mW). Figure 2.7.1 shows the schematic diagram of the Raman System. The Raman system is home- made equipped with a Jobin Yvon spectrometer and a thermally-cooled charge coupled device (CCD) detector (2048 by 512 pixels). The laser beam was focused onto a spot size with a diameter of of 5~10 µm. Lase enters the microscope through several reflective mirrors and illuminates onto the sample. A laser filter is applied to the entrance of the spectrometer to make sure that only the Raman signal be detected by CCD. The spectrometer contains two 3” holographic gratings with 2400 lines/mm and 3600 lines/mm groove densities, corresponding to resolution of 1 cm^{-1} and 0.2 cm^{-1}, respectively.

Micro-Raman spectroscopy was used to further analyze the quality of the ZnO nanorods. Wurtzite form of ZnO belongs to the space group C_{6v}^{4} with two formula units per primitive cell. [54] Group theory predicts the following optical modes at the Γ point of the Brillouin zone: $A_1 + E_1 + 2E_2 + 2B_1$. Among these modes, A_1, E_1 and $2E_2$ modes are Raman active, $2B_1$ modes are silent, and A_1 and E_1 modes are infrared active. Both A_1 and E_1 modes split into transverse optical (TO) and longitudinal optical (LO) phonons. [55]

Figure 2.7.2 shows the room temperature micro-Raman spectra (after baseline subtraction) collected from the five samples that were grown under different precursor concentrations and from the bare In_2O_3-PET substrate. Lorentzian functions were employed to fit the Raman spectra in the region between 300 and 600 cm-1. The observed peaks at about 438 and 586 cm^{-1} are assigned to be $E_2^{(2)}$ (high frequency E_2 mode) and Quasi-LO (QLO), respectively. [56,57, 58] The peak at 329 cm^{-1} results from the multiple phonon scattering processes. [59] As can be seen from Figure 2.7.2, the intensities of the ZnO Raman peak become higher as the precursor concentration increases, which indicate the increase in the crystal quality of the nanorods and/or the increase in the coverage of the nanorod arrays on the substrate. The Raman scattering result is in agreement with the X-ray and photoluminescence analyses.

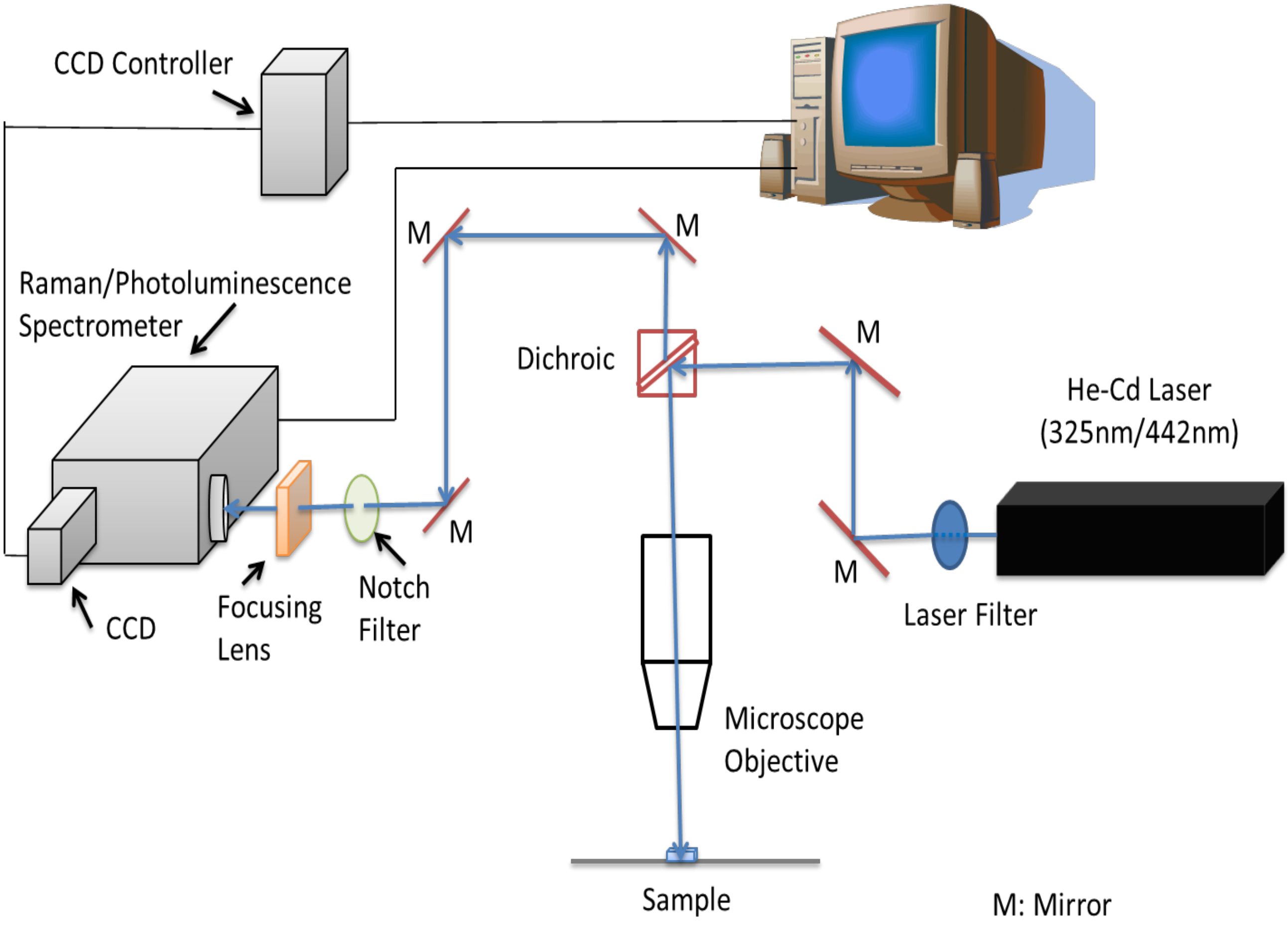

Figure 2.7.1. Schematic diagram of the Raman System.

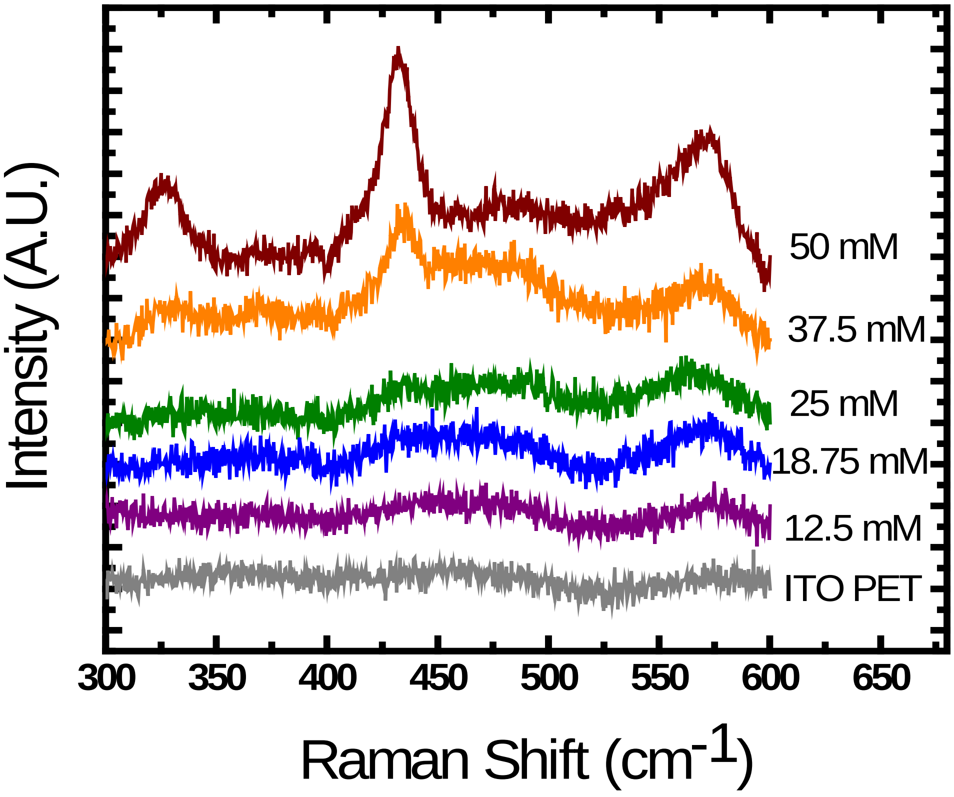

Figure 2.7.2. Raman scattering spectra of ZnO nanorods synthesized on In_2O_3-PET substrates under different precursor concentrations: 50 mM, 37.5 mM, 25 mM, 18.75 mM, 12.5 mM and bare In_2O_3-PET substrates.

Photoluminescence (PL) is a phenomenon that the substance absorbs light/photons and reradiates photons. And similar to Raman spectroscopy, PL is a non-contact, non-destructible optical method for diagnosing materials. From the PL spectra, we can elucidate the crystal quality, defects information from the position, intensity, and width of the PL peak. For wide band gap semiconductors such as ZnO and GaN, there are usually two peaks from the PL spectra: a narrow and UV near band edge (NBE) peak and a broad visible peak.

In this study, Photoluminescence measurement was employed to study the influence of precursor solution concentration on the optical property of the ZnO nanorods grown on In_2O_3-PET substrates. Room temperature PL spectra were collected using the 325 nm line (20mW) from a continuous-wave He-Cd laser.

Room temperature PL spectra from the ZnO nanorods grown under various precursor concentrations and from the bare ITO coated PET substrate are shown in Figure 2.7.3. The PL spectra from the ZnO nanorods typically exhibit two bands: a strong and sharp peak at about 385 nm (3.22 eV, UV emission) and a broad band at around 530 nm (2.34 eV, visible emission). The former is a typical near band edge transition of intrinsic ZnO, and is related to excitonic process.[60,61,62] The latter visible band is considered to be resulted from the impurities and/or structural defects such as singly ionized oxygen vacancies in ZnO. [63,64] The PL spectra of the ZnO nanorods grown from the solution with the lowest precursor concentration of 12.5mM were mainly dominated by peaks of the bare In_2O_3-PET substrates, which indicate that the coverage of the ZnO nanorods on the In_2O_3 surface is substantially low. As can be seen from the PL spectra, the contribution from the ZnO becomes dominant as the precursor solution concentration increases.

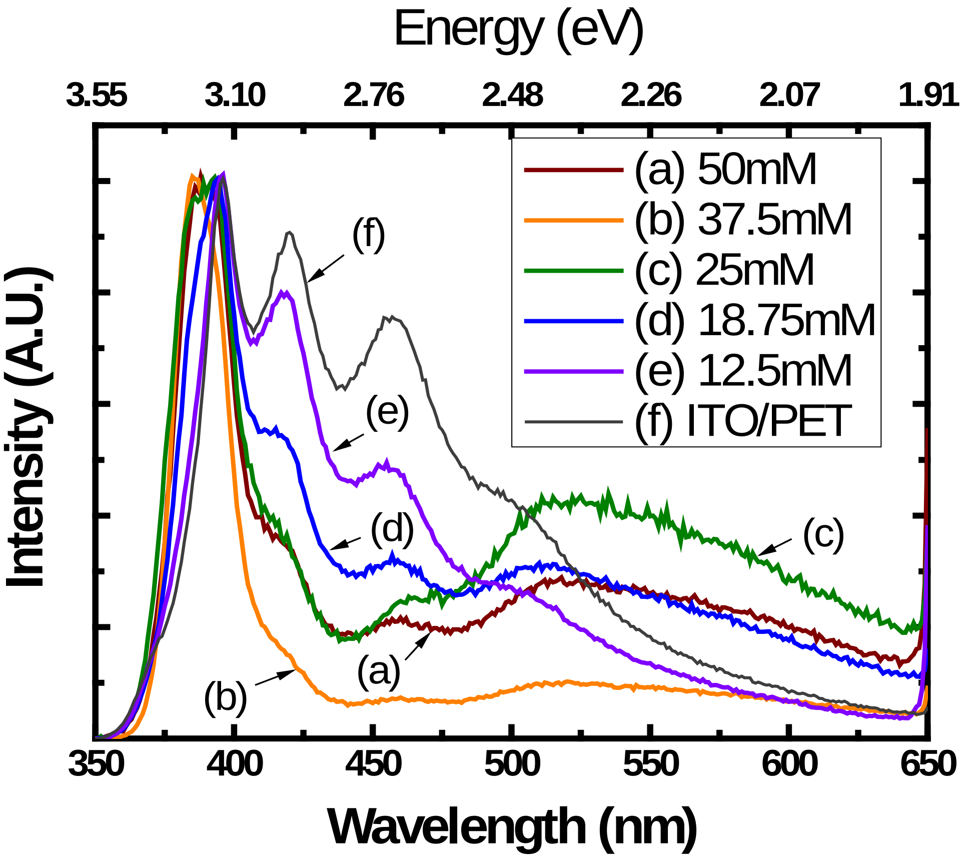

Figure 2.7.3 PL spectra of ZnO nanorods synthesized on In_2O_3-PET substrates under different precursor concentrations: (a) 50 mM, (b) 37.5 mM, (c) 25 mM, (d) 18.75 mM, (e) 12.5 mM and (f) bare In_2O_3-PET substrates.

2.8 Summary and Conclusions

In summary, optimization of solution processing of ZnO nanorods with length about 300nm for efficient charge collection in hybrid photovoltaic devices. We have systematically studied the effect of precursor solution concentration on the materials quality, orientation, and optical property of the ZnO nanorods grown on flexible In_2O_3-PET and ITO-glass substrates. Our investigation demonstrates that the morphology, crystal orientation and optical property of ZnO nanorods grown on In_2O_3-PET substrates can be tailored by changing the concentration of the precursor solution. By tuning the precursor concentration, we can grow nanorods with different morphology, crystal quality, and orientation. X-ray diffraction and mirco-Raman spectroscopy showed that the ZnO nanorods with the highest concentration of 50 mM were highly aligned and has the highest level of surface coverage. It was also found that the diameter and length of the nanorods increases upon increasing precursor solution concentration. To the best of our knowledge, this is the first systematic investigation of studying the effect of precursor solution concentration on quality of ZnO nanorods grown on In_2O_3-PET substrates by low-temperature solution method. We strongly believe that our work will contribute to the realization of flexible organic-inorganic hybrid solar cell based on ZnO nanorods and polymer.

2.9 Future Work

In theory, vertical nanorods will result in enhanced device performance than the inclined nanorods. It will be interesting to grow vertical and aligned ZnO nanorods by using porous alumina templates which then could be applied to photovoltaic devices, LEDs, and photoreceptors. Porous alumina template is a very popular and effective way in growing aligned and perpendicular nanomaterial on the substrates.

CHAPTER 3

Fabrication and Characterization of Hybrid Photovoltaic Devices

3.1 Introduction

As discussed in chapter 1, inorganic semiconductor based solar cell such as Si photovoltaic technology has become relatively mature, yet they suffer the problem of high cost and inflexibility. Organic solar cells, which offer the advantage of low cost, flexibility, light weight, and tunable band gap is very promising in the applications of sunlight energy conversion. However, organic solar cells can be greatly improved by introducing in the inorganic nanomaterial semiconductor, which will greatly help in the charge collection, transportation and device stability.

In this chapter, ZnO nanorod arrays integrated organic bulk heterojunction hybrid solar cells were fabricated and the detailed fabrication and characterization process of these organic-inorganic photovoltaic devices will be discussed. Figure 3.1 shows the flow chart of the overall fabrication process of ZnO nanorod arrays integrated organic bulk heterojunction hybrid solar cells.

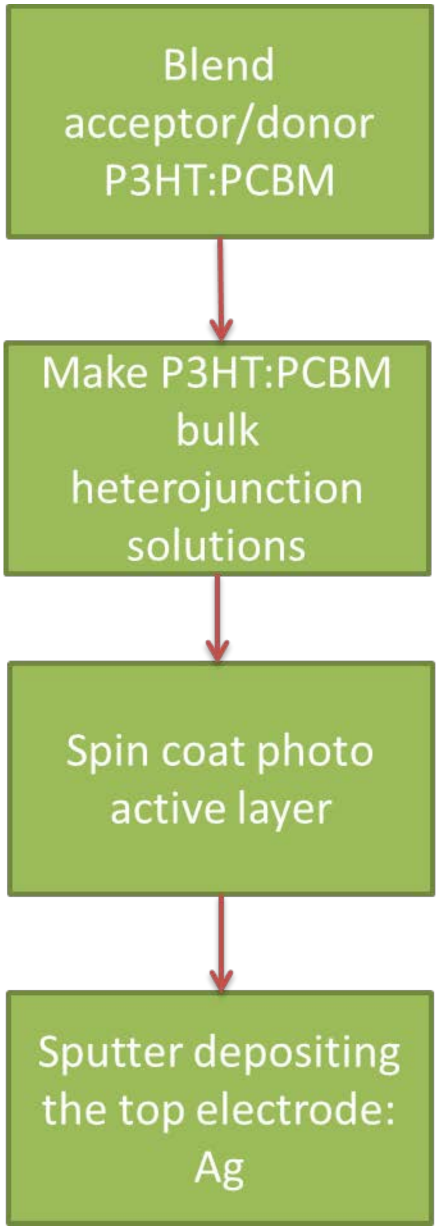

Figure 3.1 Flow chart of the overall fabrication process of ZnO nanorod arrays integrated organic bulk heterojunction hybrid solar cells.

3.2 Preparation of Organic Solution

Regioregular Poly (3-hexylthiophene-2,5-diyl) (P3HT) was purchased from Rieke Metals (4002-EE). The average molecular weight of the P3HT is 50,000 M.W. (6,6)-phenyl C61 butyric acid methyl ester (PCBM) was purchased from Sigma-Aldrich. As a solvent for the blend of P3HT and PCBM, 1,2-Dichlorobenzene (anhydrous, 99%), purchased from Sigma-Aldrich, was used. Olson et al.[65] reported that using dichlorobenzene instead of chloroform as the solvent for P3HT led to enhanced infiltration, polymer order, and device performance.

For the preparation of the bulk heterojunction photoactive layers, the blend of 50 mg P3HT and 30 mg PCBM was dissolved in 2 mL 1,2-Dichlorobenzene. In the fabrication of BHJ organic solar cells, the most often employed ratio of P3HT:PCBM is 1:1, 5:4 and 5:3. Moulé *et al.* [66] have investigated the composition ratio of the donor and acceptor materials and concluded that it depends on the active layer thickness in a predictable manner. Lee *et al.* [67]have conducted both theoretical simulation and experimental work to investigate different P3HT:PCBM weight ratios and concluded that 1:1 ratio yield the highest interface to volume ratio and the most balanced charge carrier transport in both the P3HT and PCBM phases.

Then, the solution was stirred using magnetic stirring bar (shown in Figure 3.2) at about 40 °C for 20 min and was subsequently stirred at room temperature for 24 hrs. The reason of using as little as 2 mL 1,2-Dichlorobenzene to dissolve 80 mg blend of P3HT and PCBM is as follows: firstly, to fasten the evaporating process after spin coating the photoactive layer, which is discussed in sec 3.2; secondly, as described in the next section, since spin coating is chosen as the method of depositing organic active layer, the organic solution cannot be dilute. And since the solution is highly concentrated, to make sure that the solution is completely dissolved, heating in the beginning and stir for as long as a day is important. The solution was kept in a brown color bottle since P3HT and PCBM are light sensitive material.

Figure 3.2 Magnetic stirring bar.

3.3 Spin Coating Organics

The solution of P3HT:PCBM blends (P3HT:PCBM ratio is 5:3) was later spin-coated onto the ZnO nanorods at a low spinning rate of 400 rpm for 1 min to achieve slow drying effect for the fully polymer infiltrated ZnO nanorod arrays. Then, the as-prepared samples were dried slowly at room temperature in air for 1 hr. Figure 3.3 shows the spinner used in this experiment.

Quality of the interface between the organic polymer and the inorganic nanostructured oxide is crucial for the PV device performance.[68,69,70,71] Full infiltration of the polymer into ZnO nanorods network plays an important role in the performance of the hybrid photovoltaic device.[21,65] Low spinning rate as slow as 400 rpm and slow drying process were found to be effective in enhancing the infiltration of the polymer into nanorods, increasing the polymer solidification time, , and thus improving the performance of the photovoltaic device.[14]

The ZnO nanorods and the extremely small amount solvent (1,2-Dichlorobenzene) makes non-annealing possible. The non-annealing feature after spin coating the photoactive layer not only simplifies the fabrication procedure, but also is particular suitable for the fabrication of the flexible organic or organic-inorganic hybrid solar cells that build on plastic substrates since the flexible substrates such as PET film cannot resist temperatures above 150 °C.

Figure 3.3 Spin coater.

3.4 DC Sputtering Top Electrode

Finally, as the top electrode, a 100 nm thick, circular pattern of Ag was sputtered through a shadow mask on top of the sample. Figure 3.4.1 shows the DC magnetron sputter system used in depositing silver top electrode. The homemade sputter system consists of a cylindrical vacuum chamber connected to a roughing and a diffusion pump. The silver target with purity of 99.99% and diameter of 2" was purchased from Kurt J. Lesker Company. The samples were located at a distance of 4" from the target. Prior to sputtering, a base vacuum pressure of 4×10^{-7} Torr was achieved. Then, Ar was introduced into the chamber at a flow rate of 100 sccm (standard cubic centimeters per minute) and a pressure of 18 mTorr. The gaseous plasma was generated by high voltage DC power supply. The sputtering current and voltage were maintained at 0.2 A and 310 V, respectively. Sputter deposition time was 3 min. During sputtering, the temperature of the substrate was maintained at room temperature.

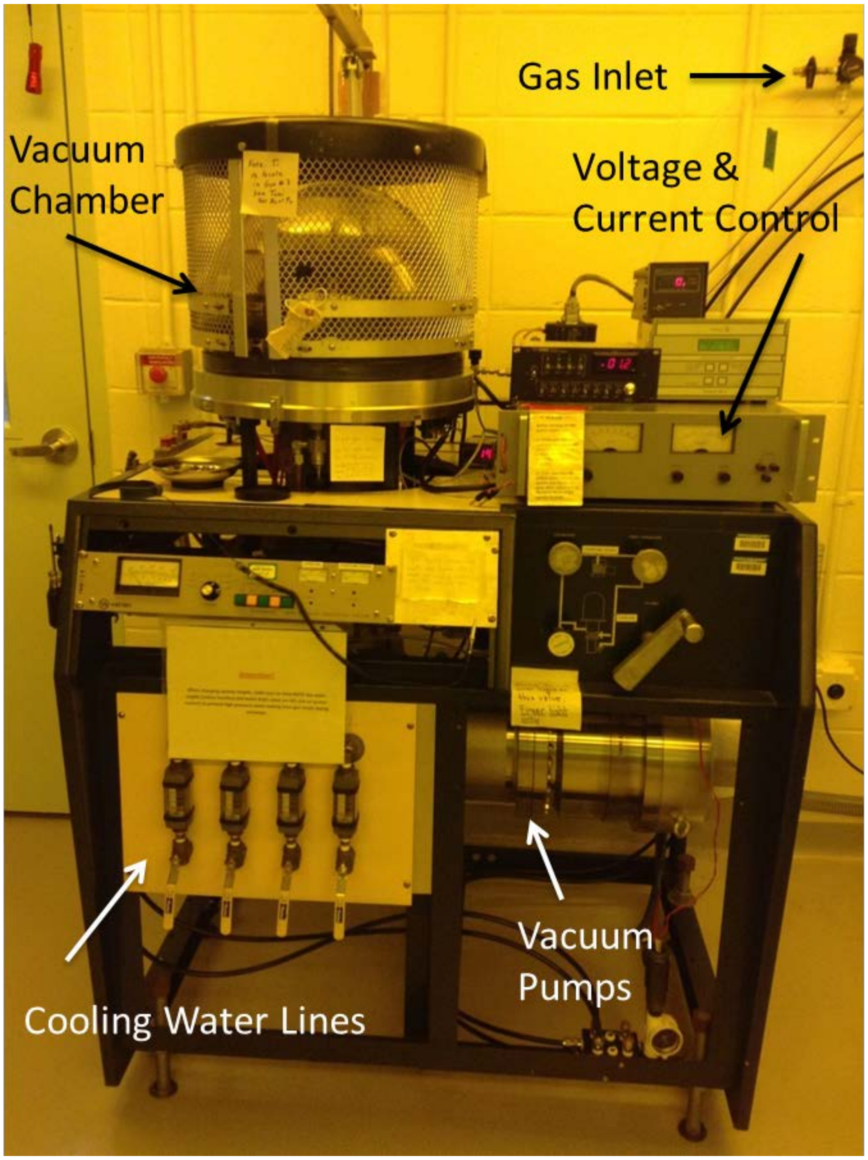

Figure 3.4.1 DC magnetron sputtering system.

As shown in Figure 3.4.2, the shadow masks used in this experiment has circular holes of different diameters: 8mm, 6 mm, and 4 mm which results in different device areas. Figure 3.4.3 shows the schematic device structure of the fabricated ZnO NRs integrated organic BHJ cells. And the reason we chose Ag instead of Al which is typically used in the fabrication of organic solar cells is that Ag has higher work functions (Figure 3.4.4) than ITO, so the photoelectrons flows from Ag to ITO. In the typical organic bulk heterojunction (BHJ) photovoltaic devices (Figure 3.4.5) such as ITO/PEDOT:PSS/organic layer/Al, photoelectrons flow from ITO to Al. Figure 3.4.6 and Figure 3.4.7 shows the photographs of fabricated hybrid PVs on rigid and flexible substrates.

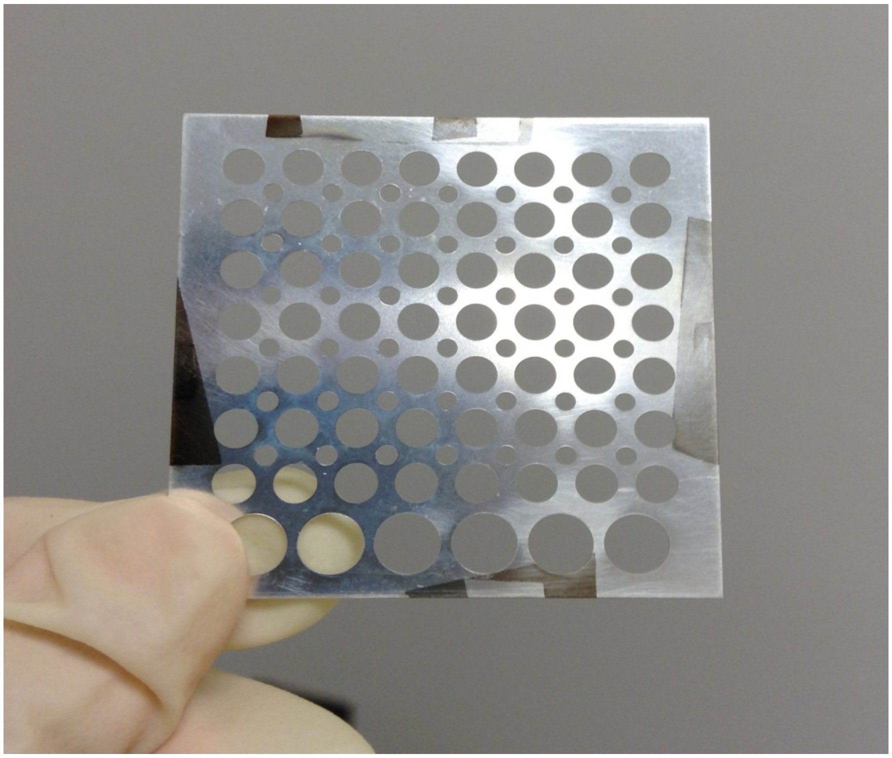

Figure 3.4.2 Shadow masks used in sputtering top electrode Ag.

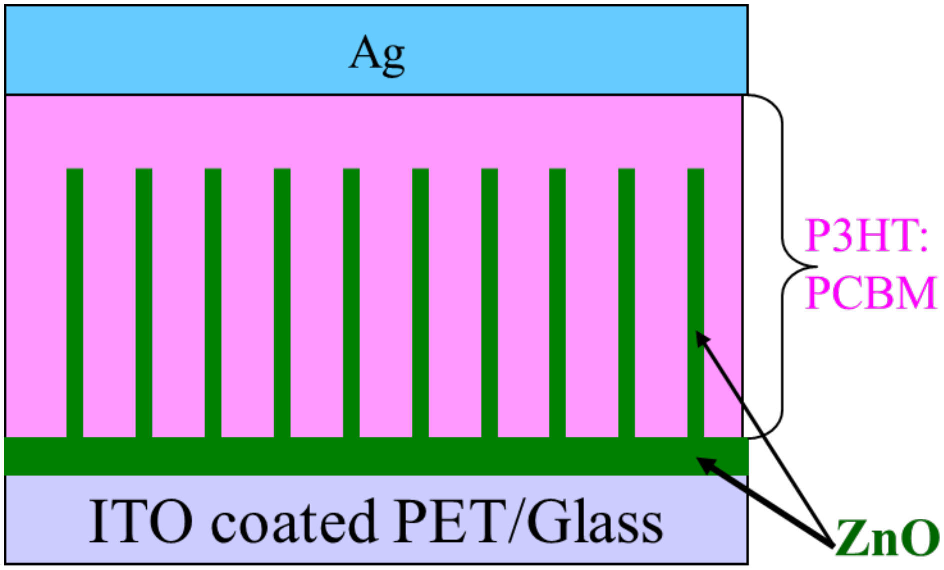

Figure 3.4.3 Schematic representation of ZnO NRs integrated organic BHJ solar cells.

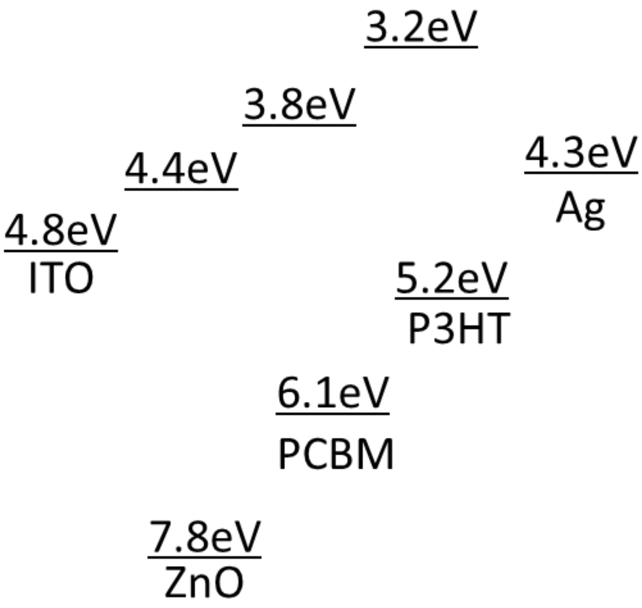

Figure 3.4.4 Energy diagram of ZnO NRs integrated organic BHJ solar cells.[12]

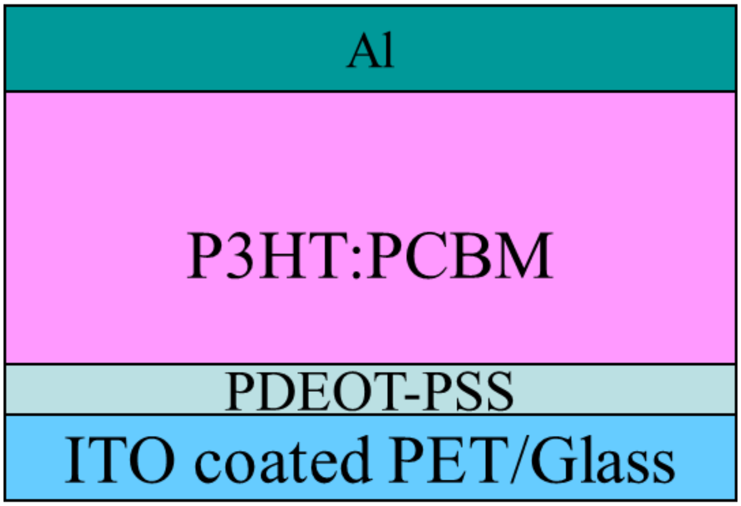

Figure 3.4.5 Typical organic BHJ photovoltaic devise structures.

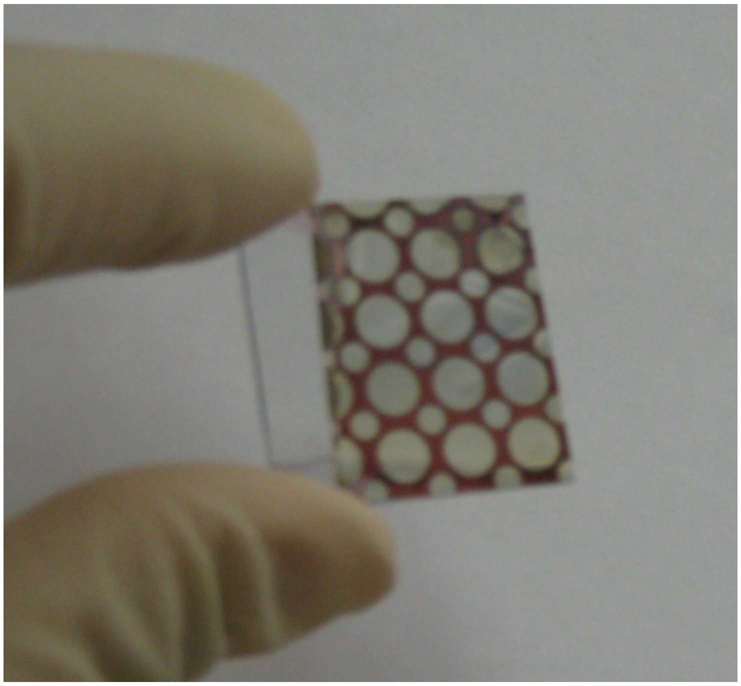

Figure 3.4.6 Solar cells fabricated on ITO-glass.

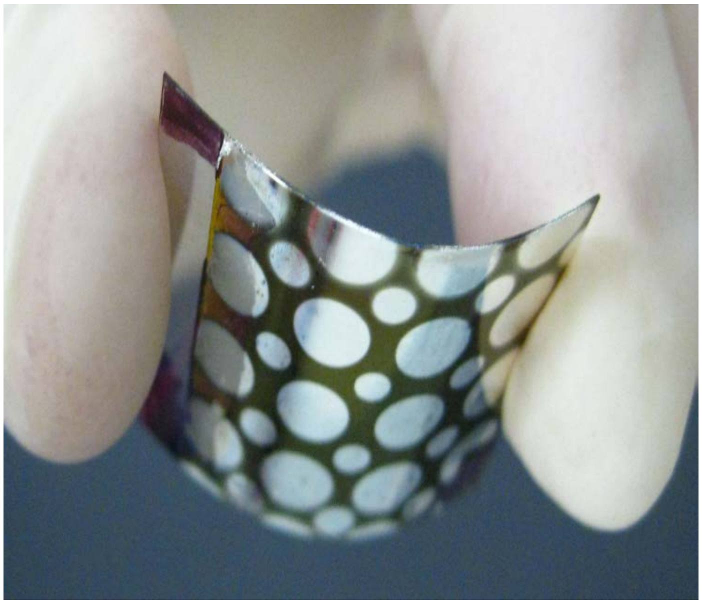

Figure 3.4.7 Solar cells fabricated on In_2O_3-PET.

3.5 Solar Cell Testing

The photovoltaic properties of the solar cell were tested using an Apex 150 W Xenon lamp with an AM 1.5G filter. Figure 3.5.1 shows the schematic solar cell testing system set up. A mirror was used to direct the light from Xenon lamp upwards to shine on the bottom of the ITO substrates of the hybrid solar cells. A probe station that is connected to the voltage source pico-ammeter was employed to test the samples. A photomask (Figure 3.5.2) which makes the area of light illumination equal to that of the active electrode area of photovoltaic device was employed. The active device area is 0.1 cm^2. The power of the incident light was measured by optical power meter (Newport, Model 1815-C). The intensity of the incident light illuminated on the device was 100 $mW\text{-}cm^{-2}$. The Current-Voltage (*I*-*V*) characteristics of the photovoltaic devices were measured using Keithley 6487 Pico-ammeter/voltage source. To make sure that the light illumination area only illuminates one active device area, photo mask with a hole of diameter 6 mm was used.

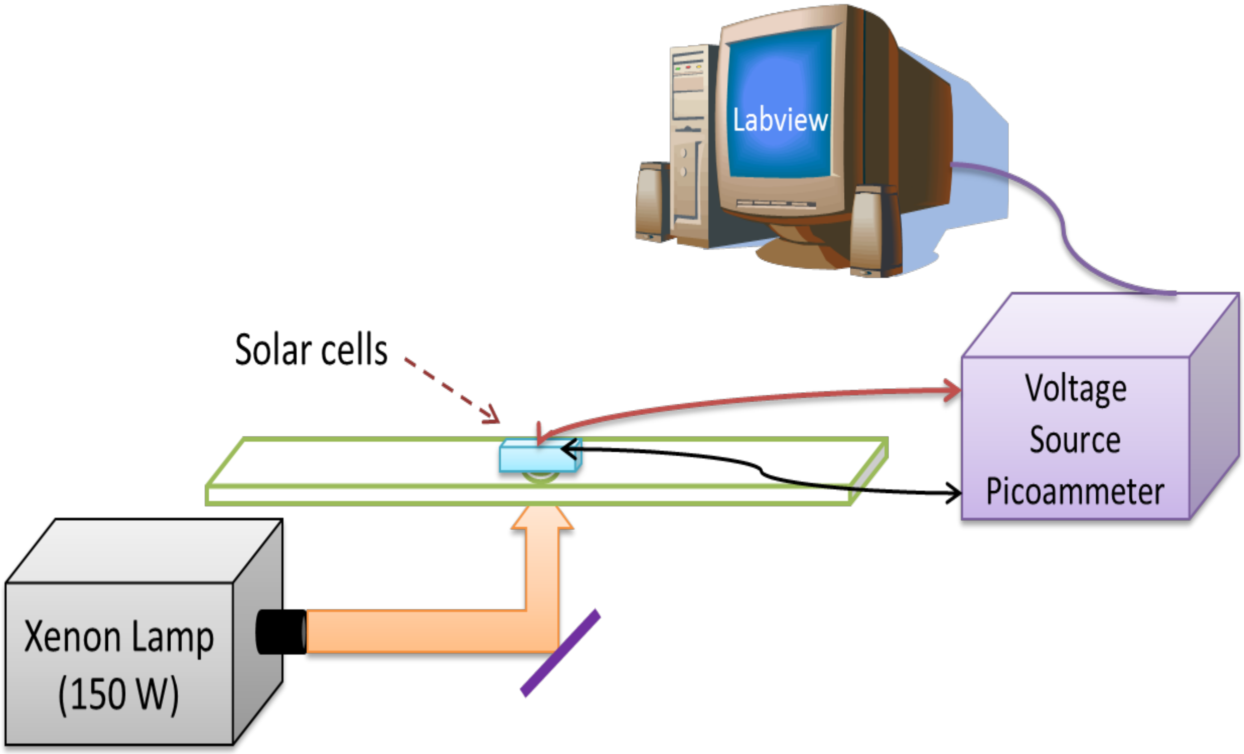

Figure 3.5.1 Solar Cell Testing System

From the Current-Voltage (I-V) characteristics, we can first can get important parameters of the photovoltaic device: open circuit voltage (V_{OC}), short circuit current (I_{SC}), and P_{max}. Where V_{OC} is the potential difference between the two terminals of the solar cell when there is no external load/current.; I_{SC} is the current value when the voltage across the solar cell is zero (the solar cell is short circuited); P_{max} is the maximum power point from the I – V curve. Then the power conversion efficiency (η) can be calculated according to equation (3.5.1), where P_{in} is the input power (100 mW/cm^2) and fill factor (FF) can be calculated according to equation (3.5.2).

$$\eta = \frac{P_{\max}}{P_{in}} \tag{3.5.1}$$

$$FF = \frac{P_{\max}}{J_{SC} \times V_{OC}} \tag{3.5.2}$$

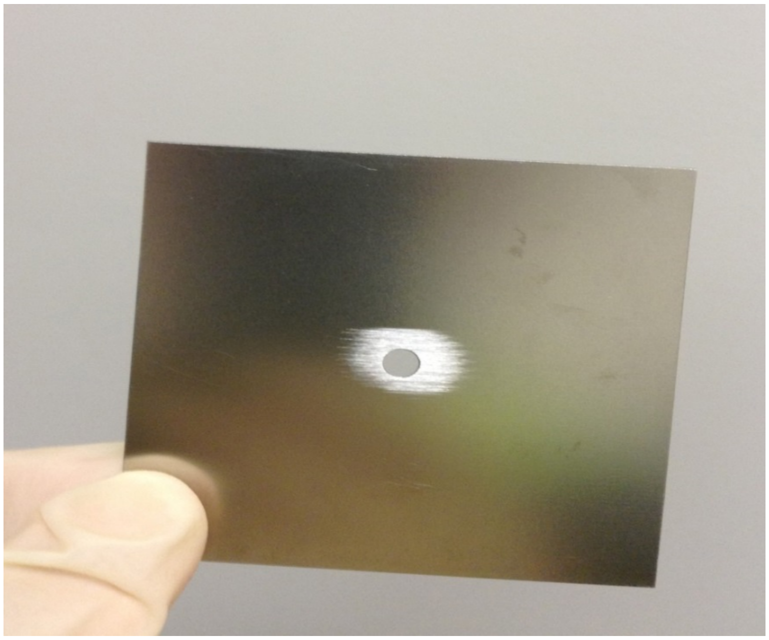

Figure 3.5.2 Photo-mask used in solar cell testing.

3.6 Results and Discussion

For flexible photovoltaic devices, fabrication process at low temperature is crucial since most of the flexible substrates are unstable at temperature above 150 °C. In this experiment, the ZnO nanorods were synthesized at 85 °C. As described in the previous chapter, the diameter and length of the ZnO nanorods can be controlled by changing growth parameters such as growth time and solution precursor concentration[12, 50]. Takanezawa *et al.* [12] have investigated the influence of the length of ZnO nanorods on the device performance and they concluded that longer nanorod length attribute to the improved performance of the hybrid photovoltaic device. However, in the following year's paper of Takanezawa *et al.*[72], they found that longer ZnO nanorods have some adverse effects on the generation of charge carriers and the power conversion efficiency reaches saturation as the length of the ZnO nanorod increases. In our experiment, we choose solution precursor concentration 25 mM and time duration 100 min as the optimized solution growth parameters for growing the desired ZnO nanorods for the flexible hybrid solar cell.

The photovoltaic devices with a structure of PET/ITO/ZnO thin film/ZnO nanorods/P3HT:PCBM/Ag, as shown in figure 3.3.3, were fabricated. In this device structure, photons can be absorbed either by ZnO nanorods or the conjugated polymer, and excitons can also be generated in either layer. However, the dominant role of ZnO nanorods is for collecting and transporting the charge carries than serving as the n type doping semiconductor material. In the P3HT:PCBM blended bulk heterojunction photoactive layer, the acceptor/donor interfaces (and thus the charge separation sites) are located randomly everywhere, an exciton is easy to reach to a neighboring acceptor/donor interface and dissociated into charge carriers[1]. ZnO nanorods, as an additional electron acceptor layer, play an important role in rapidly collecting and transporting electrons to the transparent electrode ITO. And the besides serving as seed layer, ZnO thin film also block the holes.

Quality of the interface between the organic polymer and the inorganic nanostructured oxide is of great importance for the PV device performance.[13,69,70,71] Full infiltration of the polymer into ZnO nanorods network plays an important role in the performance of the hybrid photovoltaic device.[21,65] Liu *et al.*[78] reported that using dichlorobenzene as the solvent for P3HT instead of chloroform led to enhanced infiltration, polymer order, and device performance. Low spinning rate such as 400 rpm and slow drying process were found to be effective in increasing the polymer solidification time, enhancing the infiltration of the polymer into nanorods, and thus improving the performance of the photovoltaic device.[73]

Figure 3.6.1 and Figure 3.6.2 shows the dark and photo (orange curve with squares) current density vs. voltage (J-V) characteristics of the as-fabricated hybrid photovoltaic device with the device structure of ZnO thin film/ZnO nanorods/P3HT:PCBM/Ag on flexible In_2O_3-PET and rigid ITO/glass, respectively. As shown in Figure 3.6.1, under AM 1.5G illumination of light with a power density of 100 mW cm^{-2}, the device on the flexible substrate exhibited an open circuit voltage (V_{OC}) of 0.52 V, a short circuit current density (J_{SC}) of 9.82 mA cm-2, a fill factor (*FF*) of 35%, and a power conversion efficiency (PCE) η of 1.78%. It is noteworthy that high JSC (about 10 mA cm-2) and V_{OC} larger than 0.5 V was obtained, which is comparable to the bulk heterojunction P3HT:PCBM organic solar cells reported by several research groups.[74,75,76,77] Further work is in progress in order to achieve higher efficiencies and to enhance performance for this type of device structure. Whereas the device on rigid ITO/glass substrate yield an open circuit voltage (V_{OC}) of 0.38 V, a short circuit current density (J_{SC}) of 9.14 mA cm-2, a fill factor (*FF*) of 29%, and a power conversion efficiency (PCE) η of 0.99%. Thus our flexible device showed better device performance than that of the rigid device. Table 3.6 summarizes the Solar cell testing parameters and results from Figure 3.5.1 and Figure 3.6.2. As a reference, we tested the I-V characteristics of Si solar cell (Figure3.6.3) using our solar cell testing system. The photo I-V curve (orange colsed squares) ehixibit the typical square curve of Si solar cell. And about 3% power conversion efficiency was achieved in this Si solar cell.

Substrates	power conversion efficiency (PCE) η	fill factor (FF)	open circuit voltage (V_{OC})	short circuit current density (J_{SC})
In_2O_3-PET	1.78%	35%	0.52 V	9.82 mA/cm^2
ITO/Glass	0.99%	29%	0.38 V	9.14 mA/cm^2

Table 3.6 Solar cell testing parameters and results.

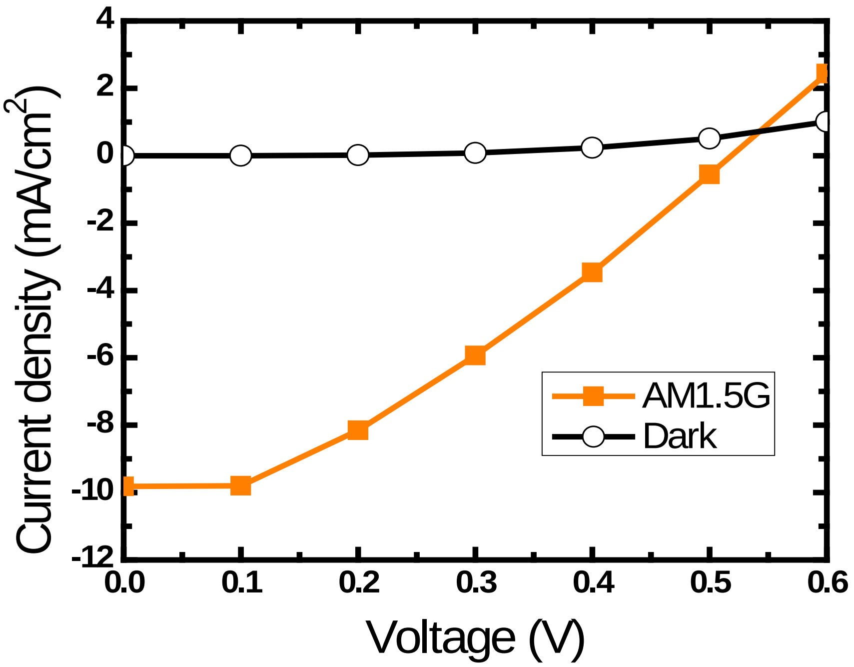

Figure 3.6.1 *J-V* characteristics for the P3HT:PCBM/ZnO nanorods photovoltaic device on flexible In_2O_3-PET substrates (open circles: dark, closed squares: AM 1.5G illumination).

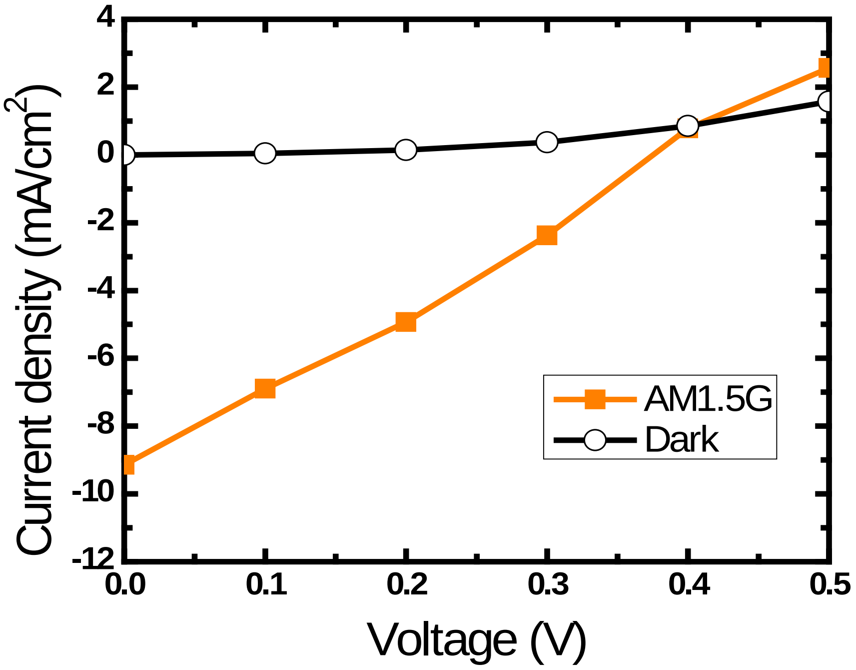

Figure 3.6.2 *J*-*V* characteristics for the P3HT:PCBM/ZnO nanorods photovoltaic device on rigid ITO-glass substrates (open circles: dark, closed squares: AM 1.5G illumination).

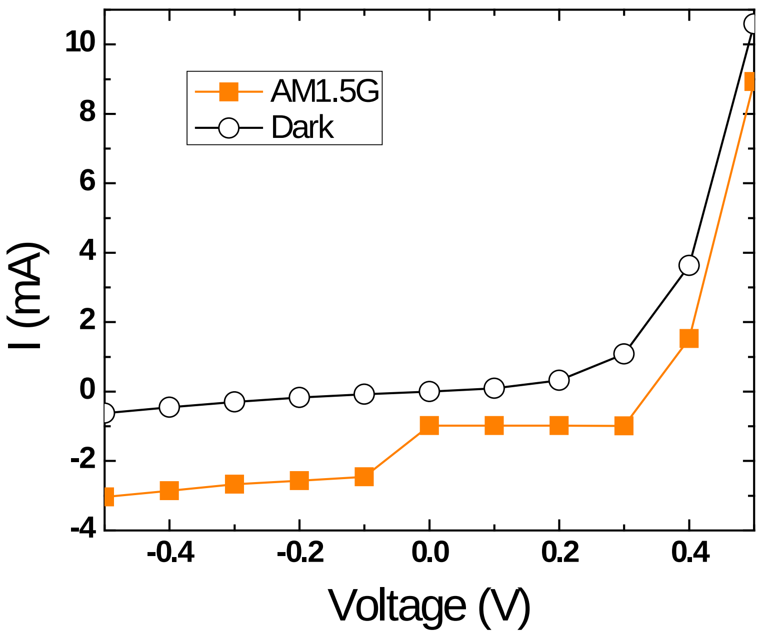

Figure 3.6.3 *I-V* characteristics of the reference Si solar cell (open circles: dark, closed squares: AM 1.5G illumination).

To investigate the role of the fullerene PCBM, the photovoltaic devices with the structure of PET/ITO/ZnO thin film /ZnO nanorods/P3HT/Ag were fabricated. Figure 3.6.4 shows the dark and photo current density vs. voltage (*J-V*) characteristics of such PV device. This device exhibited a V_{OC} of 0.25 V, a J_{SC} of 1.2 mA-cm^{-2}, a *FF* of 33%, and a PCE of 0.1%. And to compare with the device has PCBM, the two J-V curves are plotted in Figure 3.6.5. It can be seen that the J_{SC} is more than eightfold and the PCE is more than 17 times improved by using the blend of P3HT:PCBM instead of just using P3HT in constructing hybrid solar cell.

Analogous to the fabrication of the third generation organic solar cells which were categorized as “bulk heterojunction” or BHJ cells, using the blend of donor (e.g. P3HT) and acceptor (e.g. PCBM) instead of the second generation which feature the donor/acceptor double layer cells, hybrid solar cells which contain the blend of P3HT and PCBM remain the advantage that excitons can easily reach the donor/acceptor interface and be dissociated into charge carriers. According to the recent studies, the blend of P3HT and PCBM exhibited near unity photo-induced charge separation (internal quantum efficiency) at donor/acceptor interface. Liu et al.[78] conducted photoluminescence experiment to compare the exciton dissociation efficiency of P3HT: PCBM to P3HT/ZnO, and they found that the exciton dissociation occurs at the interface between P3HT:PCBM instead of that between P3HT and ZnO nanorods.

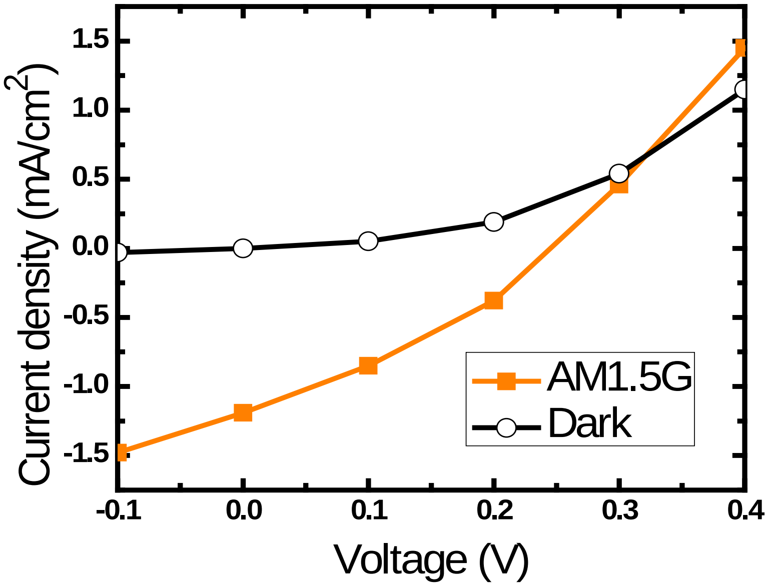

Figure 3.6.4 *J-V* characteristics of the P3HT: ZnO nanorods photovoltaic device

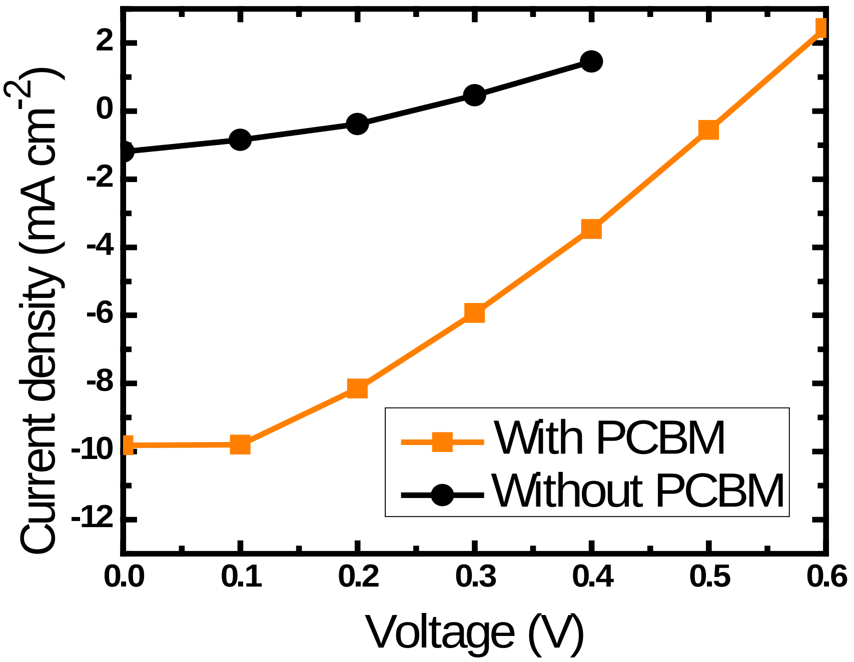

Figure 3.6.5 *J-V* characteristics for the hybrid solar cell with the photovoltaic device structure of PET/ITO/ZnO thin film/ZnO nanorods/P3HT:PCBM/Ag (squares) and for the PV device with the device structure of PET/ITO/ZnO thin film /ZnO nanorods/P3HT/Ag (circles).

And to investigate the role of ZnO nanorods, solar cells with only ZnO seed layer and without ZnO nanorods were fabricated. Figure 3.6.6 shows the dark and photo current density vs. voltage (*J-V*) characteristics of the solar cell with the device structure of P3HT:PCBM blend / ZnO thin film. Without ZnO nanorods, the *J–V* curve exhibit blocking behavior, and thus the short circuit current and power conversion efficiency are both low. This result indicates the importance role of ZnO nanorods: collecting and transferring charge carriers.

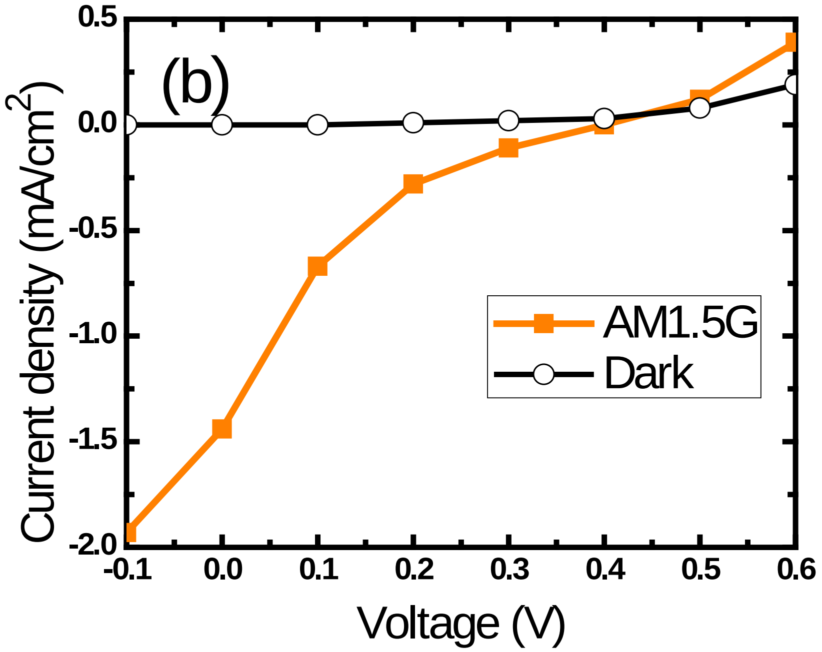

Figure 3.6.6 P3HT:PCBM /ZnO thin film PV device (open circles: dark, closed squares:AM1.5G illumination).

3.7 Summary and Conclusions

In summary, air-stable - preparation and operation in air, polymer ZnO nanorod hybrid solar cell were successfully fabricated on ITO-glass and In_2O_3-PET substrates. Bulk heterojunction P3HT:PCBM / ZnO nanorod array photovoltaic devices flexible and rigid substrates. The performance of polymer ZnO nanorod hybrid solar cells were improved by slow drying (400 or 600 rpm polymer spin rate and no annealing involved) of the photoactive layer.

The best device showed a short circuit current density (J_{SC}) of 9.82 mA cm-2, an open circuit voltage (V_{OC}) of 0.52 V, and a fill factor (*FF*) of 35%, resulting a PCE (η) of 1.78%. To the best of our knowledge, this is the first report and investigation of the fabrication and characterization of flexible organic/inorganic hybrid solar cells based on conjugated polymer and ZnO nanorods.

3.8 Future Work

It is of interest to apply the hybrid solar cell fabrication technique to make photovoltaic devices on other transparent substrates such as leaves and paper. Enhancing hybrid solar cell device efficiency, fill factor, I_{SC} and V_{OC}. Methods include optimizing the ZnO nanorod quality for efficient charge collection and lengthening the polymer solidification time to improve the performance of polymer ZnO nanorod hybrid solar cells. Details include optimizing the ratio of P3HT to PCBM, PCBM interlayer spinning rate and annealing temperature. Moreover, it is important to Optimization of the air stability of the hybrid solar cells. I also would like to grow Graphene on plastic substrates and apply into Graphene cathode based ZnO nanorods organic hybrid solar cells.

CHAPTER 4

Fabrication and Characterization of AlGaN/GaN HEMT

4.1 Introduction

Wide Bandgap semiconductors are extremely attractive and suitable for high power and high temperature electronics applications. Among the various materials and device technologies, AlGaN/GaN HEMT seems the most promising. AlGaN/GaN HEMTs are similar to normally-on MOSFETs but doesn’t need substrate doping. And unlike AlGaAs/GaAs HEMTs, which requires intentional doping to form charge, 2DEG in AlGaN/GaN HEMT are induced by both spontaneous and piezoelectric polarization, thus no intentional doping is required. Moreover, the wide band gap offers a reliable technology of high voltage and high temperature operation, which are extremely promising for industrial, automotive and aircraft applications such as power converters and high voltage rectifiers.

In this chapter, detailed fabrication and characterization of AlGaN/GaN HEMT will be discussed. Firstly, the device fabrication using RoundHEMT will be disscussed. Figure 4.1.1 shows the flow chart of the overall fabrication process of AlGaN/GaN HEMTs. Secondly, we will discuss the device testing and characterization. Specifically, high temperature (up to 300°C) operation of AlGaN/GaN HEMTs was conducted. Finally, we propose a simple and novel spectroscopic photo I-V method of diagnosing the homogeneity of electrically-active defect distribution in the large area AlGaN/GaN HEMT epi structure grown on 6" silicon wafers, which will be discussed in the end.

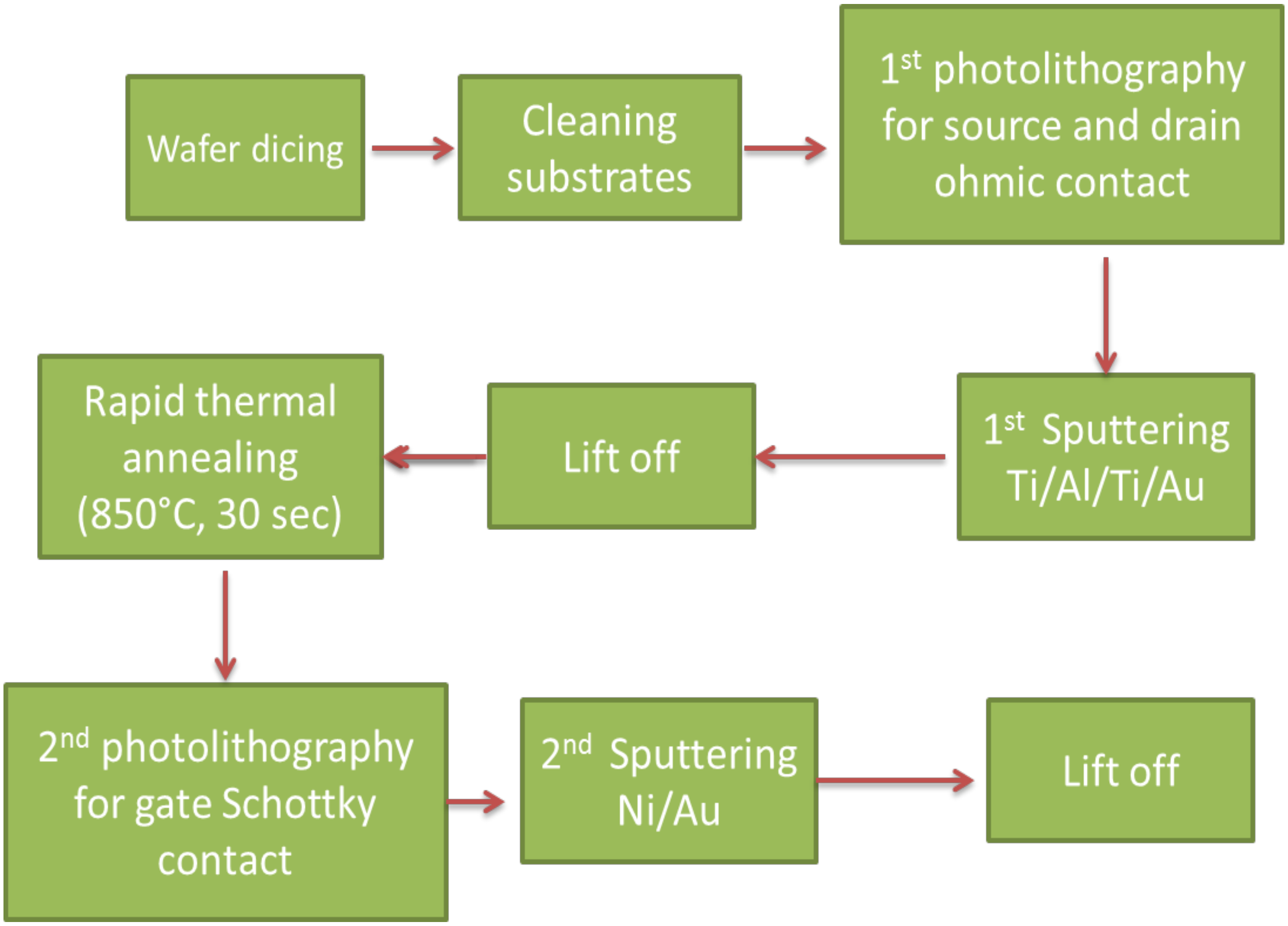

Figure 4.1.1 Flow chart of the overall fabrication process of AlGaN/GaN HEMTs.

4.2 Device Fabrication Process

4.2.1 Wafer Dicing and Raman analysis

The layers of HEMT structure were grown on 6” p-type Si wafer via metal-organic chemical vapor deposition (MOCVD). Initially, AlN nucleation layer was deposited, followed by growth of muli-layered AlGaN stress-controlling buffer layer with varying Al to Ga ratio. Then, undoped GaN channel layer (1 µm) and AlGaN barrier (20 nm) layers were grown sequentially on top of the stress-controlling layer. Finally, ultrathin GaN cap layer (2 nm) was deposited on the AlGaN barrier layer. Note that wafer XMK0909 and XMK1111 have 2 nm cap layers, but wafer XJH1611 does not have this cap layer. The highly doped GaN cap layer can reduce the contact resistance of ohmic contacts.[79,80]

In order to match the size of the photomask layout pattern, the 6” HEMT wafer was diced into individual pieces of dimensions of 1cm × 1cm. The wafer was cut from the Si side and each 1cm × 1cm piece was named according to Figure 4.2.1.1, where sample O1-O9 is near the major flat of the 6” HEMT wafer.

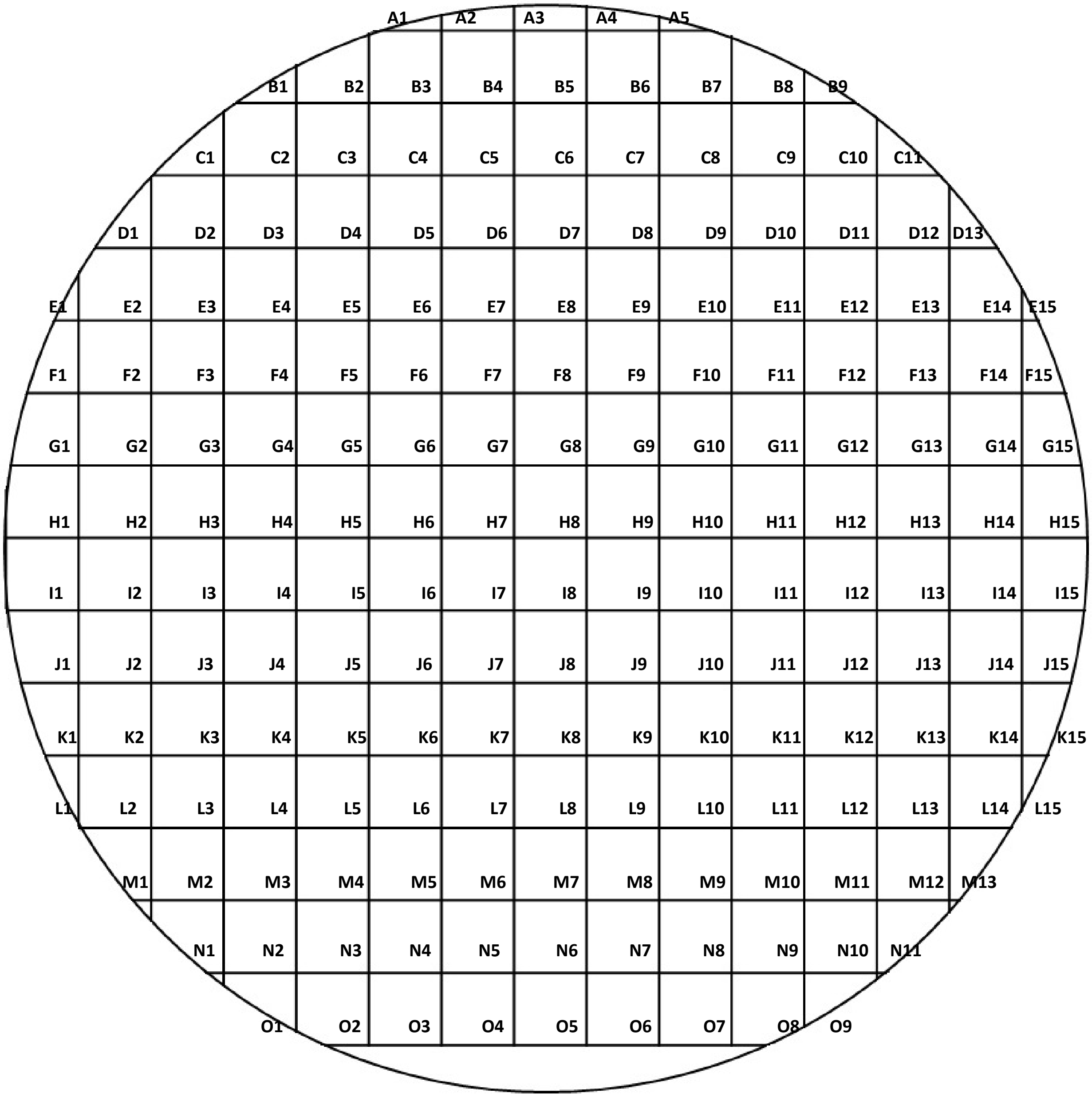

Figure 4.2.1.1 Names of each 1cm × 1cm dice of 6” HEMT wafer.

Raman Spectroscopy Analysis of the HEMT Wafer Before and After Being Diced

Raman spectroscopy is a non-destructive and non-contact technique to analyze materials. The dicing of the AlGaN/GaN HEMT epi structures on Si substrate may have effect of the strain modification of the wafer. To study the influence of stress on structural properties of the AlGaN/GaN HEMT wafer, raman spectrascopy was conducted. Strain relaxations occurred at all the heterointerfaces except for the AlGaN/(AlN/)GaN two-dimensional electron gas interface, which is desired for achieving high performance HEMT.[81] The shift of the $E_2^{(2)}$ mode is due to biaxial strain in the c-plane of the hexagonal GaN layer.[82]

Micro-Raman spectroscopy were conducted at room-temperature on the HEMT samples from wafer XMK0909 and XMK1111 using a 442 nm line (80 mW) from He-Cd laser (Kimmon Electric) as an excitation. In order to have high accuracy, 3600 gratings in the Raman system was used which has a resolution of 0.2 cm^{-1}. Figure 4.2.1.2 shows the Typical Raman spectrum of AlGaN/GaN HEMT structure on Si wafer (sample M1111 H15). In this graph, we can see two peaks: $E_2^{(2)}$ peak of Si at 519.8 cm^{-1} and $E_2^{(2)}$ peak of GaN ~568 cm^{-1}. From the shift of the dominant $E_2^{(2)}$ peak of GaN, tensile or compressive stress can be determined. However, for GaN-on-Si wafer, both the $E_2^{(2)}$ peaks from GaN and Si may shift, then it is necessary to look at the change of the distance between these two peaks. The unstrained GaN $E_2^{(2)}$ phonon frequency is claimed to be 567.2 cm^{-1}.[83]

$E_2^{(2)}$ phonon frequency is a function of the biaxial stress. Biaxial stress can be derived from the following equation (4.2.1)[84]:

$$\omega\,(E_2^{(2)}) = 567.2 - 4.2\,\sigma_b \qquad (4.2.1)$$

Where ω ($E_2^{(2)}$) is the $E_2^{(2)}$ peak measured in the experiment, σ_b is the Raman biaxial stress pressure and 4.2 cm^{-1} is the Raman biaxial pressure coefficient.[85] According to equation (4.2.1), the Raman biaxial stress pressure of the wafer XMK0909 and XMK1111 before and after dicing are plotted in Figure 4.2.1.3. According to naming diagram, A3 to O5 is vertical direction and H1 to H15 is horizontal direction. From the results of Figure 4.2.1.3, the dicing process does not change the strains in the wafer.

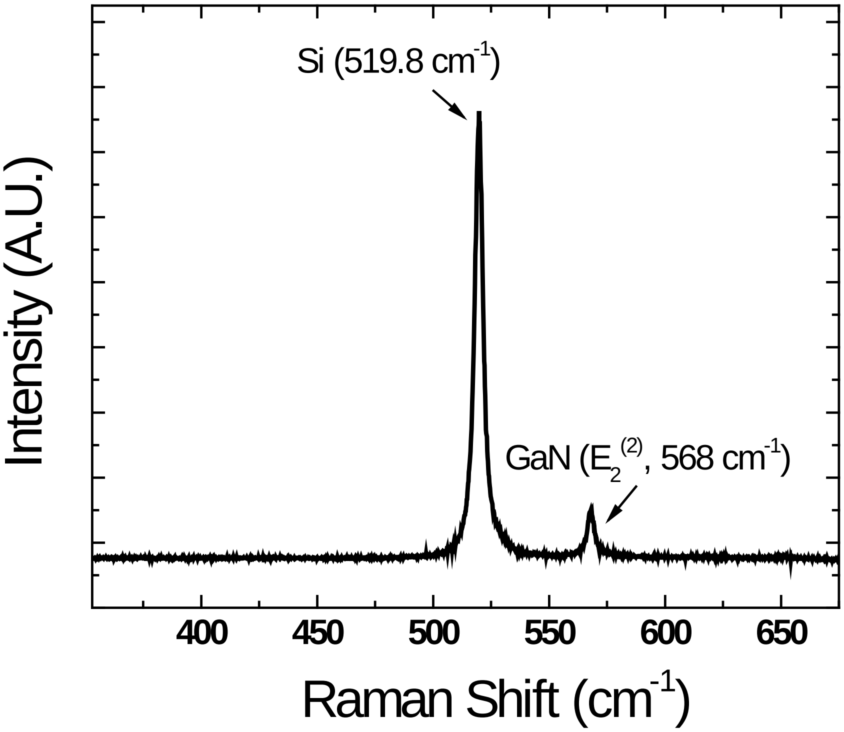

Figure 4.2.1.2 Typical Raman spectrum of AlGaN/GaN HEMT structure on Si wafer (sample M1111 H15).

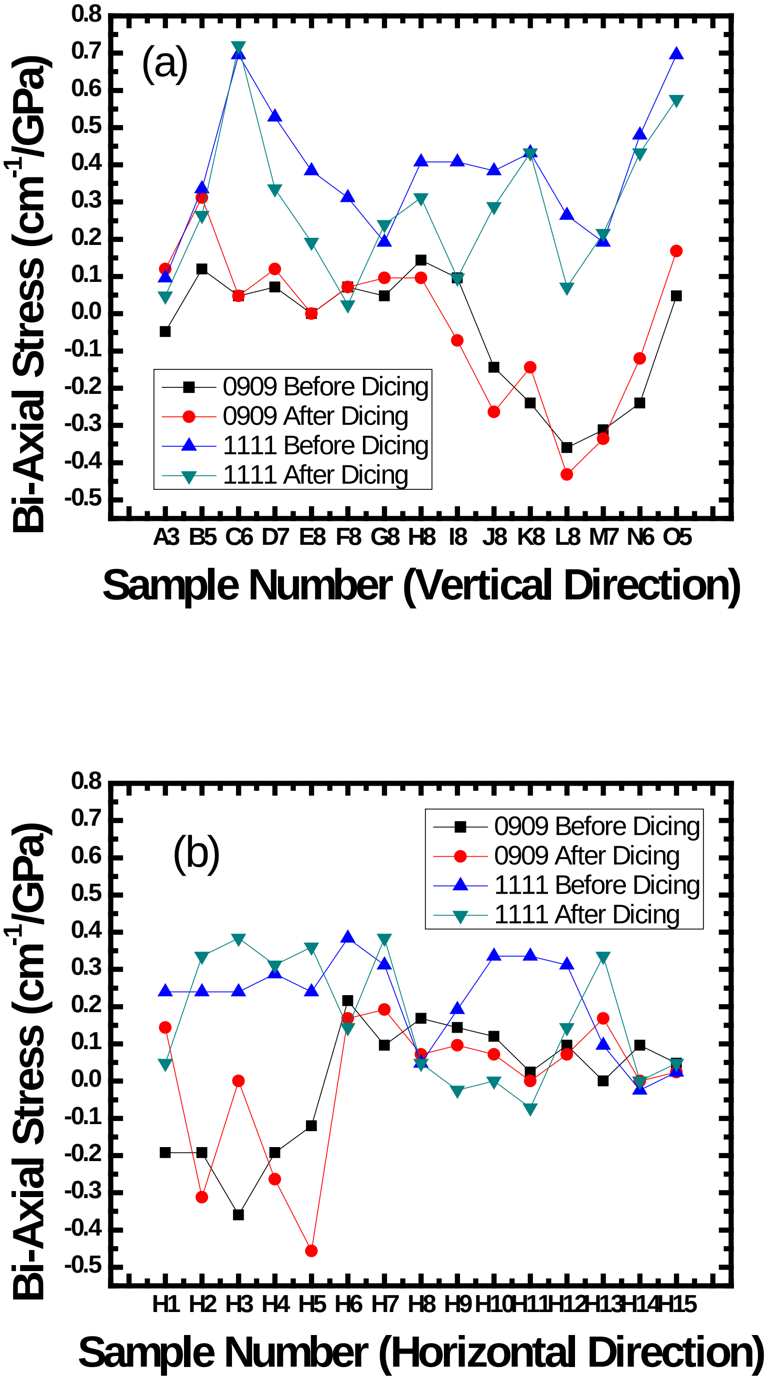

Figure 4.2.1.3 Bi-axial stress of a) vertical direction and b) horizontal direction of the samples before and after dicing.

4.2.2 Sample Cleaning

The sample cleaning was done in the Polypropylene Fume Exhaust Hood (PFH6C, LM Air Technology, Inc.) which is shown in Figure 4.2.2.1 in the clean room. Figure 4.2.2.2 shows the ultrasonic bath used in the cleaning procedure. To remove the organic, metal contaminants, native oxide and surface particulates, the AlGaN/GaN wafers were first cleaned using standard organic clean process which is listed as follows:

1. Place samples in acetone (electronic grade) for 5 minutes in the ultrasonic
2. Place samples in trichlorethylene (electronic grade) for 5 minutes in the ultrasonic
3. Place samples in acetone (electronic grade) for 5 minutes in the ultrasonic
4. Place samples in methonal (electronic grade) for 5 minutes in the ultrasonic
5. Repeat: Place samples again in another fresh methonal (electronic grade) for 5 minutes in the ultrasonic
6. Place samples in deionized water (di-H_2O) for 5 minutes in the ultrasonic

The first acetone and TCE is for complete organic degreasing, and the second acetone is to remove the TCE residue. The first methnal is for dissolving the acetone residue. The second methnal is for complete removal of organic solvents. Finally, di-H_2O is to rainse the sample and get the sample ready for native oxide and ionic contaminants removal: the samples are then immersed in a heated (about 100 °C) dilute HCl solution (HCl: di-H_2O=1:1) for 10 minutes. Smith *et al.* [86] HCl: di-H_2O (1:1) reported that result in the lowest levels of carbon (C) and Oxygen (O). Diale *et al.* [87] reported that the effects of Cl on the GaN surface may enhance the adhesion of metals, thus improving device quality. Lastly, the sample is rinsed again in di-H_2O and blow dried in Nitrogen.

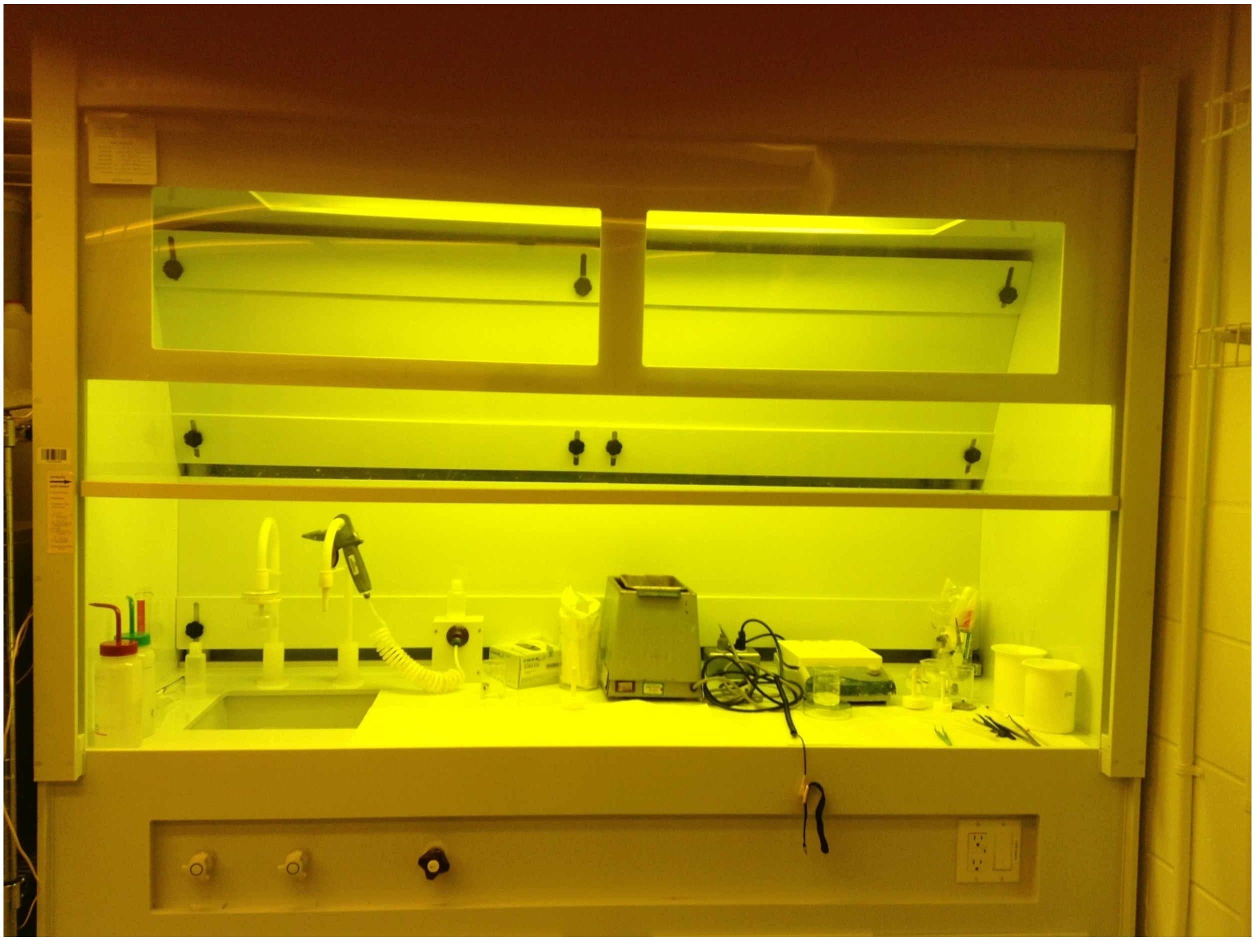

Figure 4.2.2.1 Polypropylene Fume Exhaust Hood.

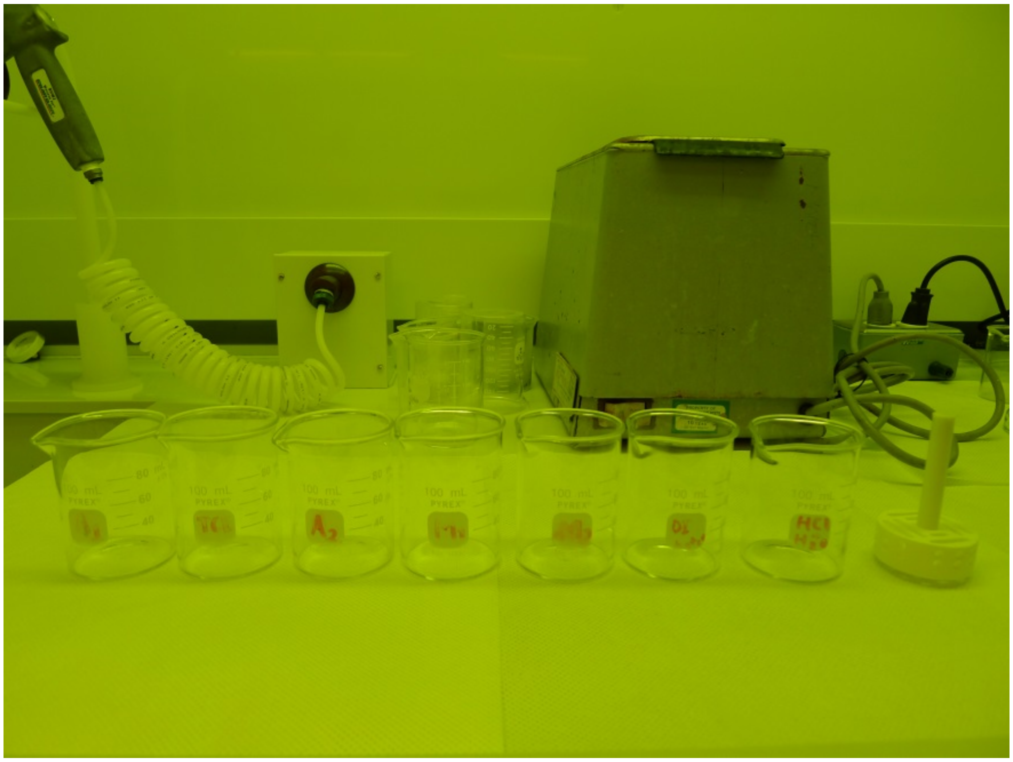

Figure 4.2.2.2 Ultasonic bath and beakers.

4.2.3 Photolithography

Photolithography is the process that transfer geometric shapes on a photomask to the surface of the wafer. The steps involved in the photolithographic process are photoresist application, soft baking, mask alignment, exposure, development and hard-baking. As shown in Figure 4.2.3.1, Karl Suss MJB3 UV400 mask aligner, which has a mercury (Hg) arc lamp of 160W output power and an optical microscope of magnifications of 5, 10 and 20, was used for this study. The photo-mask aligner is manually controlled and the spatial resolution is about 3µm. As shown in Figure 4.2.3.2 and Figure 4.2.3.3, There are generally two polarites of photo-masks: dark field (positive) mask and clear field (negative) mask. For dark field mask, most of the area of the exposure field is dark. And clear field mask has opaque images and clear background. Square clear field mask which has round HEMT patterns and served as first and second photo mask, respectively, for the reverse photolithography is used in the experiment. And since clear field mask is used, reversing photolithography process is conducted.

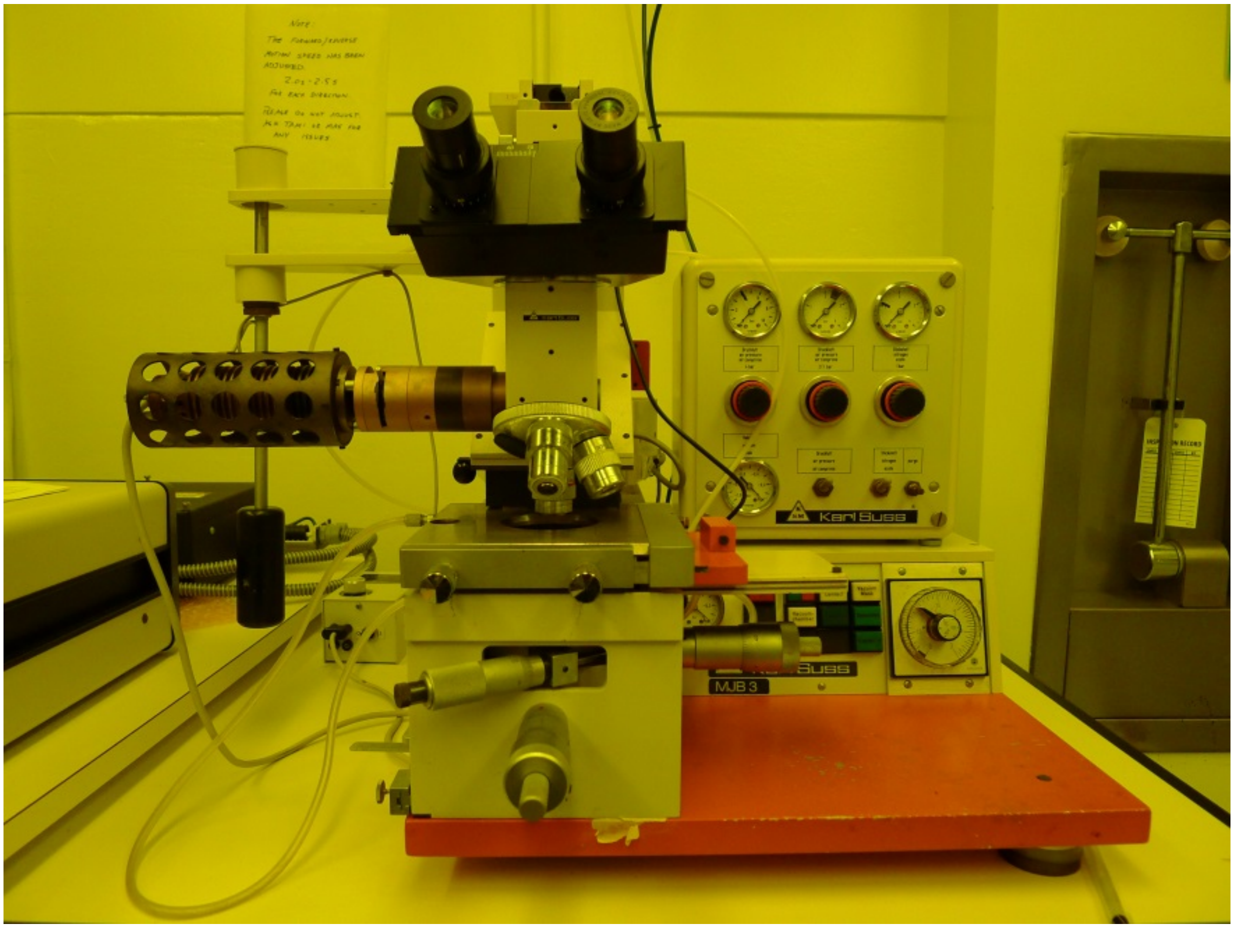

Figure 4.2.3.1 Karl Suss MJB3 photo-mask aligner.

The image reversal photoresist, Shipley AZ5214E, is used for mounting the wafer and spin-coating the wafer. The 1cm × 1cm sample was attached to a 3" silicon wafer using photoresist.

The spin-coating was done at a rotor speed of 4000 rpm for 30 sec. And then the sample was soft baked in an oven at 110 °C (Figure 4.2.3.4) for 1 min to dry off the solvents, promote the adhesion of the photoresist and be more photosensitive. The sensitivity of the photoresist can be destroyed by under-baking or over-baking.

In the next step of the photolighography process, the sample on the 3" Si wafer was held on the mask alighner, and by using X, Y, and θ adjustment, the sample was brought into alignment with the photo-mask feature. And the sample had UV contact exposure for 30 sec at the lamp power of 150 W.

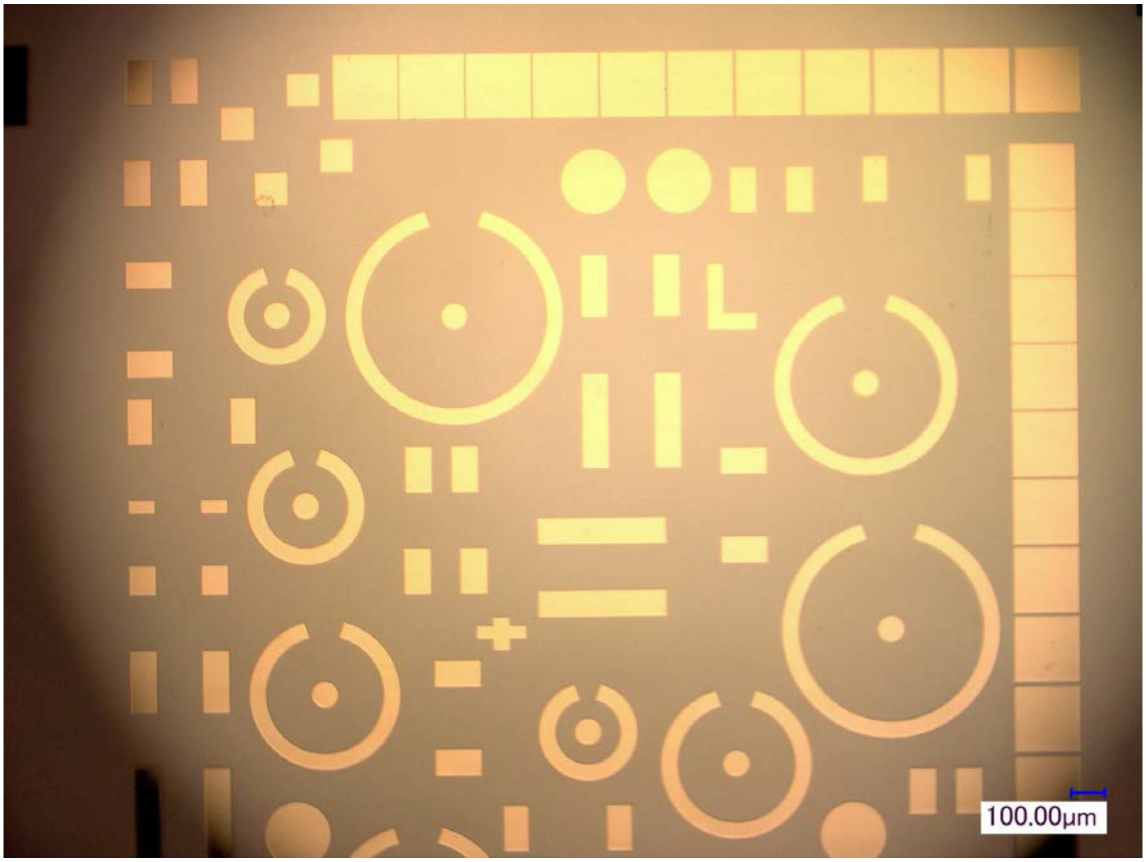

Figure 4.2.3.2 Photograph of the source and drain pattern photomask.

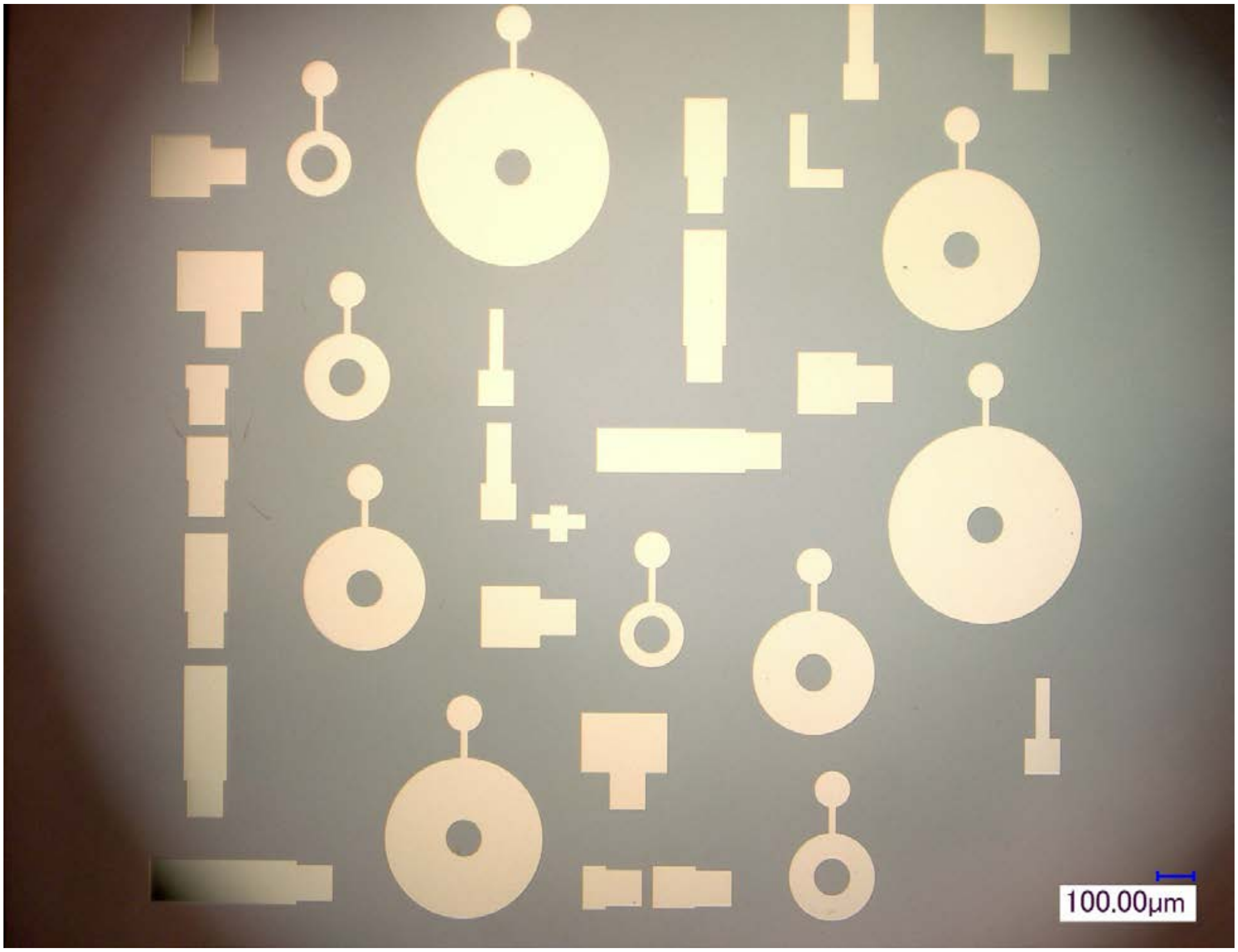

Figure 4.2.3.3 Photomask of gate pattern.

After exposure, for the reversing photolithography to take place, the sample is hard baked at 110 °C for 1 min. This step makes the photoresist of the unexposed area remains photoactive and the exposed area insoluble in the developer (4 parts of AZ 400K and 1 part of DI water). The sample then had flood expousre for 1 minute which maskes the previously unexposed area of the photoresist soluble in the developer. The sample was immersed in this dilute developer for 20 to 40 seconds. Complete development was confirmed using optical microscope. The above photolithography process result in the negative image of the mask.

Figure 4.2.3.4 Oven.

4.2.4 DC Magnetron Sputtering

Sputtering is a physical vapor deposition (PVD) process that ion collisions dislodge particles from the target material which deposit on the surface. DC Magnetron Sputtering is a popular and highly developed technique which allows for the sputtering of a large variety of conducting materials with a high control over film uniformity and thickness.

The DC magnetron sputtering system used in this study is a homemade high vacuum system (Figure 3.3.1) that consists of a cylindrical vacuum chamber connected to a roughing and a diffusion pump. It has four 2" diameter Polaris magnetron sputtering guns which is equipped with chimneys to prevent the cross contamination between targets. The ring magnet confines the ions close to the surface of the target to increase the sputtering rate. Chilled water lines are stored underneath the guns for cooling during the sputter. All metals in this study were DC magnetron sputtered in an Ar plasma. The samples were located on the top rotational plate, at a distance of 4" from the target. Prior to sputtering, a base vacuum pressure of 3×10^{-7} Torr was achieved. Then, Ar was introduced into the chamber at a flow rate of 100 sccm (standard cubic centimeters per minute) and a pressure of 18 mTorr. When the pressure of Ar reaches 18 mTorr, DC voltage is applied between the target (cathode) and the substrate (anode) to generate the gaseous Ar plasma. During the sputtering, the temperature of the substrate was maintained at room temperature. Before the sputtering, pre-sputtering is conducted to remove the trapped impurities from the surface of the target. Depending on the metal, pre-sputtering can take from 30 sec to 5 min. After pre-sputtering, the sample is moved to the location right above the sputtering target to be sputtered for as long as required to yield a desired film thickness. The sputtering rate of the target is checked using Tencor profilometer (Figure 4.2.4) which measures film thickness.

After the first reverse photolithography, the samples are loaded in the sputter system for depositing source and drain (ohmic contact) metals. The typical sputter conditions of this process are summarized in Table 4.2.4.1. Ohmic contact formation to GaN is a crucial processing step for the fabrication of GaN HEMT devices. Stability of the ohmic contact affects the reliability of the GaN devices. Ti/Al/Ti/Au has been widely used in the ohmic contact schemes for n-type GaN. [88,89,90,91,92,93] So it typically has a Ti/Al/ blocking layer/Au multilayer structure. The blocking layer is often one of the metals Ti, Ni, Mo, or Pt.

When Ti reacts with GaN, it follows the formation of vacancies of nitrogen in the GaN below the contact layer, thus the contact region is doped and ohmic contact is formed due to the low work function of TiN. High concentration of nitrogen vacancies are created in the GaN near the Ti/GaN interface, due to the formation of TiN layer when Ti reacts with GaN, causing the GaN to be heavily doped n-type. In order to achieve good ohmic behavior, a tunneling metal/semiconductor contact is formed. Therefore, the tunneling process will become dominant and the specific contact resistivity reduces.

To prevent the oxidation of TiN, Au is sputtered to serve as a stable cap. Au is deposited as the final metal layer to exclude oxidation of the contact and the metal should limit the diffusion of Au into the layers below and vice versa. Ti/Al thickness ratio is important. Al can reduce Ga_2O_3 on GaN upon annealing at elevated temperatures and would be expected to do the same to Ti metal because Ti has a strong tendency to react with oxide. The necessity of Al on top of Ti is mainly evidenced by the fact that an optimum Ti/Al relative thickness exists, both on GaN and on AlGaN/GaN.

Sputter target	**Voltage (V)**	**Current (A)**	**Pre-sputter time (min)**	**Sputter duration (min)**	**Thickness of film (nm)**
Ti	290	0.25	3	10	50
Al	290	0.2	2	20	150
Ti	290	0.25	2	10	50
Au	340	0.1	1	5	100

Table 4.2.4.1 Sputter conditions for ohmic contact metals.

To achieve high breakdown voltages and low gate leakage current, a Schottky gate contact with a large barrier height is always desirable for AlGaN/GaN HEMT. Table 4.2.4.2 summarizes the sputtering conditions for depositing gate contact metals. Ni is chosen since it has greater work function than GaN. Since we use DC magnetron sputtering, we cannot use magnetic target like Ni, we need use nonmagnetic sputtering target NiV_7. Element V was added to make Ni target nonmagnetic.

Sputter target	**Voltage (V)**	**Current (A)**	**Pre-sputter time (min)**	**Sputter duration (min)**	**Thickness of film (nm)**
NiV_7	450	0.25	2	5	50
Au	340	0.1	1	5	100

Table 4.2.4.2 Sputter conditions for gate contact metals.

Figure 4.2.4 Tencor profilometer.

4.2.5 Lift-off

Lift-off is a method for patterning films that are deposited. During sputtering process, metal film is deposited all over the substrate. The metal film deposited on top of the photoresist is lift-off by acetone, and metal film sticks only where photoresist is cleared. The result of the lift-off process is checked with the high resolution optical microscope (Figure 4.2.5.1).

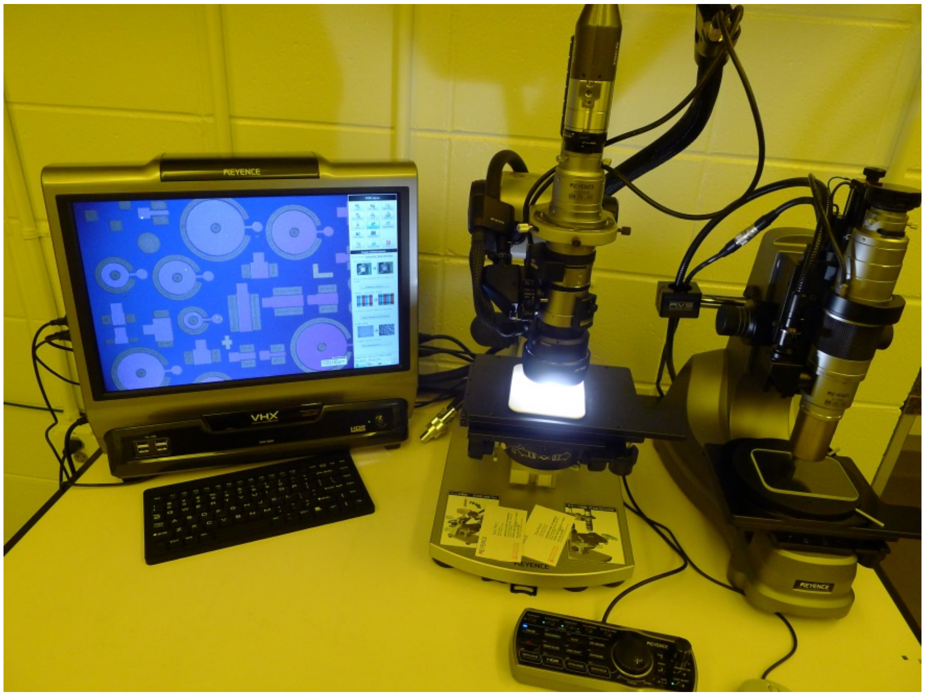

Figure 4.2.5.1 High resolution optical microscope. (Photo credit: Chungman Yang)

The photoresist should avoid being overheated during the sputtering process, or it may result in difficulties in the lift-off process. Exposure duration, baking temperature, and resist developer parameters also affects the quality of the lift-off process. Thicker metal film is more impermeable to the solvent acetone and results in longer time in lift-off. Figure 4.2.5.2 shows the result of the first lift-off, that is, after the ohmic contact metal sputtering; and Figure 4.2.5.3 shows the result of the second lift-off, after the gate metal contact sputtering. And each of the 10 round devices is named according to Figure 4.2.5.3. Table 4.2.5 summarizes the dimensions including gate width and length, source to gate distance, and gate to drain distance of each device.

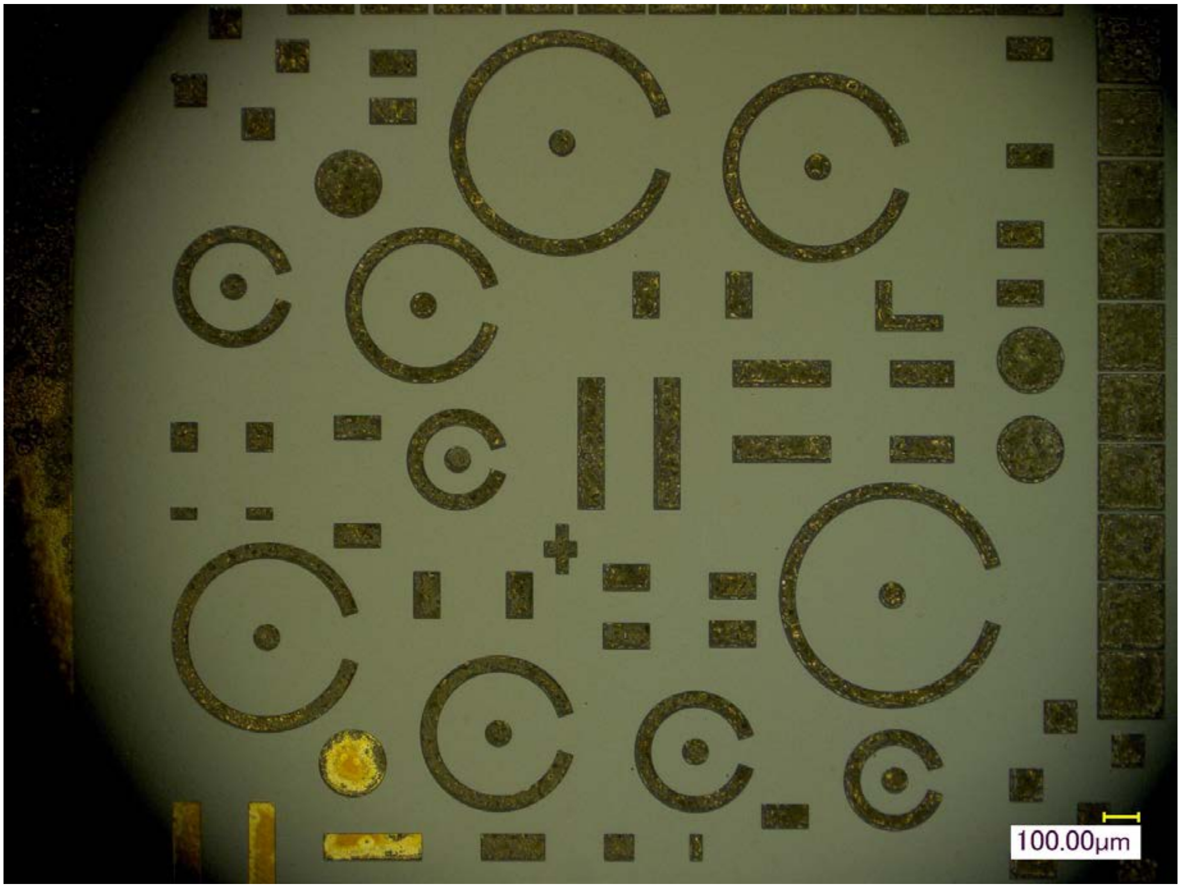

Figure 4.2.5.2 Photograph of the source and drain of the AlGaN/GaN HEMT device.

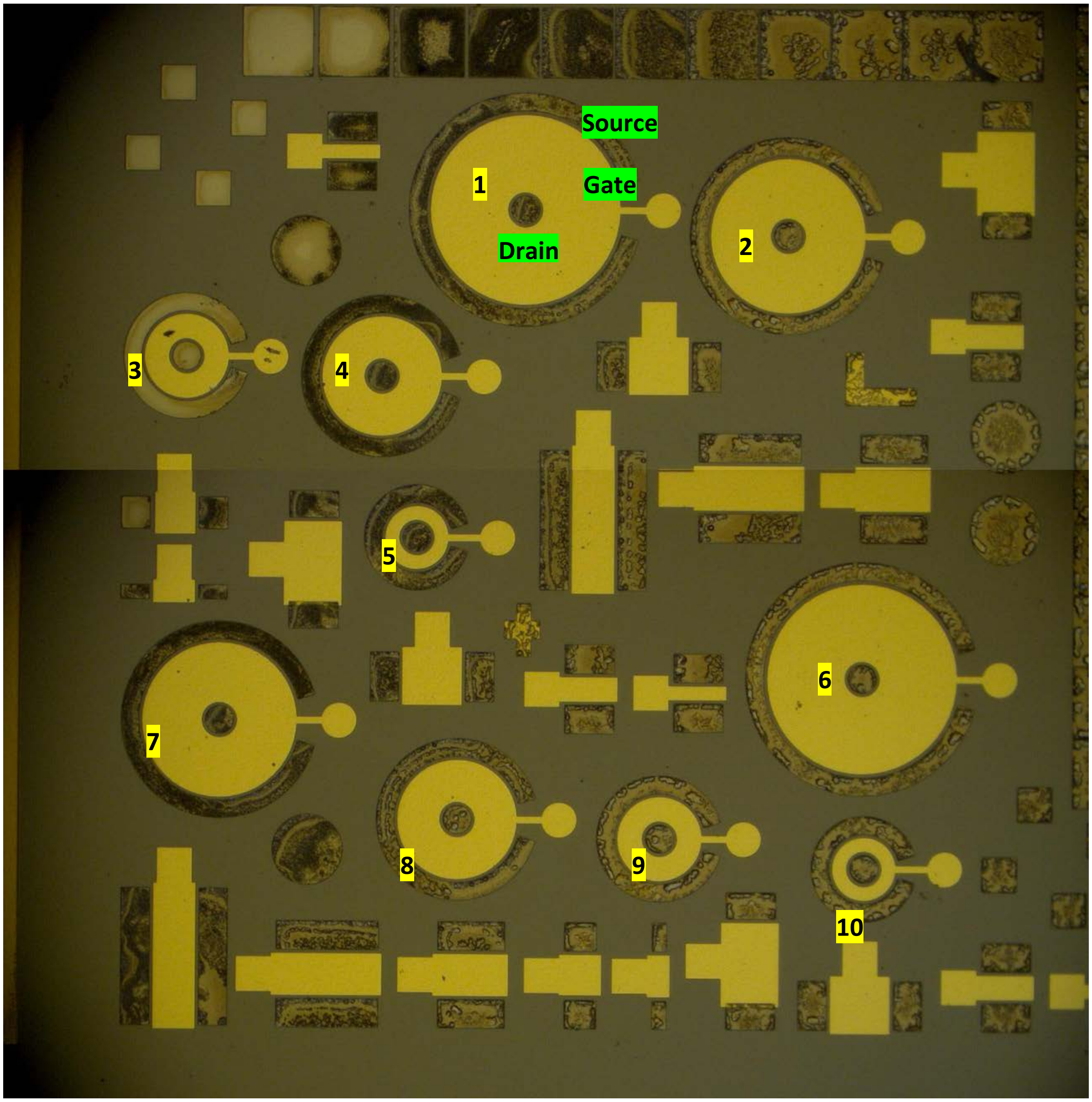

Figure 4.2.5.3 Names of each AlGaN/GaN HEMT device (1-10).

Device #	**L_{gd} (gate to drain) (μm)**	**L_{sg} (source to gate) (μm)**	**L_g (gate length) (μm)**	**W_g (gate width) (μm)**
1 and 6	10	10	220	1000
2 and 7	10	10	170	850
3 and 8	10	10	120	690
4 and 9	10	10	70	530
5 and 10	10	10	40	440

Table 4.2.5 Demensions of each AlGaN/GaN HEMT device (1-10).

4.2.6 Rapid Thermal Annealing

Rapid thermal annealing (RTA) is a semiconductor fabrication process of heating a single wafer at a time in order to affect its electrical properties. The RTA system is used for forming low resistance ohmic contact in this research. It consists of a cylindrical vacuum chamber and two vacuum pump system which is similar to the sputtering system that described in sec 4.4, and able to achieve a vacuum pressure of $1\sim4\times10^{-7}$ Torr. The heating elements in the system include two carbon strips, a variable transformer controlling the current through the carbon strip, and an Omegascope OS1100 infrared pyrometer on top of the chamber which is calibrated with the black body emission and focused in the edge of the sample to monitor the temperature.

Figure 4.2.6 shows a photograph of the rapid thermal annealing system used for this research. As mentioned in the previous section, rapid thermal annealing is performed to let Ti react with GaN to form TiN which generates nitrogen vacancies to make the surface heavily n-type and form tunneling junction. Ohmic contact annealing is a crucial step in improving the electrical properties of the samples. After loading the sample, the annealing chamber is pumped to a pressure of 4×10^{-7} Torr to remove moisture and possible contaminants. The system is then flushed with research grade (99.9997%) nitrogen for 10 minutes. And then by controlling the variable transformer, the temperature is ramped up to 850 °C with 10 seconds. The 1cm × 1cm sample was annealed in a nitrogen atmosphere at 850 °C for 30 sec. Afterwards, the temperature was brought down back to room temperature in about 10 min.

Ti/Al metal system is frequently used to fabricate low resistivity contacts to n-type GaN. It is believed that during annealing, which is required to form the ohmic contact, nitrogen extracted from GaN reacts with Ti to form TiN. The out diffusing nitrogen atoms create nitrogen vacancies, which acting as shallow donors, heavily dope the sub contact region of n-GaN.

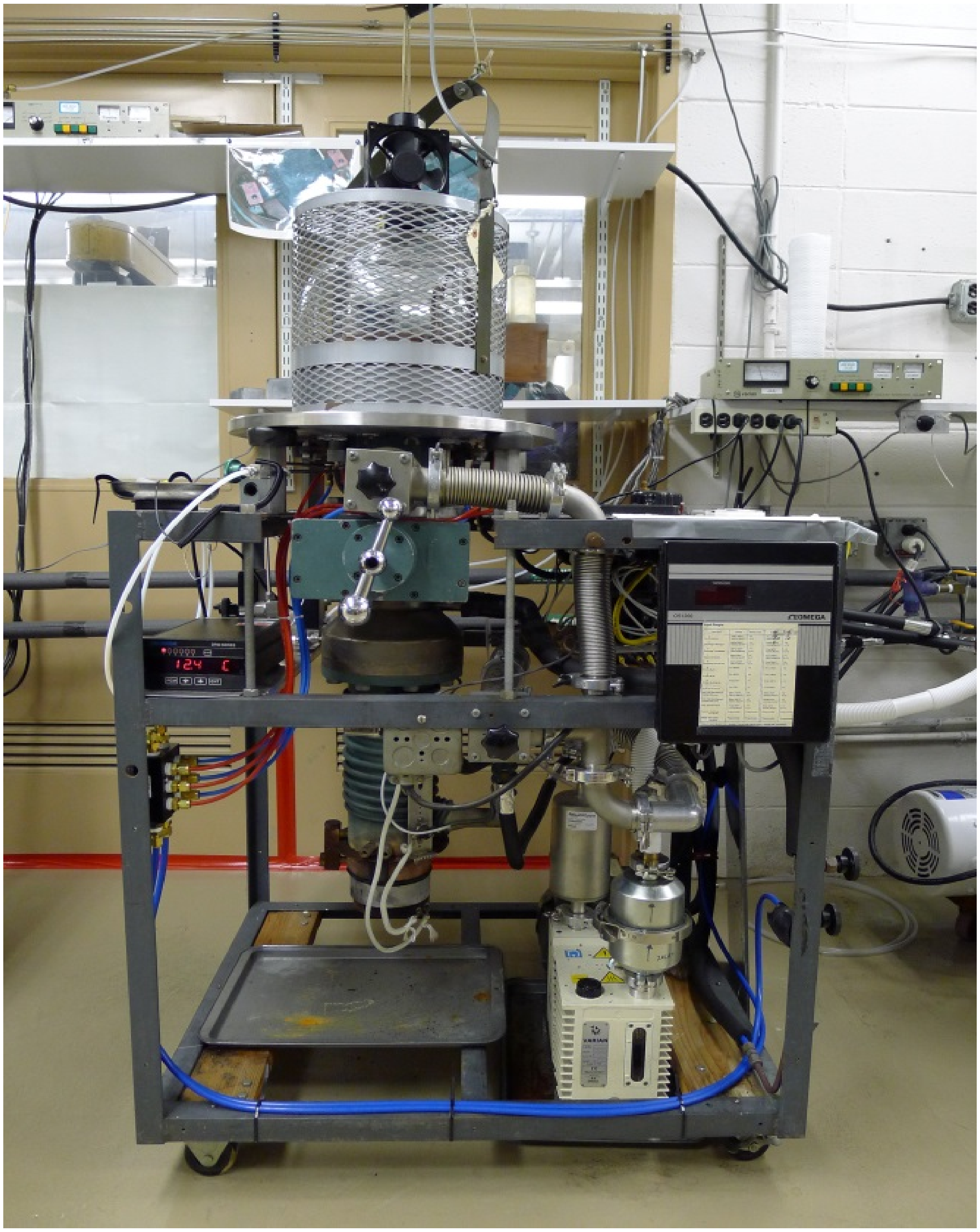

Figure 4.2.6 Rapid thermal annealing system.

4.3 Device Testing and Characterization

Current-Voltage (*I*-*V*) measurement is an important technique to characterize the performance of the AlGaN/GaN HEMT and to extract parameters such as threshold voltage, transconductance, and specific on-resistance.

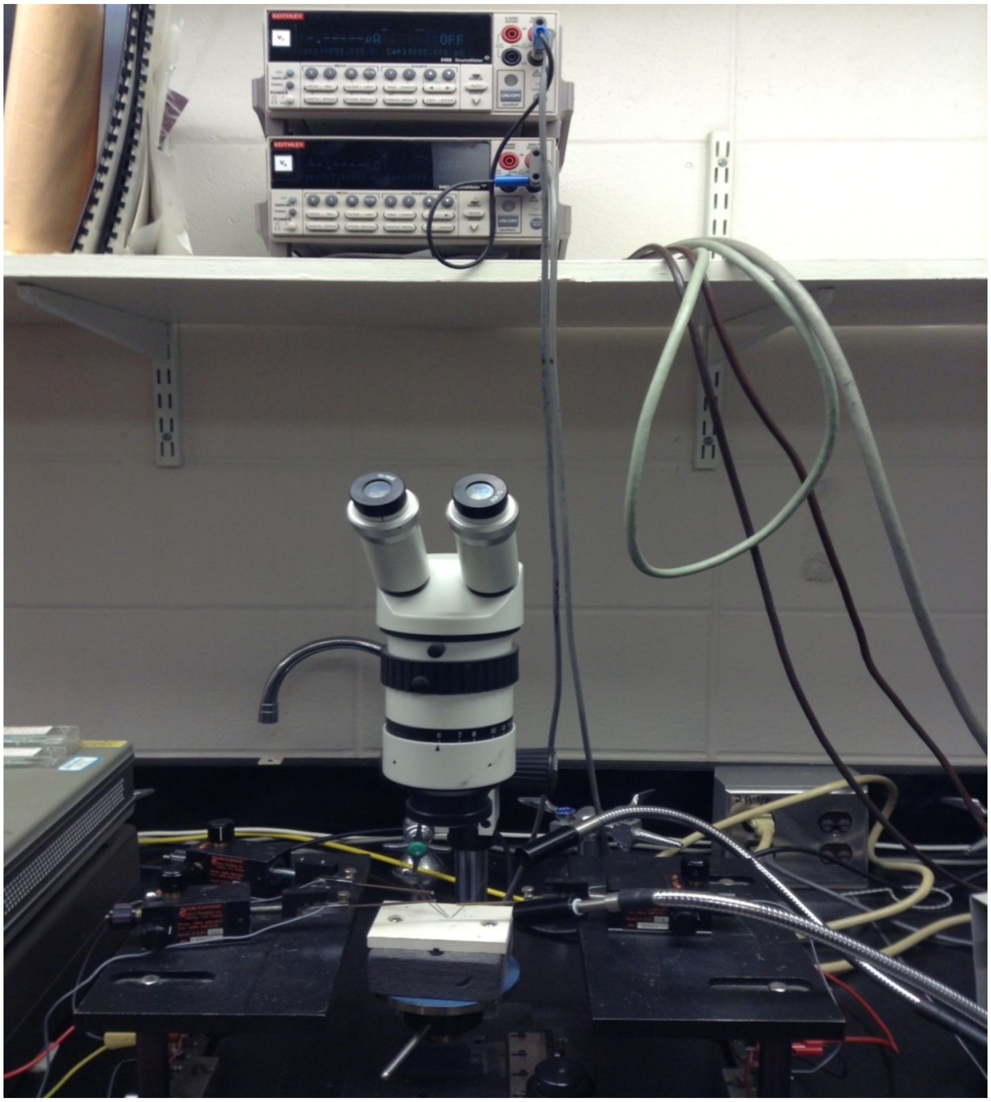

Figure 4.3.1 High field *I*-*V* measurement system.

The high field *I-V* measurement system shown in Figure 4.3.1 was used for the *I-V* measurement of the round AlGaN/GaN HEMT. The system includes a Keithley 2410 (source & drain) source meter, a Keithley 2400 (gate voltage & current), and a probe station. Both of the source meters are capable of applying voltage and measuring current at the same time. Keithley 2410 measures gate voltage V_g.

Some of the *I-V* measurements of the AlGaN/GaN HEMT devices were also conducted using Semiconductor characterization system (Keithley 4200 – SCS) (Figure 4.2.2) and Micromanipulator (Figure 4.3.3).

Figure 4.3.2 Semiconductor characterization system (Keighley 4200 – SCS).

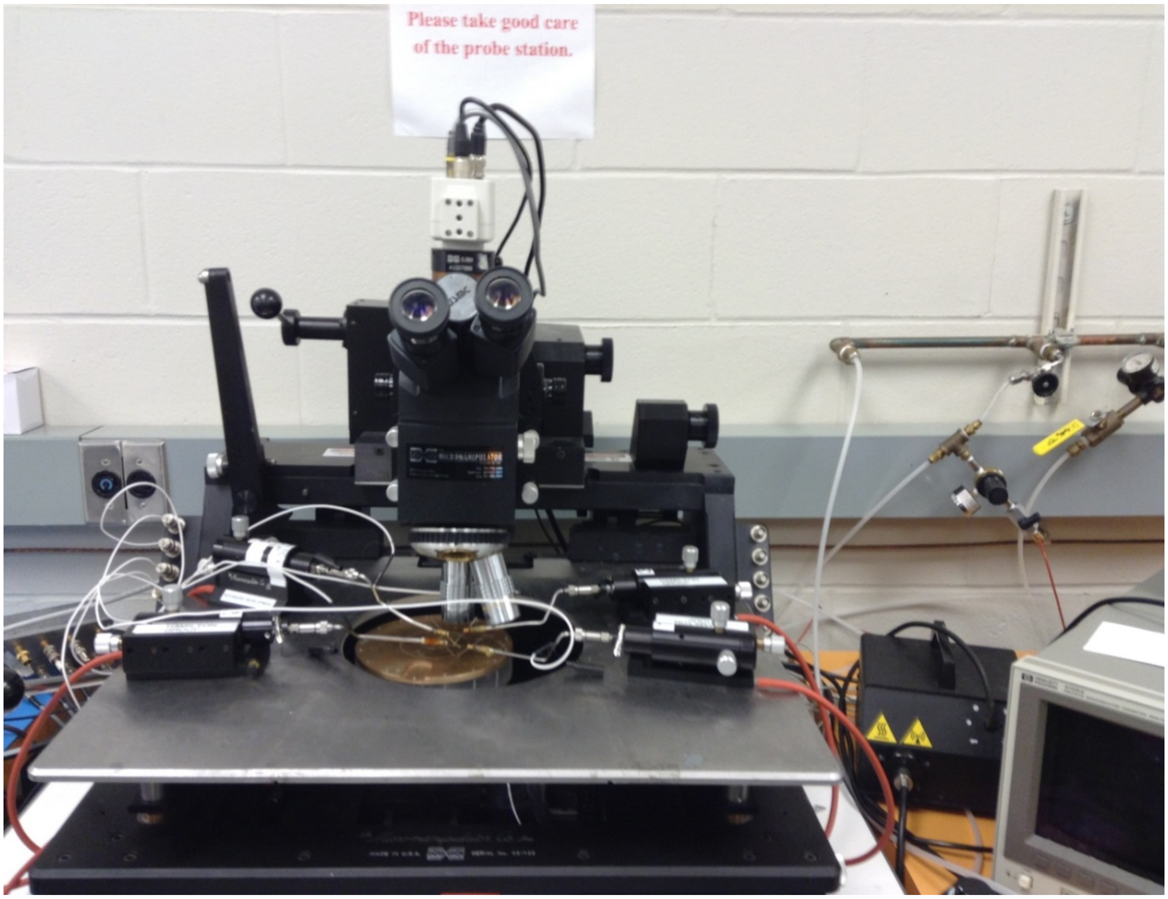

Figure 4.3.3 Micromanipulator.

Dices located from different area (e.g. top, center, and bottom) of the wafer, which and have different device dimensions, were fabricated into AlGaN/GaN HEMT and tested. Figure 4.3.4, Figure 4.3.5, Figure 4.3.6 and Figure 4.3.7 show the I_D-V_d , I_D-V_g, I_g-V_g and transconductance (g_m) characteristics of HEMT samples from different areas of the wafer XJH 1611. And Table 4.3.1 summerizes the electrical characteristics that derived from the above figures.

From the I_D-V_d charateristics, Specific On-Resistance R_{ON} was evaluated measuring the drain current change when the drain voltage V_d was increased form 0 V to 0.25 V at V_g = 0 V. And transconductance (g_m) can also be derived both from I_D-V_d charateristics or I_D-V_g characteristics since transconductance is a measure of the sensitivity of drain current to changes in gate-source bias, as shown in equation 4.3.1.

$$g_m = \frac{\Delta I_{out}}{\Delta V_{out}} \tag{4.3.1}$$

Threshold voltage, V_{th}, is the value of the gate bias needed to push away the channel electrons so that current flows from source to drain. V_{th} in this study is derived from I_D-V_g characteristics. And the derivative of I_D-V_g curve yields the transconductance (g_m) characteristics curve.

From the results of Table 4.3.1, we can see that center sample H8 A9 with gate width of 530 µm showed the largest transconductance of 14.08 mS/mm and smallest R_{ON} of 0.25 Ω-cm^2 among the 4 samples.

All the samples showed small threshold voltage about -1.2 V~ -1.6 V. It is of great importance to control the threshold voltages (V_{th}) of AlGaN/GaN high-electron mobility transistors (HEMTs) accurately. Low threshold voltage is desirable for high power switching and digital logic applications. In a conventional depletion-mode (D-mode) AlGaN/GaN HEMT, threshold voltage is usually very high, which makes it unsuitable for high power and digital logic applications. Joshi *et al.*[94] reported that by varying the Al composition and by employing different grading profiles, the threshold voltage can be tailored. They have shown that for conventional HEMT, the threshold voltage (V_{th}) is -8 V and V_{th} is -3.5 V for graded HEMT with Al composition ranging from 0 to 30%, and V_{th} decreases to -3 V by changing the Al composition from 0 t o30 and back to 0.

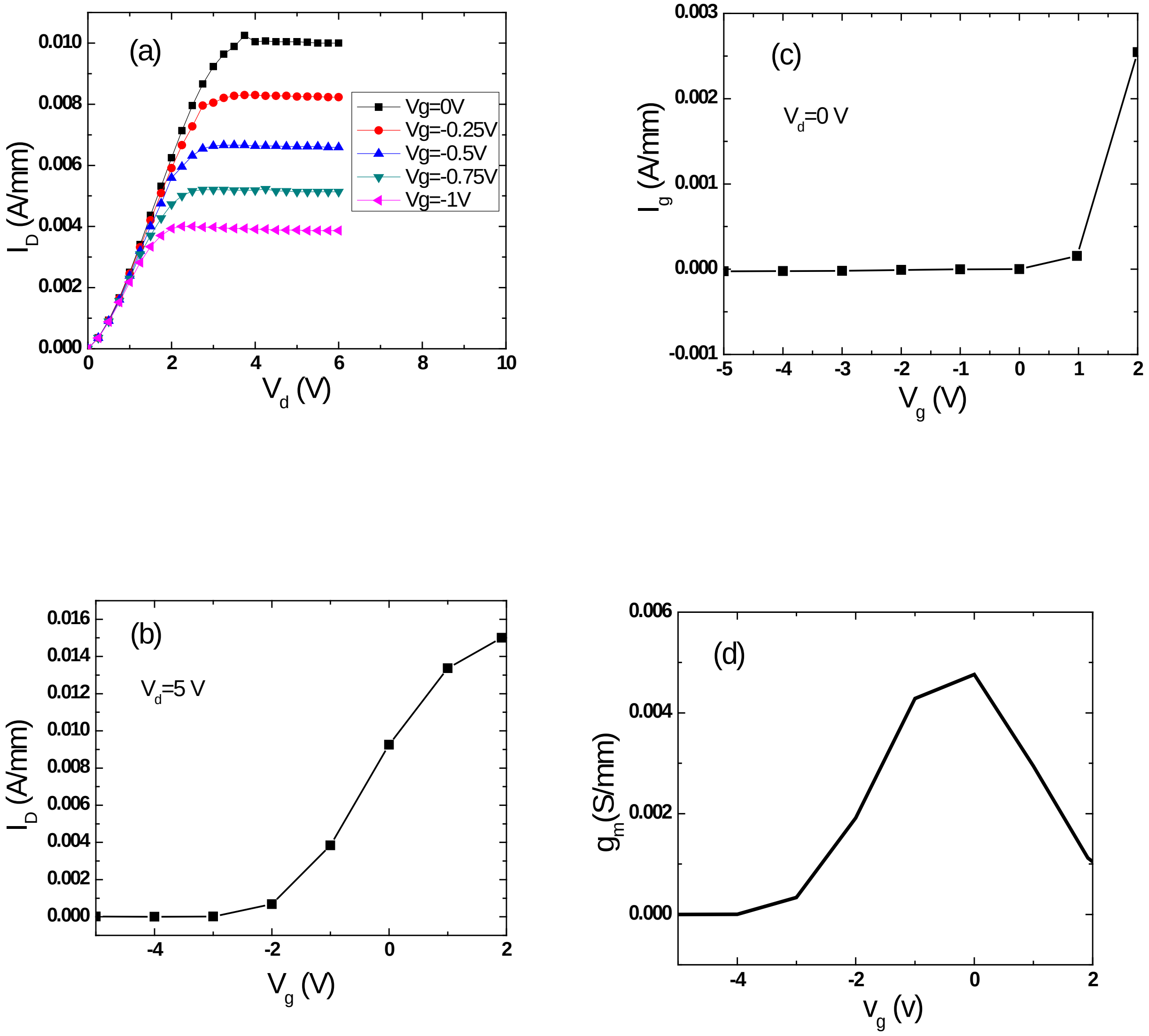

Figure 4.3.4 a) I_D-V_d , b)I_D-V_g, c)I_g-V_g and d) g_m characteristic of XJH1611 H9 C10.

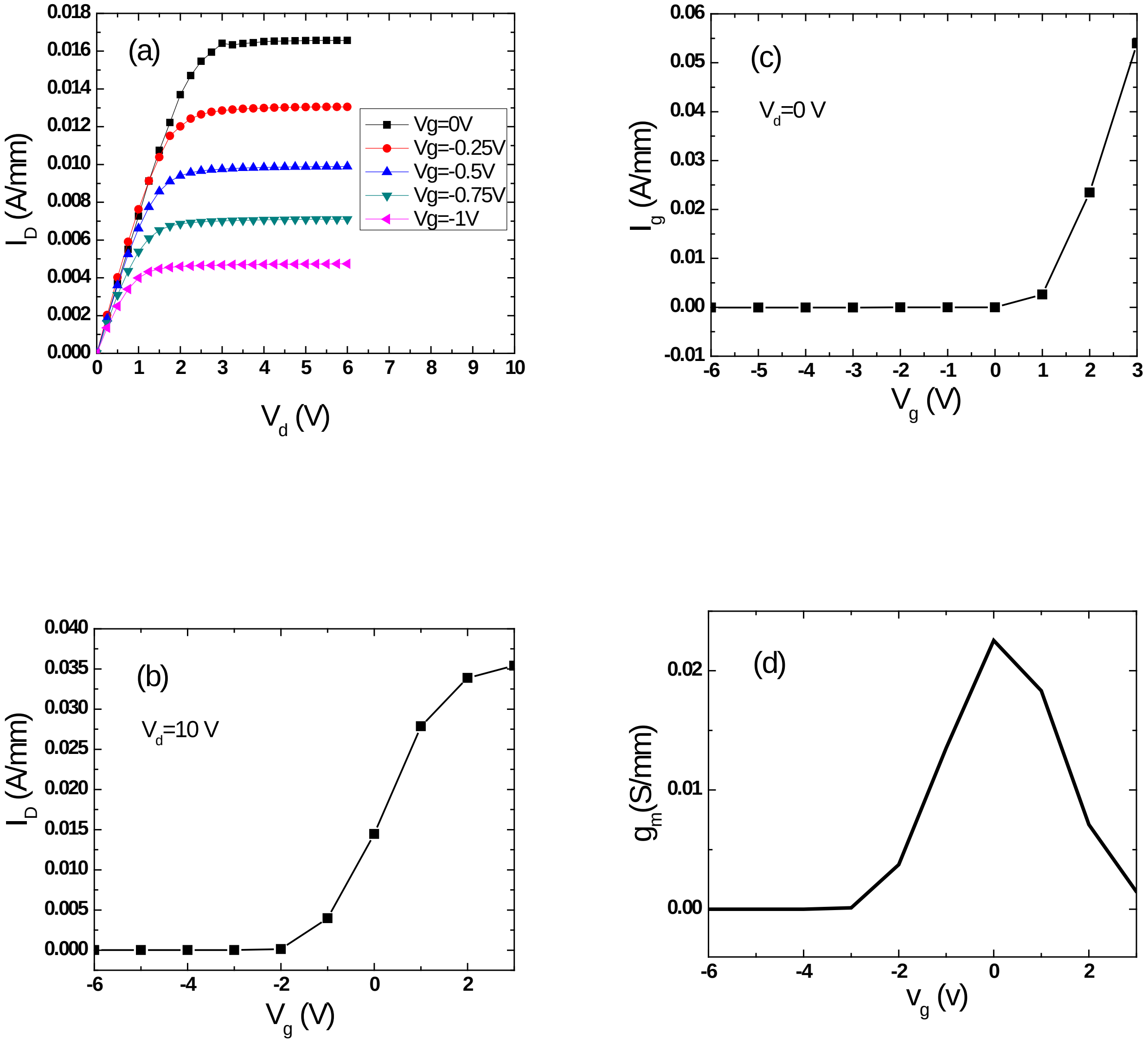

Figure 4.3.5 a) *Id-Vd* b) Id-Vg, c) Ig-Vg and d) g_m characteristic of XJH1611 H8 A9.

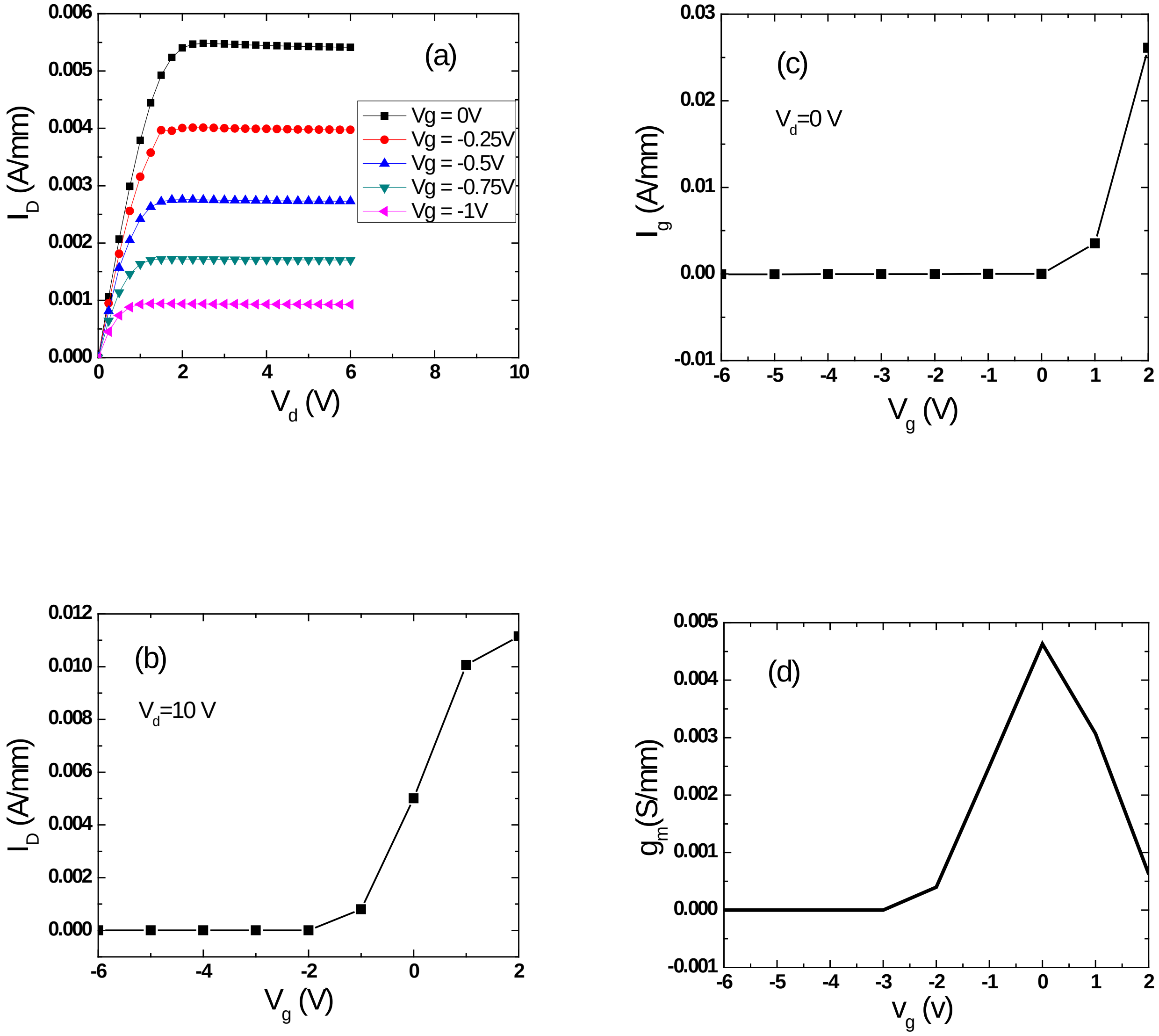

Figure 4.3.6 a) *Id-Vd* b) Id-Vg, c) Ig-Vg and d) g_m characteristic of XJH1611 N7 B2.

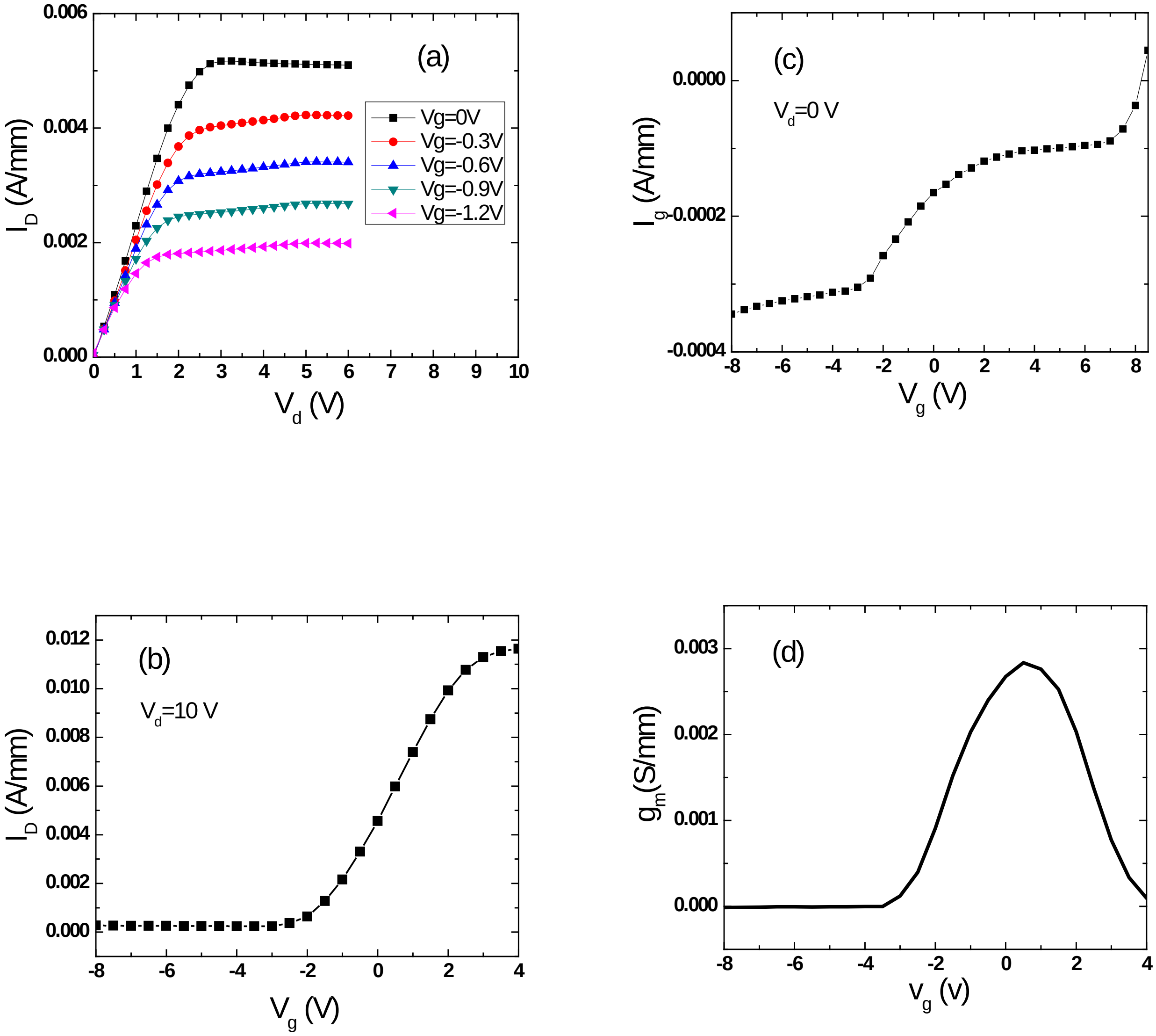

Figure 4.3.7 a) *Id-Vd* b) Id-Vg, c) Ig-Vg and d) g_m characteristic of XJH1611 C6 A3.

Wafer #	**XJH1611**	**XJH1611**	**XJH1611**	**XJH1611**
Sample Name	H9	H8	N7	C6
Quadrant of the Sample	C	A	B	A
Device #	10	9	2	3
Gate Width (µm)	440	530	850	690
Specific On Resistance (Ω-cm^2)	2.24	0.25	0.28	0.81
Threshold Voltage	-1.5	-1.3	-1.2	-1.6
Max. Transconductance (mS/mm)(determined by Id-Vd	2.4	14.08	5.8	2.96
Max. Transconductance (mS/mm)(determined by d(Vg)/d(Id))	4.52	11.95	4.63	2.84
Gate Leakage from IgVg @-10V (A/mm)	-8.17E-05	-7.37E-05	-5.55E-05	-4.54E-04
Drain Leakage from IdVg @-10V (A/mm)	5.92E-05	2.47E-05	1.40E-05	4.07E-04

Table 4.3.1 Electrical characteristics of the RoundHEMT.

4.4 High Temperature Operation of Round AlGaN/GaN HEMT

Due to the wide band gap of GaN (3.44 eV), at very high temperatures, the intrinsic carrier concentration of GaN remains low, GaN based HEMT structures has the promising potential of high temperature operation beyond that of Si and GaAs based devices. The applications of the high temperature operation of HEMT include automotive and aerospace engine control, and microwave devices. However, reliability and high temperature operation research is in its initial stages.

Adachi *et al.*[95] has investigated the high temperature operation of AlGaN/GaN HEMTs at channel temperature of 269 °C and 368 °C. Hatano *et al.* [96] have tested their GaN-channel HEMT from room temperature to 300 °C. Cai *et al.*[97] has investigated the performance of AlGaN/GaN HEMT direct-coupled PET logic (DCFL) at 375 °C. Maier *et al.* [98]have tested their AlGaN/GaN HEMTs devices at 300 °C and 400 °C for 250 h and seen the devices failed at 500 °C. However, only a few research groups have carried out the demonstration of high-temperature operation of the HEMT based digital circuits.

So far, there are only a few publications about the high temperature operation of the conventional AlGaN/GaN HEMT, but no publication about the high temperature operation of RoundHEMT. In this study, we have investigated that high temperature operation of round AlGaN/GaN HEMTs on Si substrate up to 300°C. The results show that the fabricated round AlGaN/GaN HEMT device can successfully operate at an elevated temperature.

The high temperature I-V measurement was conducted using the semiconductor characterization system Keithley 4200 – SCS (Figure 4.4.1) and high temperature capability probe station. The devices tested in this experiment are device D8 of sample N7 from wafer

XMK0909 and device A3 of sample M8 from wafer XJH1712. Both of the devices have a gate length and width of 120 µm and 690 µm, respectively. And the distance of source to gate and gate to drain is the same of 10 µm. The devices were tested at temperatures of 25°C, 50°C, 100°C, 150°C, 200°C, 250°C and 300°C.

Figure 4.4.1 Probe station (High temperaure capability, Signatone Model S-1045).

Typical dc output characteristics up to 10 V on the drain and up to -1 V on the gate of device D8 of sample N7 from wafer XMK0909 and device A3 of sample M8 from wafer XJH1712 measured from 25°C to 300°C are shown from Figure 4.4.2 (a) to (g) and Figure 4.4.3 (a) to (g), respectively. Device from wafer XMK0909 showed more drain current than the device from wafer XJH1712 at the same temperature. The specific on resistance of each device at each temperature is calculated and summarized in Table 4.4.1. The specific on resistance of the sample from wafer XMK0909 is smaller than that of the sample from wafer XJH1712. For sample XMK0909 N7 D8, the specific on resistance increase as the temperature rises. The fact that the AlGaN/GaN HEMTs have stable performance at 300°C proves that Ni a reliable gate electrode. Generally, the results of Figure 4.4.2 and Figure 4.4.3 indicate that the round AlGaN/GaN HEMT device can successfully operate at an elevated temperature up to 300°C with minimal degradation, and thus can be used for building high temperature circuits.

To compare I_D at different temperatures, the I_D-V_d characteristics (at zero gate bias) of the AlGaN/GaN HEMT on Si substrate measured from 25°C to 300°C.are plotted in Figure 4.4.4 (a) and (b) for device D8 from sample N7 from wafer XMK0909 and device A3 of sample M8 from wafer XJH1712, repectively. For device D8 of sample N7, at zero gate bias, the drain current achieves 0.01 A/mm at room temperature. At 25°C and 50°C, device A3 achieve full saturation current of about 0.006 A/mm. For both deveces, the drain current decreases as the temperature rises. To investigate the high temperature degradation mechanism, Figure 4.4.5 (a) and (b) shows the temperature dependence of the maximum drain current at V_d=10 V, V_g =0 from device D8 of sample N7 from wafer XMK0909 and device A3 of sample M8 from wafer XJH1712, respectively. For XMK0909 N7 D8, the drain current decreased to less than a third of that at room temperature. The degradation of the drain current at high temperature is due to the decrease of electron velocity. The results show the possibility of the round AlGaN/GaN HEMTs operating at high temperature, over 200°C without external cooling .

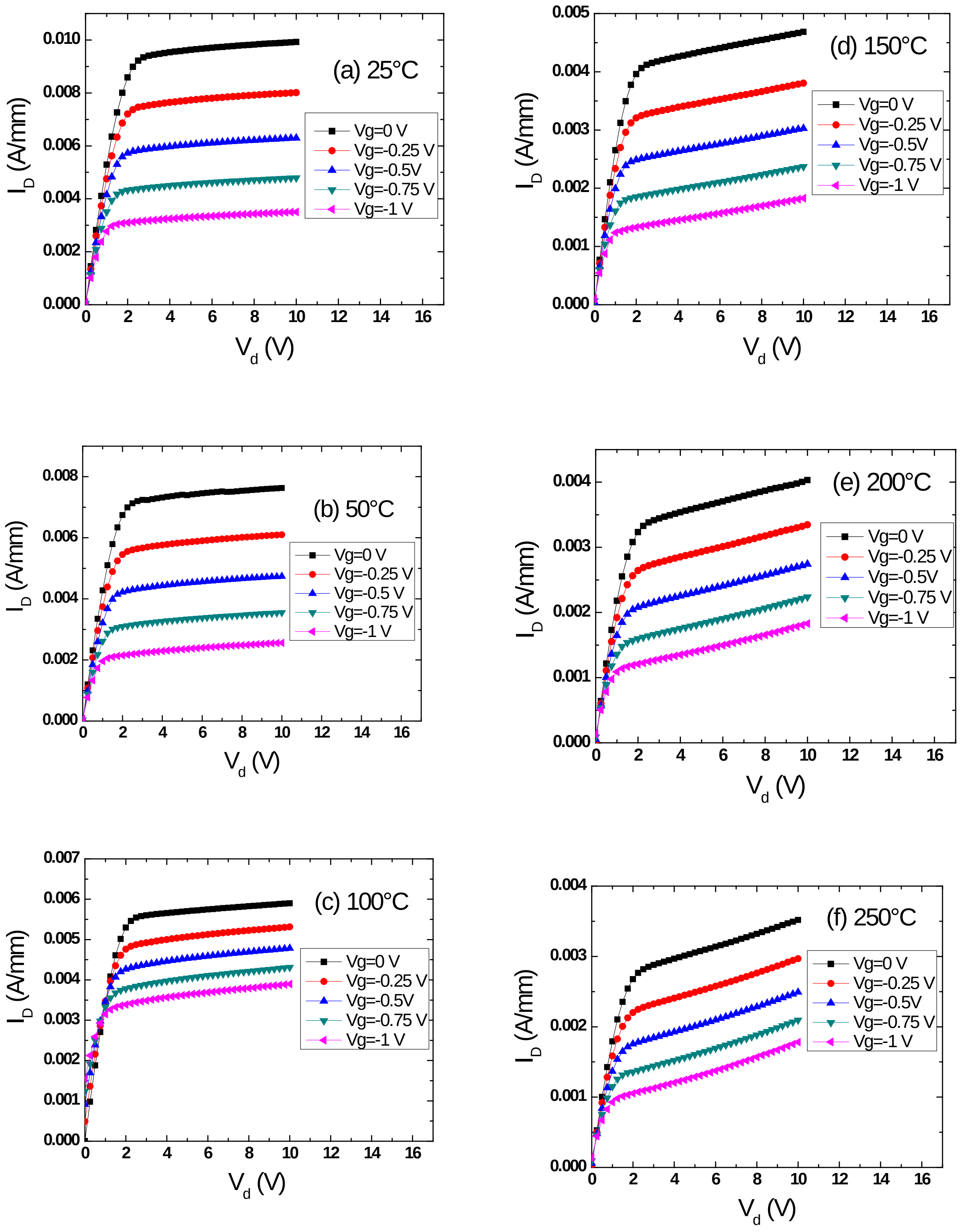
(a) 25°C
0.010
0.008
0.006
0.004
0.002
0.000
I_D (A/mm)
0 2 4 6 8 10 12 14 16
V_d (V)
Vg=0 V
Vg=-0.25 V
Vg=-0.5V
Vg=-0.75 V
Vg=-1 V
(d) 150°C
0.005
0.004
0.003
0.002
0.001
0.000
I_D (A/mm)
0 2 4 6 8 10 12 14 16
V_d (V)
Vg=0 V
Vg=-0.25 V
Vg=-0.5V
Vg=-0.75 V
Vg=-1 V
(b) 50°C
0.008
0.006
0.004
0.002
0.000
I_D (A/mm)
0 2 4 6 8 10 12 14 16
V_d (V)
Vg=0 V
Vg=-0.25 V
Vg=-0.5 V
Vg=-0.75 V
Vg=-1 V
(e) 200°C
0.004
0.003
0.002
0.001
0.000
I_D (A/mm)
0 2 4 6 8 10 12 14 16
V_d (V)
Vg=0 V
Vg=-0.25 V
Vg=-0.5V
Vg=-0.75 V
Vg=-1 V
(c) 100°C
0.007
0.006
0.005
0.004
0.003
0.002
0.001
0.000
I_D (A/mm)
0 2 4 6 8 10 12 14 16
V_d (V)
Vg=0 V
Vg=-0.25 V
Vg=-0.5V
Vg=-0.75 V
Vg=-1 V
(f) 250°C
0.004
0.003
0.002
0.001
0.000
I_D (A/mm)
0 2 4 6 8 10 12 14 16
V_d (V)
Vg=0 V
Vg=-0.25 V
Vg=-0.5V
Vg=-0.75 V
Vg=-1 V

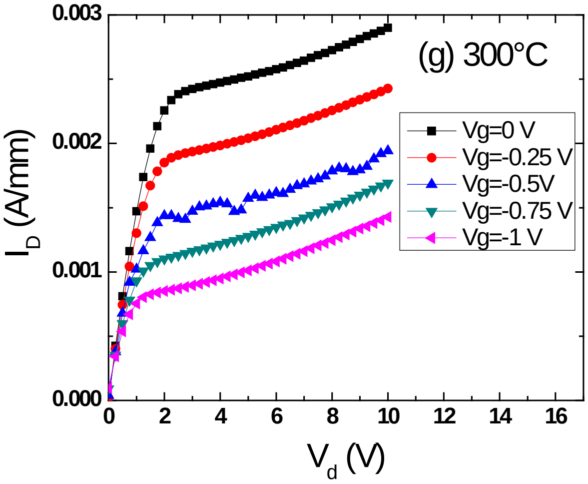

Figure 4.4.2 I_D -V_d characteristics of device D8 of sample N7 from wafer XMK0909 measured at a)25°C, b)50°C, c)100°C, d)150°C, e)200°C, f)250°C and g) 300°C.

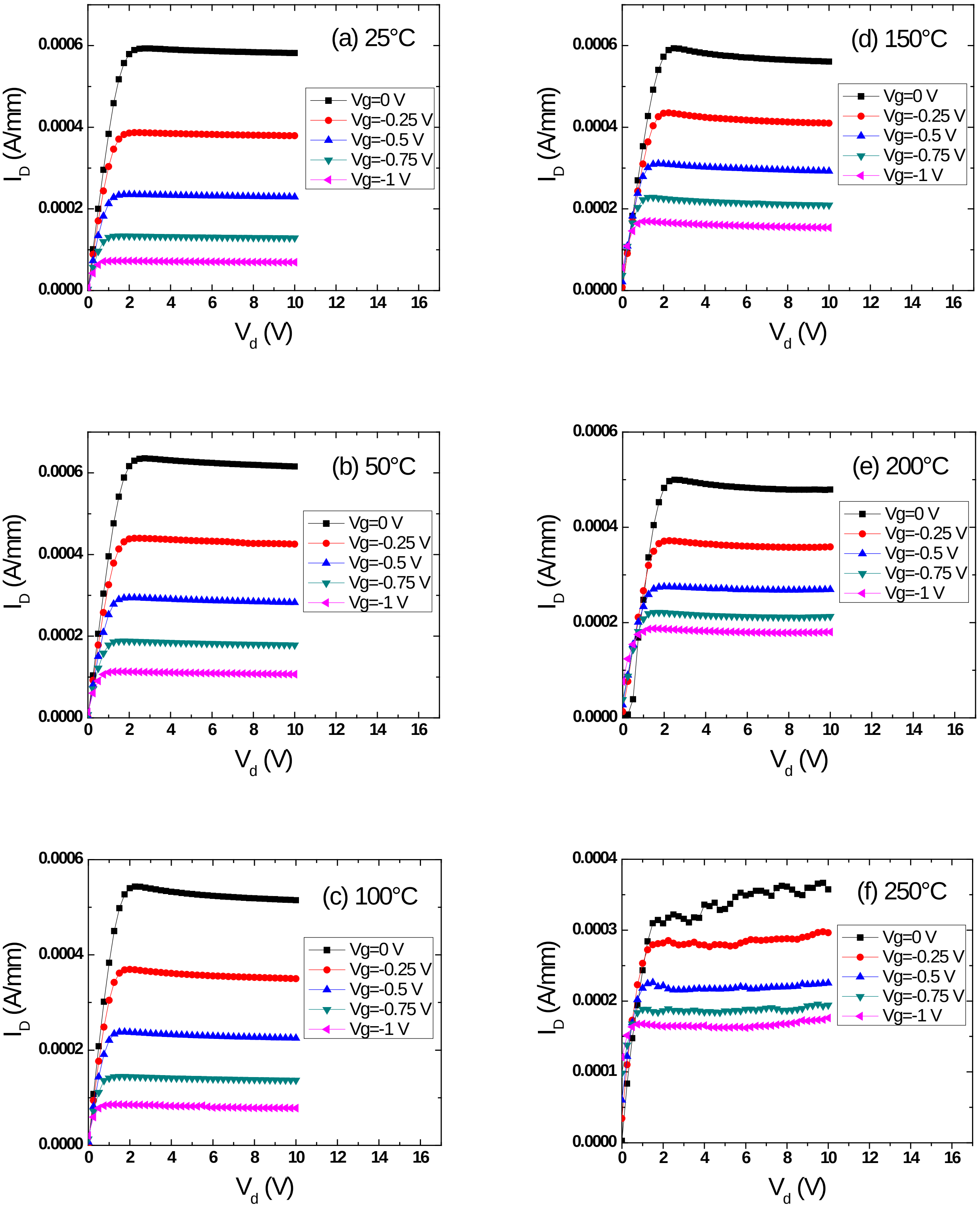
(a) 25°C
(b) 50°C
(c) 100°C
(d) 150°C
(e) 200°C
(f) 250°C
Vg=0 V
Vg=-0.25 V
Vg=-0.5 V
Vg=-0.75 V
Vg=-1 V
I_D (A/mm)
V_d (V)
0.0000
0.0001
0.0002
0.0003
0.0004
0.0006
0
2
4
6
8
10
12
14
16

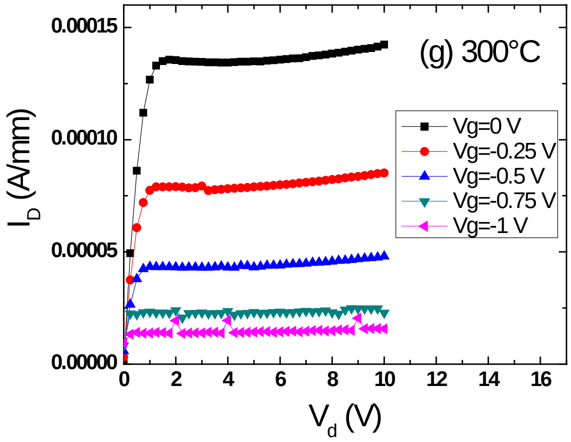

Figure 4.4.3 I_D -V_d characteristics of device A3 of sample M8 from wafer XJH1712 measured at a)25°C, b)50°C, c)100°C, d)150°C, e)200°C, f)250°C and g) 300°C.

Temperature (°C)	**25**	**50**	**100**	**150**	**200**	**250**	**300**
Specific on resistance (Ω-cm^2) XMK0909 N7 D8	0.3	0.4	0.5	0.6	0.7	0.9	1.1
Specific on resistance (Ω-cm^2) XJH1712 M8 A3	4.6	4.5	4.4	5.0	7.4	5.8	9.7

Table 4.4.1 Specific on resistance of the two devices (XMK0909 N7 D8 and XJH1712 M8 A3) measured from 25°C to 300°C.

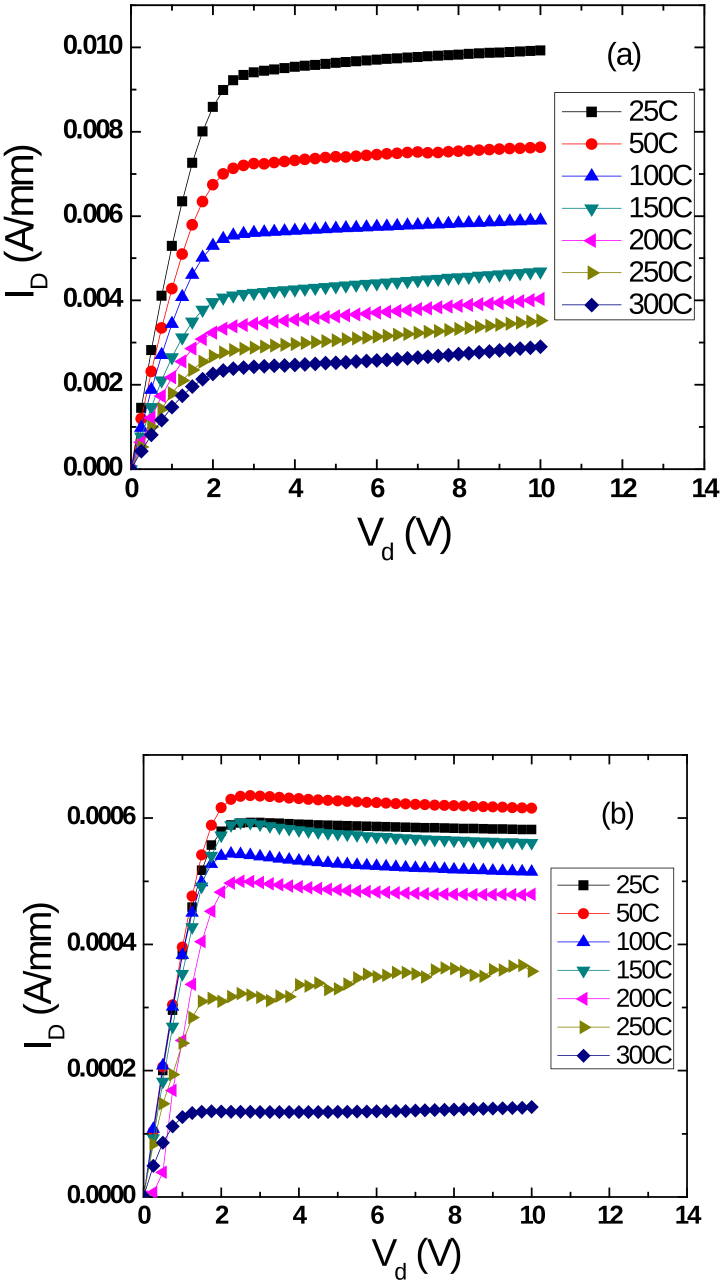

Figure 4.4.4 I_D -V_d (V_g =0) characteristics of (a) device D8 of sample N7 from wafer XMK0909 and (b) device A3 of sample M8 from wafer XJH1712 measured from 25°C to 300°C.

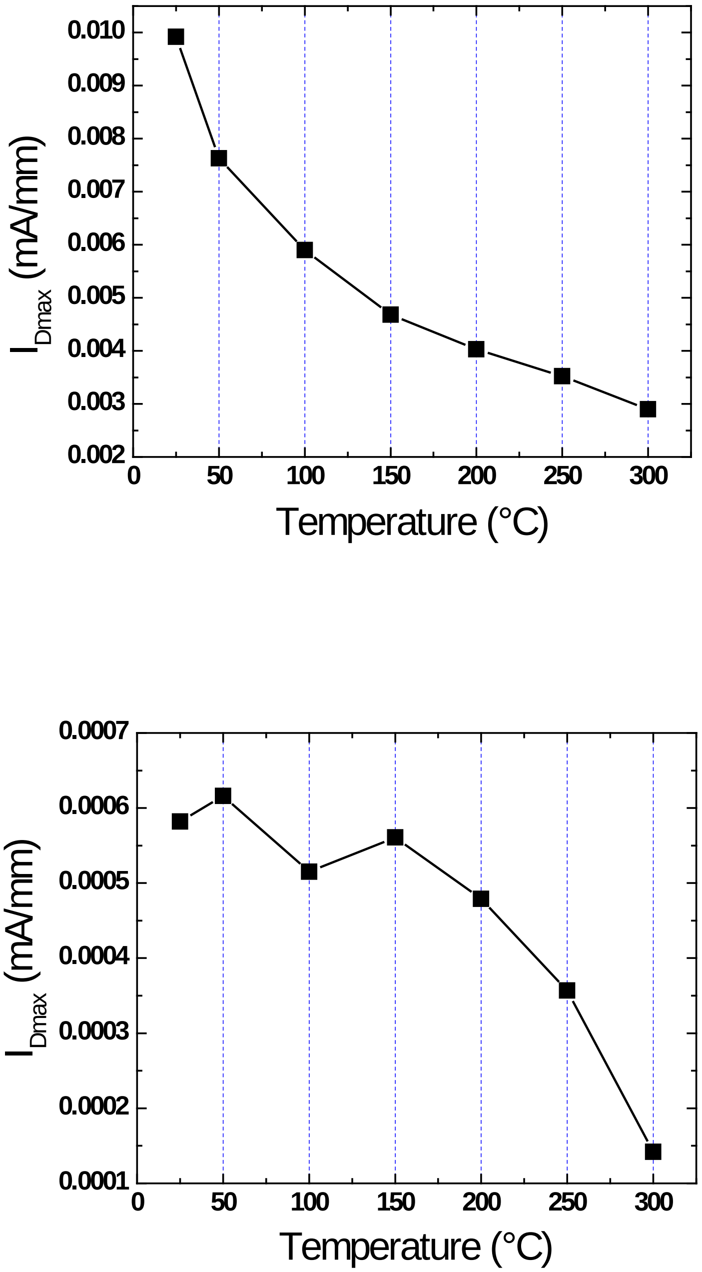

Figure 4.4.5 Temperature dependence of I_{Dmax} at V_d=10 V, V_g =0 from (a) device D8 of sample N7 from wafer XMK0909 and (b) device A3 of sample M8 from wafer XJH1712.

Figure 4.4.6 (a) and (b) shows the Id-Vg and transconductance characteristics of device A3 of sample M8 from wafer XJH1712 measured at different temperatures, respectively. Table 4.4.2 summarises the threshold Voltage and maximum transconductance of the round AlGaN/GaN HEMT measured from 25°C to 300°C. The threshold votage generally shifted more to the negative side as the temperature rises except for at 300°C, which may be due to the degradation of the device. And the maximum transconductance generally decreases as the temperature rises.

Note that the channel length of our testing devices is long at over 10 µm, thus the drain current and transconductance are low. In order to increase transconductance and drain current per gate width, the modification of the design of the HEMT layout: to have shorter effective gate lengths, for example, scaling gate length to approximately 0.5 µm is under way. Marso *et al.*[99] have reported that their RoundHEMT device with 0.2 µm gate length, 100 µm gate width and 2 µm source-to-drain spacing exhibited a drain current of 0.7 A/mm, with a maximal transconductance of 250 mS/mm. The decrease of the electron velocity results in the decrease of the transconductance.

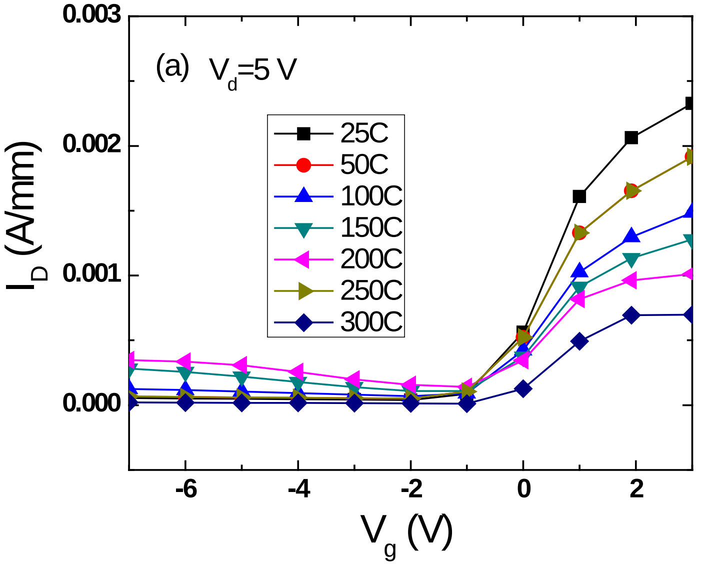

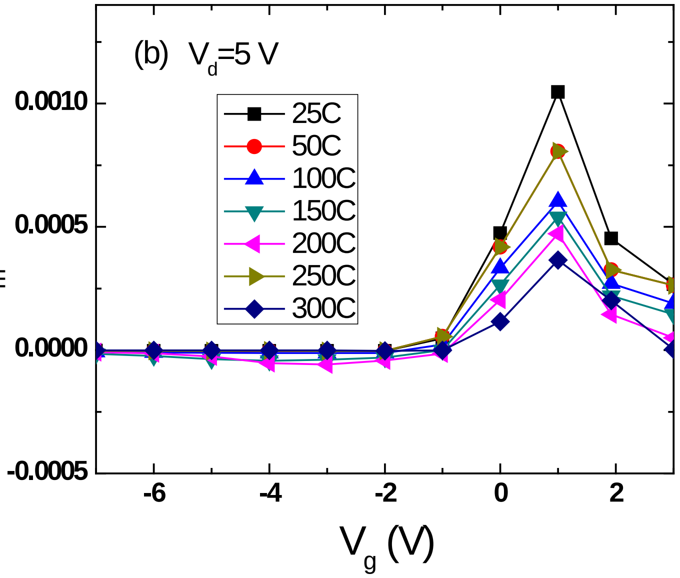

Figure 4.4.6 (a) I_D-V_g (V_d=5 V) and (b) g_m characteristics of the round AlGaN/GaN HEMT (device A3 from sample M8 from wafer XJH1712) measured from 25°C to 300°C.

Temperature (°C)	**25**	**50**	**100**	**150**	**200**	**250**	**300**
Threshold Voltage (V)	-1.15	-1.35	-1.35	-1.4	-1.65	-1.81	-0.74
Max.Transconductance (mS/mm)	0.56	0.41	0.31	0.24	0.27	0.19	0.26

Table 4.4.2 Threshold Voltage and Maximum Transconductance of AlGaN/GaN HEMT (device A3 from sample M8 from wafer XJH1712) measured from 25°C to 300°C.

4.5 Spectroscopic Photo *I-V* Diagnostics

Due to the wide energy band gap (3.4 eV), high critical electric field (4 MV/cm), high electron saturation velocity and many other superior characteristics, GaN and its alloys are considered as a promising material for power electronic device application.[100,101] Recently, great attention has been paid on the fabrication of AlGaN/GaN high electron mobility transistor (HEMT) devices on Si wafer due to the drastic reduction in manufacturing cost and availability of large diameter wafers. However, due to the large mismatch in lattice parameters and thermal expansion coefficients between GaN and Si, it is of necessity to deposit carefully designed multi-layered stress-controlling buffer layers between GaN and Si, which inctoduce additional unwanted interfacial/bulk detects.

One of the phenomena that limits the device performance of the AlGaN/GaN HEMT is so-called "current collapse" which reduces the drain current, thus decreasing the output power.[102,103] It is believed that surface/interface and bulk traps are major culprits to this effect. Therefore, it is of great importance to reduce these surface/interface and bulk traps that will reduce the number of charge carriers in the HEMT channel. In addition, it is very important to reduce the leackage current in the buffer layer to improve the breakdown voltage. To achieve semi-insulating buffer layers, C or Fe doping is often employed.[104,105,106] These compensation doping introduce deep level acceptors in the buffer layer, producing high resistive GaN buffer layers.

One of the analysis techniques which was used to study the deep traps in AlGaN/GaN HEMT system is photoionization spectroscopy. Optical excitation with an above threshold trapping energy photon will release electrons from the trap and the drain current will increase again. By analyzing trapping and detrapping of these charge carriers in the deep traps, the nature of these traps can be elucidated. The details of the photoionization spectroscopy of nitride based transistor were reviewed by Klein *et al*.[107]

In this study, we have proposed a simple diagnostic technique to evaluate the “electrical” homogeneity of the large area AlGaN/GaN HEMT/Si wafer. This method can be considered as a simplified version of photoionization spectroscopy. With further refinement, spectroscopic photo I-V measurement can be employed to diagnose the traps in nitride based HEMT on Si wafers.

The 6” HEMT epitaxy wafer was then diced into individual pieces of dimensions of 1cm × 1cm. As shown in Figure 4.5.1, three pieces which located at the top, center and bottom (bottom substrate is near the major flat of the large area wafer) were selected for this experiment. The HEMT epitaxy wafer pieces were ultrasonically cleaned in the following organic solvents sequentially; acetone, trichloroethylene, acetone, methanol, and methanol for 5 min in each chemical, and finally in boiling hydrochloric acid (HCl) solution. An array of semitransparent circular gate (Ni Schottky contact) with a diameter of 600 μm and thickness of 20 nm were prepared on the surface of the GaN cap layer *via* direct-current (DC) magnetron sputtering. Typical device structure is shown in Figure 4.5.2.

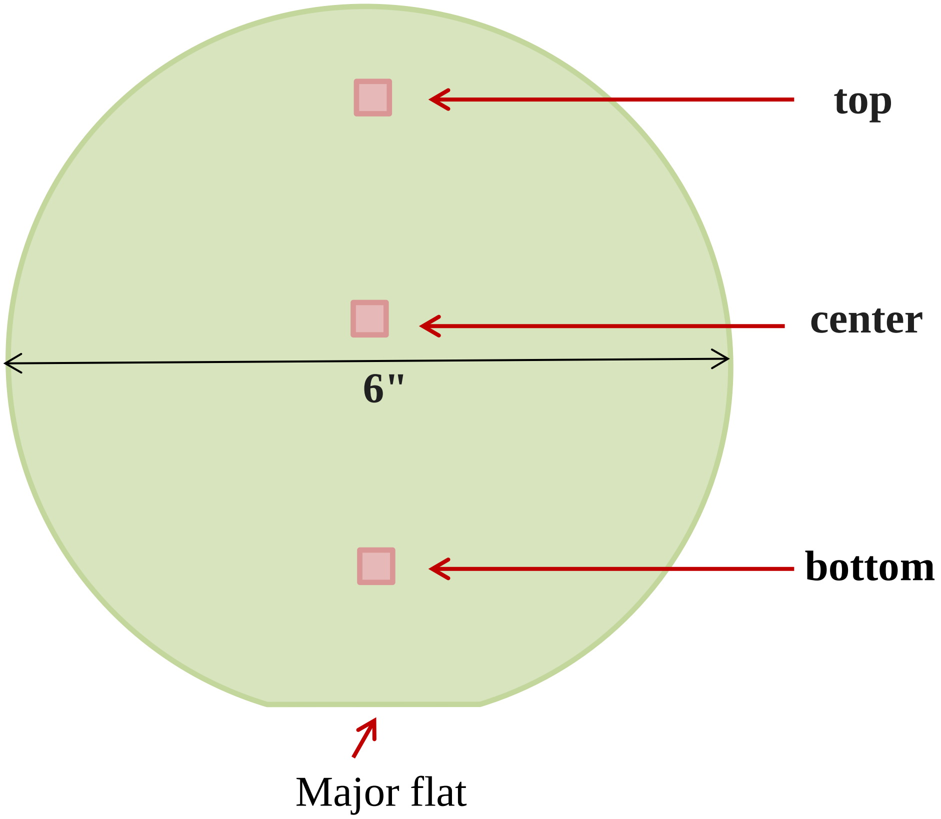

Figure 4.5.1 Schematics of the sample locations on the 6" wafer (not to scale).

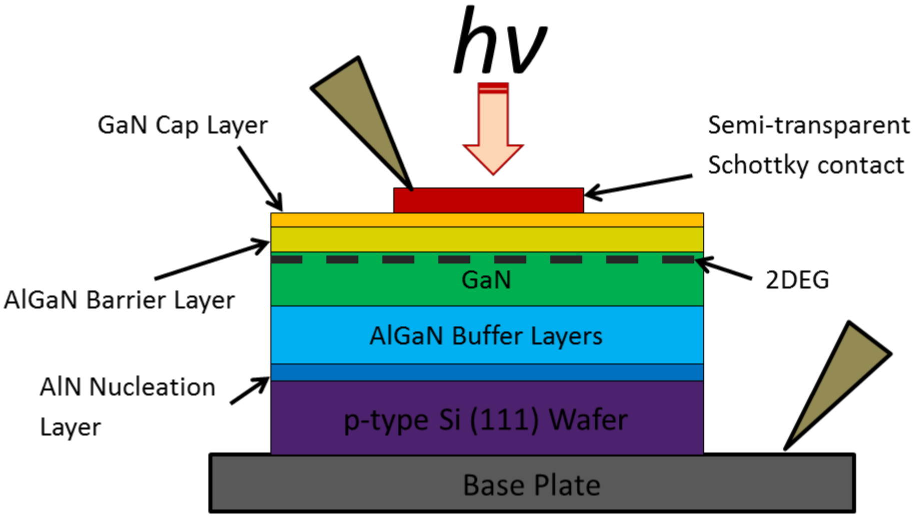

Figure 4.5.2 Schematics of the sample and measurement configuration

Spectroscopic photo *I-V* measurement system, as shown in Figure 4.5.3, is composed of an Apex 150 W Xenon lamp, stepping motor controlled monochromator, Keithley 6487 Pico-ammeter/voltage source, micromanipulator and a computer. Spectroscopic photo *I-V* data were collected from several different region on the 6” wafer. The system was controlled by LabVIEW program. Photocurrent at different excitation wavelength were measured upon sweeping the voltage appled to the device from -20 V to +5 V. The wavelength of the monochromatized light was varied from 800 nm to 400 nm with a step of 50 nm. Since persistent photoconductivity is prevalent in AlGaN/GaN heterostructures,[108, 109] the photo *I-V* was swept from longer wavelength light to shorter wavelength light (800 nm to 400 nm).

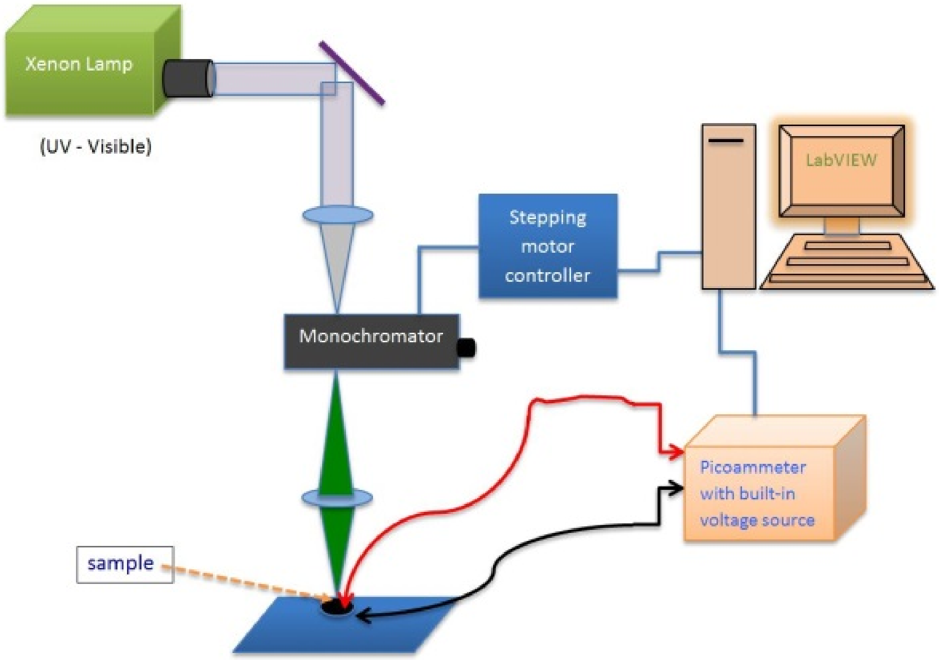

Figure 4.5.3 Schematics of spectroscopic photo I-V measurement system

Figure 4.5.4 shows the spectroscopic photo *I-V* data collected from (a) top, (b) center, and (c) bottom samples of the 6” AlGaN/GaN MOCVD-grown HEMT on Si wafer. Since the dark current level is lower in the reverse bias than that in the forward bias regime, we have focused on the change of photocurrent in the reverse bias region. The photo *I-V* characteristics of the three samples exhibit different spectral response. For the top sample, as shown in Figure 4.5.4 (a), the photocurrent of 800 nm has negligible variance to the dark current; current starting to increase with 750 nm (1.65 eV) and 700 nm (1.77 eV) light illumination, and then gradually decrease in the order of 650 nm, 600 nm, 550 nm, 500 nm, 450 nm and 400 nm. For the center and bottom samples, as shown in Figure 4.5.4 (b) and (c), respectively, photocurrents under 800 nm and 750 nm light illumination are close to the dark current; the photo current starts to increase under 700 nm light illumination and the current jump to the maximum with 650 nm (1.91 eV) light illumination, and then the currents decrease as the illumination wavelength decreases. Top sample shows the maximum photocurrent with the illumination at 750nm while center and bottom samples show the maximum at 650 nm. The spectral response of the photocurrent might be related with energy levels of the responsible traps in epi structures. Surface, interfaces and each layer in the epi structure could be sources for the traps. Khan *et al.*[110] observed the removal of the trapped electrons with the 1.91 eV (650 nm) radiation in their study of the AIGaN/GaN heterostructure insulated gate field effect transistors. DasGupta *et al.*[111] reported the *d*etrapping under monochromatic light near ≈ 1.65 eV (750 nm).

Dark I-V measurements from the three samples show very similar Schottky contact characteristics (data is not shown here) to support that photocurrent changes are not stemmed from contact formation or process variations but can be attributed to local trap variations.

More work is in progress to refine the measurement set-ups and to correlate photocurrent responses to specific trap levels.

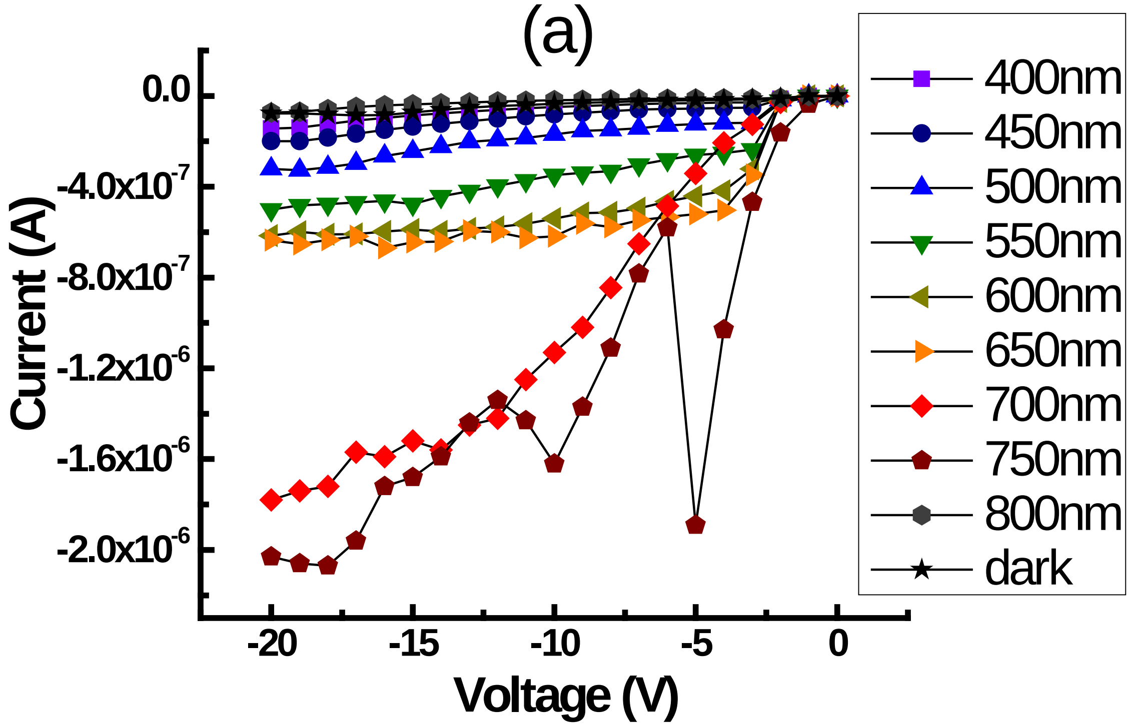
(a)
Current (A)
0.0
-4.0x10^{-7}
-8.0x10^{-7}
-1.2x10^{-6}
-1.6x10^{-6}
-2.0x10^{-6}
-20
-15
-10
-5
0
Voltage (V)
400nm
450nm
500nm
550nm
600nm
650nm
700nm
750nm
800nm
dark

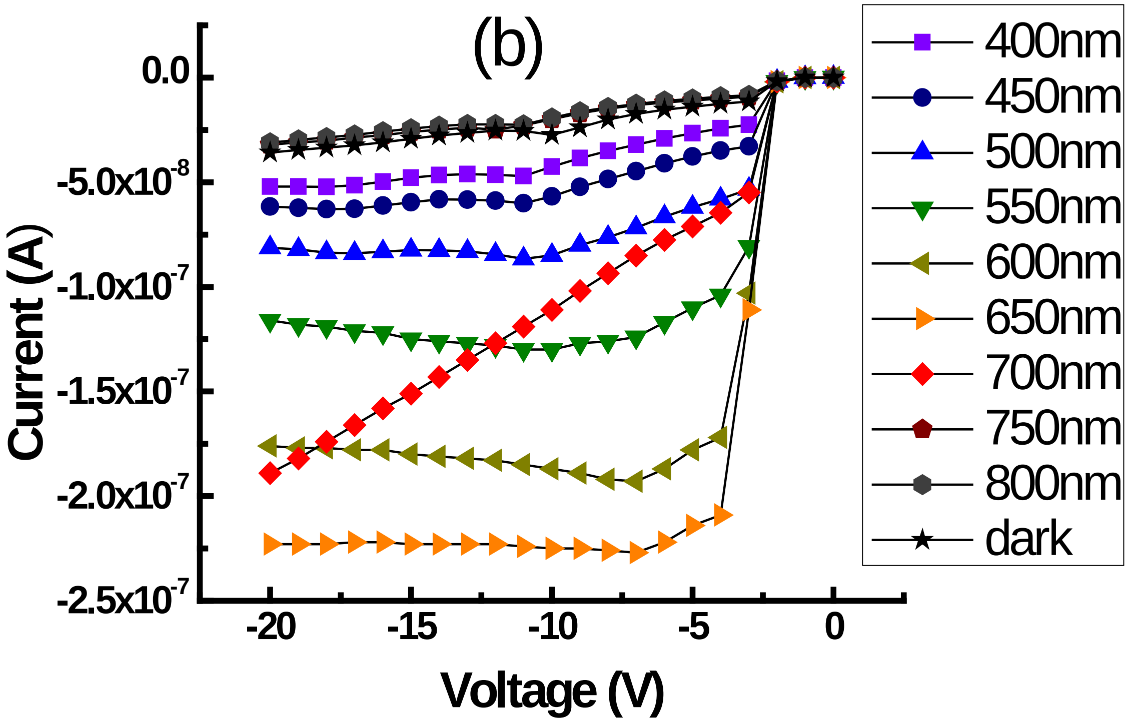
(b)
Current (A)
0.0
-5.0x10^{-8}
-1.0x10^{-7}
-1.5x10^{-7}
-2.0x10^{-7}
-2.5x10^{-7}
-20
-15
-10
-5
0
Voltage (V)
400nm
450nm
500nm
550nm
600nm
650nm
700nm
750nm
800nm
dark

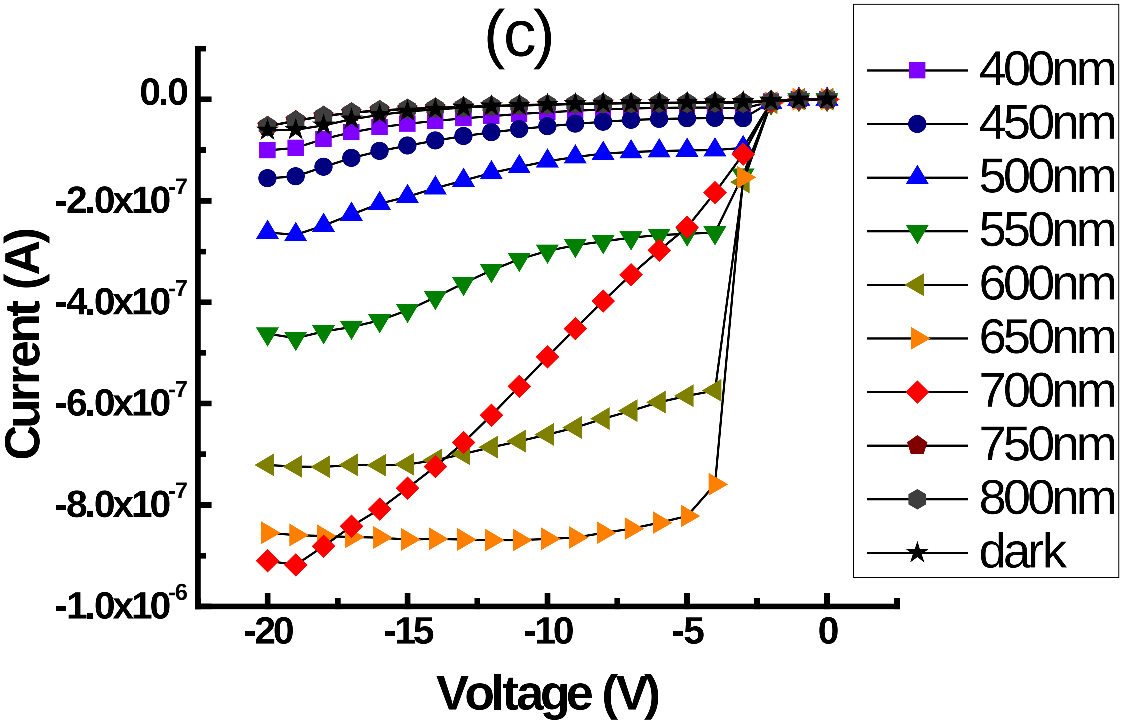

Figure 4.5.4 Spectroscopic photo *I*-*V* data collected from the device from a) top, b) center, c) bottom piece of the 6” HEMT wafer.

4.6 Summary and Conclusions

In summary, fabrication and characterization of the round AlGaN/GaN high electron mobility transistor from various areas of the 6” GaN-on-Si HEMT epitaxy wafer was conducted and the characterization results were analyzed. Detailed micro fabrication techniques including photolithography, sputtering, and rapid thermal annealing was discussed. The result of the *I*-*V*, *C*-*V* and high temperature *I*-*V* was discussed. Moreover, the fabricated round AlGaN/GaN

HEMT device can successfully operate at an elevated temperature up to 300 °C with minimal degradation.

Also, Spectroscopic photo I-V measurements have been applied to the local areas of a 6” GaN-on-Si HEMT epitaxy wafer. The variations of spectral response from different areas of the wafer can be related with local traps across the wafer and the proposed spectroscopic photo I-V test can be useful in diagnosing and characterizing the electrical homogeneity of the HEMT epitaxy wafer with minimum sample preparation steps.

4.7 Future Work

First, it is of great significance to do the optimization of ohmic contact such as Ti/Al/Ni/Au and Ti/Al/Mo/Au of AlGaN/GaN HEMT. For any semiconductor device, contact resistance and semiconductor resistance are the two main resistances. Transmission line method (TLM) is the effective method to investigate the ohmic contact. Secondly, to increase transconductance and drain current per gate width, it would be interesting to modify the design of the HEMT layout: to have shorter effective gate lengths, for example, scaling gate length to approximately 0.5 µm. And the influence of the source-gate distance may be studied. The reduction of drain current at an elevated temperature will be alleviated by process and device design optimization for cap and passivation layers.

Bibliography

---

[1] S.-S. Sun and H. O’Neill, Sunlight Energy Conversion Via Organics Handbook of Photovoltaic Science and Engineering, ed A. Luque and S. Hegedus (Wiley) 2 edition (2011) .

[2] T.A. Skotheim and J.R. Reynolds, Handbook of Conducting Polymers, 3rd edn, CRC Press: Boca Raton, Florida (2007).

[3] M. Pope and C.E. Swenberg, Electronic Process in Organic Crystals and Polymers, Oxford University Press, 2 edition (1999).

[4] N.F. Wannier, Phys. Rev., **52**, 191 (1937).

[5] S. Sun and L. Dalton, “Introduction to Organic Electronic and Optoelectronic Materials and Devices”, CRC Press/Taylor Francis, Boca Raton, Florida (2008).

[6] C.W. Tang, Appl. Phys. Lett. **48**, 183-185 (1986).

[7] W. Ma, C. Yang, X. Gong, K. Lee, A. Heeger, Adv. Funct. Mater. **15**, 1617 – 1622 (2005).

[8] G. Li, V. Shrotriya, J. Huang, Y. Yao, T. Moriarty, K. Emery, Y. Yang, Nature Materials **4**, 864 - 868 (2005).

[9] J.-p. Liu, K.-L. Choy and X.-h. Hou, “Charge transport in flexible solar cells based on conjugated polymer and ZnO nanoparticulate thin films”, J. Mater. Chem. **21**, 1966–1969 (2011).

[10] A. A. D. T. Adikaari, D. M.N. M. Dissanayake and S. R. P. Silva, IEEE J. Sel. Top. Quant. **16,** 201595 (2010).

[11] U. K. Mishra and J. Singh, Semiconductor Device Physics and Design, Springer (2007).

[12] K. Takanezawa, K. Hirota, Q.-S. Wei, K. Tajima, K. Hashimoto, ‘Efficient Charge Collection with ZnO Nanorod Array in Hybrid Photovoltaic Devices”, J. Phys. Chem. **111,** 7218-7223 (2007).

---

[13] P. Ravirajan, A. M. Peiro, M. K. Nazeeruddin, M. Graetzel, D. D. C. Bradley, J. R. Durrant, J. Nelson, “Hybrid Polymer/Zinc Oxide Photovoltaic Devices with Vertically Oriented ZnO Nanorods and an Amphiphilic Molecular Interface Layer”, J. Phys. Chem. B **110,** 7635-7639 (2006).

[14] C.-Y. Chou, J.-S. Huang, C.-H. Wu, C.-Y. Lee, C.-F. Lin, “Lengthening the polymer solidification time to improve the performance of polymer/ZnO nanorod hybrid solar cells”, SOL. ENERG. MAT. SOL. C. **93,** 1608–1612 (2009).

[15] D.C. Olson, J. Piris, R.T. Collins, S.E. Shaheen, D.S. Ginley, Hybrid photovoltaic devices of polymer and ZnO nanofiber composites, Thin Solid Films 496 26–29 (2006).

[16] A. M. Peiró, P. Ravirajan, K. Govender, D. S. Boyle, P. O’Brien, D. D. C. Bradley, J. Nelson and J. R. Durrant, “Hybrid polymer/metal oxide solar cells based on ZnO columnar structures”, J. Mater. Chem. **16,** 2088–96 (2006).

[17] A. Ohtomo, M. Kawasaki, Y. Sakurai, Y. Yoshida, H. Koinuma, P. Yu, Z.K. Tang, G.K.L. Wong, Y. Segawa, Room temperature ultraviolet laser emission from ZnO nanocrystal thin films grown by laser MBE, Mater. Sci. Eng. B **54** (1-2), 24-28 (1998).

[18] M. Godlewski, E. Guziewicz, K. Kopalko, G. Łuka, M. I. Łukasiewicz, T. Krajewski, B. S. Witkowski, S. Gierałtowska, “Zinc oxide for electronic, photovoltaic and optoelectronic applications”, Low Temp. Phys. **37,** 235-240 (2011).

[19] G.-C. Yi, C.R. Wang, W. Il Park, “ZnO nanorods: synthesis, characterization and applications”, Semicond. Sci. Technol. **20**, 22–24 (2005).

[20] K. Yu and J.-H. Chen, “Enhancing Solar Cell Efficiencies through 1-D Nanostructures Nanoscale”, Res. Lett. **4**, 1–10 (2009).

---

[21] L. Baeten, B. Conings, H.-G. Boyen, J. D’Haen, A. Hardy, M. D’Olieslaeger, J. V. Manca, and M. K. Van Bael, “Towards Efficient Hybrid Solar Cells Based on Fully Polymer Infiltrated ZnO Nanorod Arrays”, Adv. Mater. **23**, 2802–5 (2011).

[22] W. I. Park, D. H. Kim, S. W. Jung, and G. C. Yi, “Metalorganic vapor-phase epitaxial growth of vertically well-aligned ZnO nanorods”, Appl. Phys. Lett. **80,** 4232-4234 (2002).

[23] X. Liu, X.-H Wu, H. Cao, and R.P.H. Chang, “Growth mechanism and properties of ZnO nanorods synthesized by plasma-enhanced chemical vapor deposition”, J. Appl. Phys. **95**, 3141-3147 (2004).

[24] K. Ogata, K. Maejima, Sz. Fujita, and Sg. Fujita, “Growth mode control of ZnO toward nanorod structures or high-quality layered structures by metal-organic vapor phase epitaxy”, J. Cryst. Growth **248**, 25-30 (2003).

[25] B.D. Yao, Y.F. Chan, and N. Wang, “Formation of ZnO nanostructures by a simple way of thermal evaporation”, Appl. Phys. Lett. **81,** 757-759 (2002).

[26] Y. Dai, Y. Zhang, Q.K. Li, and C.W. Nan, “Synthesis and optical properties of tetrapod-like zinc oxide nanorods”, Chem. Phys. Lett. **358,** 83-86 (2002).

[27] A.-J. Cheng, Y. Tzeng, Y. Zhou, M. Park, T.-H. Wu, C. Shannon, D. Wang, and W. Lee, “Thermal Chemical Vapor Deposition Growth of Zinc Oxide Nanostructures for Dye Sensitized Solar Cell Fabrication”, Appl. Phys. Lett. **92,** 092113-092115(2008).

[28] Y.-H. Ni, X.-W. Wei, J.-M. Hong, and Y. Ye, “Hydrothermal preparation and optical properties of ZnO nanorods”, Mater. Sci. Eng. B **121,** 42-47 (2005).

[29] L.-B Fan, H.-W. Song, T. Li, L.-X. Yu, Z.-X. Liu, G.-H. Pan, Y.-Q. Lei, X. Bai, T. Wang, Z.-H. Zheng, and X.-G. Kong, “Hydrothermal synthesis and photoluminescent properties of ZnO nanorods”, J. Luminescence **122–123,** 819–821 (2007).

---

[30] D. Polsongkrama, P. Chamninok, S. Pukird, L. Chow, O. Lupan, G. Chai, H. Khallaf, S. Park, and A. Schulte, “Effect of synthesis conditions on the growth of ZnO nanorods via hydrothermal method”, Physica B **403,** 3713–3717 (2008).

[31] H. Ahn, Y. Wang, S. H. Jee, M. Park, Y. S. Yoon, and D.-J. Kim, “Enhanced UV activation of electrochemically doped Ni in ZnO nanorods for room temperature acetone sensing”, Chem. Phys. Lett. 511(4-6) 331-335 (2011).

[32] M. Guo, P. Diao, and S.-M. Cai, “Hydrothermal growth of well-aligned ZnO nanorod arrays: Dependence of morphology and alignment ordering upon preparing conditions”, J. Solid State Chem. **178,** 1864–1873 (2005).

[33] F. Tong, K. Kim, Y. Wang, R Thapa, A. Modic, A. Ahyi, T. Issacs-Smith, J. Williams, H. Ahn, H. Park, D-J Kim, S. Lee, E. Lim, K. K. Lee, and M. Park, “Growth of ZnO nanorod arrays on flexible substrates: Effect of precursor solution concentration”, ISRN Nanomaterials **2012**, 651468, (2012).

[34] O. Ambacher, J. Smart, J. R. Shealy, N. G. Weimann, K. Chu, M. Murphy, W. J. Schaff, L. F. Eastman, R. Dimitrov, L. Wittmer, M. Stutzmann, W. Rieger, and J. Hilsenbeck, “Two-dimensional electron gases induced by spontaneous and piezoelectric polarization charges in N- and Ga-face AlGaN/GaN heterostructures”, J. Appl. Phys. **85**, (1999).

[35] E. T. Yu, X. Z. Dang, P. M. Asbeck, and S. S. Lau, and G. J. Sullivan, “Spontaneous and piezoelectric polarization effects in III–V nitride Heterostructures”, J. Vac. Sci. Technol. B **17** (4), (1999).

[36] P. Lawaetz, “Study of Wurtzite structures”, Phys. Rev. B **5**, 4039 (1972).

[37] A. Bykhovski, B. L. Gelmont, and M. S. Shur, “Elastic strain relaxation and piezoeffect in GaN-AlN, GaN-AlGaN and GaN-InGaN superlattices”, J. Appl. Phys. **81**, 6332 (1997).

---

[38] A. Ozgur, W. Kim, Z. Fan, A. Botchkarev, A. Salvador, S. N. Mohammad, B. Sverdlov, and H. Morkoc, Electron. Lett. **31**, 389 (1995).

[39] M. K. Khan, Q. Chen, M. S. Shur, B. T. Msdermott, J. A. Higgins, J.Burm, W. J. Schaff, and L. F. Eastman, IEEE Electron Device Lett. **17**, 84 (1996).

[40] S. Firoz and R.K. Chauhan, "Comparison of AlGaN/GaN and AlGaAs/GaAs based HEMT device under doping consideration", International Journal of Advances in Engineering & Technology **1** (2), 12-19 (2011).

[41] S. Kato, Y. Satoh, H. Sasaki, I. Masayuki, S. Yoshida, "C-doped GaN buffer layers with high breakdown voltages for high-power operation AlGaN/GaN HFETs on 4-in Si substrates by MOVPE", Journal of Crystal Growth **298,** 831–834 (2007).

[42] E. M. Chumbes, A. T. Schremer, J. A. Smart, Y. Wang, N. C. MacDonald, D. Hogue, J. J. Komiak, S. J. Lichwalla, R. E. Leoni, and J. R. Shealy, "AlGaN/GaN High Electron Mobility Transistors on Si(111) Substrates", IEEE Transactions on Electron Devices, **48** (3) (2001).

[43] B. Lu, E. L. Piner, and T. Palacios, "Breakdown Mechanism in AlGaN/GaN HEMTs on Si Substrate", Device Research Conference (DRC), (2010).

[44] S. Bouzid, V. Hoel, N. Defrance, H. Maher, F. Lecourt, M. Renvoise, D. Smith, and J.C. De Jaeger, "AlGaN/GaN HEMT on Si (111) substrate for millimeter microwave power applications", Advanced Semiconductor Devices & Microsystems (ASDAM), 8th International Conference (2010).

[45] M. Marso, K. Schimpf, A. Fox, A. v. d. Hart, H. Hardtdegen, M. Hollfelder, P. Kordo, and H. Lu¨th, Electron. Lett. **31**, 589 (1995).

---

[46] M. Marso, P. Javorka, A. Alam, M. Wolter, H. Hardtdegen, A. Fox, M. Heuken, P. Kordos, and H. Lüth, “AlGaN/GaN HEMT Optimization Using the RoundHEMT Technology”, phys. stat. sol. (a) **188**, 1, 199–202 (2001).

[47] B. Zimmermann, M. Glatthaar, M. Niggermann, M.K.Riede, A. Hinsch, A. Gombert, Solar Energy Materials &Solar Cells **91,** 374 (2007).

[48] K. L. Chopra, S. Major, and D. K. Pandya, Thin Solid Films **102,** 1(1983).

[49] H. Ahn, Y. Wang, S. H. Jee, M. Park, Y. S. Yoon, and D.-J. Kim, “Enhanced UV activation of electrochemically doped Ni in ZnO nanorods for room temperature acetone sensing”, Chem. Phys. Lett. **511**(4-6), 331-335 (2011).

[50] M. Guo, P. Diao, and S.-M. Cai, “Hydrothermal growth of well-aligned ZnO nanorod arrays: Dependence of morphology and alignment ordering upon preparing conditions”, J. Solid State Chem. **178**, 1864–1873 (2005).

[51] R. D. Tarey, R. S. Rastogi and K. L. Chopra, “Characterization of thin films by glancing incidence X-ray diffraction”, The Rigaku Journal, **4** (1/2), 11 (1987).

[52] Joint Committee on Powder Diffraction Standards, Mineral powder diffraction file: databook: sets 1-42, Powder Diffraction File No. 36-1451.

[53] B. Lo, J.-Y. Chang, A.V. Ghule, S.-H. Tzing, and Y.-C. Ling, “Seed-mediated fabrication of ZnO nanorods with controllable morphology and photoluminescence properties”, Scripta. Materialia. **54,** 411–415 (2006).

[54] J. M. Calleja and M. Cardona, “Resonant Raman scattering in ZnO, Resonant Raman scattering in ZnO”, Phys. Rev B **16,** 3753-3761 (1977).

---

[55] H.C. Hsu, H.M. Cheng, C.Y. Wu, H.S. Huang, Y.C. Lee, W.F. Hsieh, “Luminescence of selective area growth of epitaxial ZnO nanowires and random-growth-oriented nanobelts”, Nanotechnology **17,** 1404-1407 (2006).

[56] R. Cuscó, E. Alarcón-Lladó, J. Ibáñez, and L. Artús, “Temperature dependence of Raman scattering in ZnO”, Phys. Rev. B **75,** 165202 (2007).

[57] A.-J. Cheng, Y.-H. Tzeng, H. Xu, S. Alur, Y.-Q. Wang, M. Park, T.-H. Wu, C. Shannon, D.-J. Kim, and D. Wang, “Raman analysis of longitudinal optical phonon-plasmon coupled modes of aligned ZnO nanorods”, J. Appl. Phys. **105,** 073104 (2009).

[58] E. Alarcón-Lladó, J. Ibánez, R. Cusco, L. Artus, J. D. Prades, S. Estrade, and J. R. Morante, “Ultraviolet Raman scattering in ZnO nanowires: quasimode mixing and temperature effects”, J. Raman Spectrosc. **42,** 153-159 (2011).

[59] Y.H. Tong, Y.C. Liu, C.H. Shao, Y.X. Liu, C.S. Xu, J.Y. Zhang, Y.M. Lu, D.Z. Shen, and X.W. Fan, “Growth and Optical Properties of Faceted Hexagonal ZnO Nanotubes”, J. Phys. Chem. B **110,** 14714 (2006).

[60] A. Umar, B. Karunagaran, E-K Suh, and Y. B. Hahn, “Structural and optical properties of single-crystalline ZnO nanorods grown on silicon by thermal evaporation”, Nanotechnology **17,** 4072–4077 (2006).

[61] S.S. Hong, T. Joo, W.I. Park, Y.H. Jun, and G.C. Yi, “Time-resolved photoluminescence of the size-controlled ZnO nanorods”, Appl. Phys. Lett. **83,** 4157-4159 (2003).

[62] Y. Sun, J.B. Ketterson, and G.K. Wong, “Ecitonic gain and simulated ultraviolet emission in nanocrystalline zinc-oxide powder”, Appl. Phys. Lett.**77** (15), 2322-2324 (2000).

[63] Z.L. Wang, “Zinc oxide nanostructures: growth, properties and applications”, J. Phys. Condens. Matter. **16,** R829–R858 (2004).

---

[64] H.J. Egelhaaf, D. Oelkrug, “Luminescence and nonradiative deactivation of excited states involving oxygen defect centers in polycrystalline ZnO”, J. Cryst. Growth **161**, 190-194 (1996).

[65] D. C. Olson, Y.-J. Lee, M. S. White, N. Kopidakis, S. E. Shaheen, D. S. Ginley, J. A. Voigt and J.W.P. Hsu, “Effect of Polymer Processing on the Performance of Poly(3-hexylthiophene)/ZnO Nanorod Photovoltaic Devices”, J. Phys. Chem. C **111** (44), 16640-45 (2007).

[66] A. J. Moulé, J. B. Bonekamp, and K. Meerholz, “The effect of active layer thickness and composition on the performance of bulk-heterojunction solar cells”, J. Appl. Phys. **100**, 094503, (2006).

[67] C.-K. Lee, C.-W. Pao, and C.-W. Chu, “Multiscale molecular simulations of the nanoscale morphologies of P3HT:PCBM blends for bulk heterojunction organic photovoltaic cells”, Energy Environ. Sci.**4**, 4124-4132 (2011).

[68] P. Ravirajan, A. M. Peiró, M. K. Nazeeruddin, M. Graetzel, D. D. C. Bradley, J. R. Durrant, and J. Nelson, “Hybrid Polymer/Zinc Oxide Photovoltaic Devices with Vertically Oriented ZnO Nanorods and an Amphiphilic Molecular Interface Layer”, J. Phys. Chem. B **110**, 7635-39 (2006).

[69] J.-S. Huang, C.-Y. Chou and C.-F. Lin, “Enhancing performance of organic–inorganic hybrid solar cells using a fullerene interlayer from all-solution processing”, Sol. Energ. Mat. Sol. C. **94,** 182–86 (2010).

[70] C.-T. Chen, F.-C. Hsu, S.-W. Kuan, and Y.-F. Chen, “The effect of C_{60} on the ZnO-nanorod surface inorganic–inorganic hybrid photovoltaics”, Sol. Energ. Mat. Sol. C. **95,** 740-44 (2011).

---

[71] Y.-Y. Lin, Y.-Y. Lee, L.-W. Chang, J.-J. Wu, and C.-W. Chen, “The influence of interface modifier on the performance of nanostrucured ZnO/polymer hybrid solar cells”, Appl. Phys. Lett. **94,** 063308-3 (2009).

[72] Takanezawa K, Tajima K and Hashimoto K Charge Separation Interfaces in Polymer Photovoltaic Devices Hybridized with ZnO Nanorod Arrays Japanese Journal of Applied Physics **47,** 8049–53 (2008).

[73] C.-Y. Chou, J.-S. Huang, C.-H. Wu, C.-Y. Lee, and C.-F. Lin, “Lengthening the polymer solidification time to improve the performance of polymer/ZnO nanorod hybrid solar cells”, SOL. ENERG. MAT. SOL. C. **93,** 1608–12 (2009).

[74] W.-L. Ma, C.-Y. Yang, X. Gong, K. Lee, and A. J. Heeger, “Thermally stable, efficient polymer solar cells with nanoscale control of the interpenetrating network morphology”, Adv. Funct. Mater. **15,** 1617-22 (2005).

[75] G. Li, V. Shrotriya, J-S Huang, Y. Yao, T. Moriarty, K. Emery, and Y. Yang, “High-efficiency solution processable polymer photovoltaic cells by self-organization of polymer blends”, Nat. Mater. **4**, 864-68 (2005).

[76] W. Y. Huang, P. T. Huang, Y. K. Han, C. C. Lee, T. L. Hsieh, and M. Y. Chang, “Aggregation and gelation effects on the performance of poly(3-hexylthiophene)/fullerene solar cells”, Macromolecules **41,** 7485-89 (2008).

[77] V. Shrotriya, Y. Yao, G. Li, and Y. Yang, “Effect of self-organization in polymer/fullerene bulk heterojunctions on solar cell performance”, Appl. Phys. Lett. **89,** 063505 (2006).

[78] J.-P. Liu, K.-L. Choy, and X.-H. Hou, “Charge transport in flexible solar cells based on conjugated polymer and ZnO nanoparticulate thin films”, J. Mater. Chem. **21**, 1966-69 (2011).

[79] S. J. Pearton, J. C. Zolper, R. J. Shul, and F. Ren, J. Appl. Phys. **86**, 1 (1999).

---

[80] W. K. Wang, P. C. Lin, C. H. Lin, C. K. Lin, Y. J. Chan, G. T. Chen, and J. I. Chyi, IEEE Electron Device Lett. **26**, 5 (2005).

[81] H. F. Liu, S. B. Dolmanan, L. Zhang, S. J. Chua, D. Z. Chi, M. Heuken, and S. Tripathy, "Influence of stress on structural properties of AlGaN/GaN high electron mobility transistor layers grown on 150 mm diameter Si (111) substrate", J. Appl. Phys. **113**, 023510 (2013).

[82] H.Harima, J.Phys.: Condensed Matter **14**, 967-982 (2002).

[83] M. Park, J. J. Cuomo, B. J. Rodriguez, W.-C. Yang, R. J. Nemanich, and O. Ambacher, "Micro-Raman study of electronic properties of inversion domains in GaN-based lateral polarity heterostructures", J. Appl. Phys. **93**, 9542 (2003).

[84] J.-Y. Lu, Z.-J. Wang, D.-M. Deng, Y. Wang, K. J. Chen, K.-M. Lau, and T.-Y. Zhang, "Determining phonon deformation potentials of hexagonal GaN with stress modulation", J. Appl. Phys. **108**, 123520 (2010).

[85] C. Kisielowski, J. Kruger, S. Ruvimov, T. Suski, J. W. Ager III, E. Jones, Z. Liliental-Weber, M. Rubin, E. R. Weber, M. D. Bremster, and R. F. Davis, Phys. Rev. B **54**, 17745 (1996).

[86] L.L. Smith, S. W. King, R. J. Nemanich, and R. F. Davis, "Cleaning of GaN surfaces", Journal of Electronic Materials **25** (5), 805-810 (1996).

[87] M. Diale, F.D. Auret, N.G. van der Berg, R.Q. Odendaal, W.D. Roos ,Analysis of GaN cleaning procedures, **246** (1–3) 15 279–289 (2005).

[88] D.-F. Wang, S.-w. Feng, C. Lu, A. Motayed, M. Jah, S. N. Mohammad, K. A. Jones, and L. Salamanca-Riba, "Low-resistance Ti/Al/Ti/Au multilayer ohmic contact to n-GaN", J. Appl. Phys. **89**, 6214 (2001).

---

[89] A.V. Davydov, A. Motayed, W.J. Boettinger, R.S. Gates, Q. Z. Xue, H. C. Lee, and Y. K. Yoo, "Combinatorial optimization of Ti/Al/Ti/Au ohmic contacts to n-GaN", phys. stat. sol. (c) **2** (7), 2551–2554 (2005).

[90] H.-C. Seo, S. Sivaramakrishnan, J.-M. Zuo, L. Pang, P. T. Krein and K. Kim, "Interface analysis of Ti/Al/Ti/Au ohmic contacts with regrown n+-GaN layers using molecular beam epitaxy", Surf. Interface Anal., **43**, 1627–1631 (2011).

[91] X. A. Cao, H. Piao, S. F. LeBoeuf, J. Li, J. Y. Lin, and H. X. Jiang, "Effects of plasma treatment on the Ohmic characteristics of Ti/Al/Ti/Au contacts to n-AlGaN", Appl. Phys. Lett.**89**, 082109 (2006).

[92] A. Vertiatchikh, E. Kaminsky, J. Teetsov and K. Robinson, "Structural properties of alloyed Ti/Al/Ti/Au and Ti/Al/Mo/Au ohmic contacts to AlGaN/GaN", Solid-State Electronics **50,** 1425–1429 (2006).

[93] J. A. Bardwell, S. Haffouz, H. Tang, and R. Wang, "Electrical Characterization and Surface Morphology of Optimized Ti/Al/Ti/Au Ohmic Contacts for AlGaN/GaN HEMTs", Journal of the Electrochemical Society, **153** (8), G746-G749 (2006).

[94] B.C. Joshi, D. Kumar, R. K. Tyagi, and C. Dhanavantri, "Design of Low Threshold Voltage AlGaN/GaN High Electron Mobility Transistors for High Power Switching and Digital Logic Applications", International Journal of Advancements in Technology **1**, (2) (2010).

[95] N. Adachi, Y. Tateno, S. Mizuno, A. Kawano, J. Nikaido, and S. Sano, "High Temperature Operation of AlGaN/GaN HEMT", Microwave Symposium Digest, IEEE MTT-S International (2005).

[96] M. Hatano, N. Kunishio, H. Chikaoka, J. Yamazaki, Z. B. Makhzani, N. Yafune, K. Sakuno, S. Hashimoto, K. Akita, Y. Yamamoto, and M. Kuzuhara, "Comparative high-temperature DC

---

characterization of HEMTs with GaN and AlGaN channel layers”, CS MANTECH Conference, , Portland, Oregon, USA (2010).

[97] Y. Cai, Z. Cheng, Z. Yang, C. W. Tang, K. M. Lau, and K. J. Chen, “High-Temperature Operation of AlGaN/GaN HEMTs Direct-Coupled FET Logic (DCFL) Integrated Circuits”, IEEE Electron Device Letters **28**, 328 (2007).

[98] D. Maier, M. Alomari, N. Grandjean, J.-F. Carlin, M.-A. di Forte-Poisson, C. Dua, A. Chuvilin, D. Troadec, C. Gaquière, U. Kaiser, S. L. Delage, and E. Kohn, “Testing the Temperature Limits of GaN-Based HEMT Devices”, IEEE Transcactions on Device and Materials Reliability **10** (4), (2010).

[99] M. Marso, P. Javorka, A. Alam, M. Wolter, H. Hardtdegen, A. Fox, M. Heuken, P. Kordos, and H. Lu¨th , “AlGaN/GaN HEMT Optimization Using the RoundHEMT Technology”, phys. stat. sol. (a) **188** (1), 199–202 (2001).

[100] A. Ozgur, W. Kim, Z. Fan, A. Botchkarev, A. Salvador, S. N. Mohammad, B. Sverdlov, and H. Morkoc, Electron. Lett. **31**, 389 (1995).

[101] M. K. Khan, Q. Chen, M. S. Shur, B. T. Msdermott, J. A. Higgins, J.Burm, W. J. Schaff, and L. F. Eastman, IEEE Electron Device Lett. **17**, 84 (1996).

[102] S. C. Binari, W. Kruppa, H. B. Dietrich, G. Kelner, A. E. Wickenden, and J. A. Freitas, jr., “Fabrication and characterization of GaN FETs”, Solid-State Electronics **41**, 1549 (1977).

[103] P. B. Klein, S. C. Binari, K. Ikossi, A. E. Wickenden, D. D. Koleske, and R. L. Henry, “Current collapse and the role of carbon in AlGaN/GaN high electron mobility transistors grown by metalorganic vapor-phase epitaxy”, Appl. Phys. Lett. **79**, 3527 (2001).

---

[104] S. Kato, Y. Satoh, H. Sasaki, I. Masayuki, S. Yoshida, "C-doped GaN buffer layers with high breakdown voltages for high-power operation AlGaN/GaN HFETs on 4-in Si substrates by MOVPE", Journal of Crystal Growth **298,** 831 (2007).

[105] S. Haffouz, H. Tang, J.A. Bardwell, E.M. Hsu, J.B. Webb, and S. Rolfe, "AlGaN/GaN field effect transistors with C-doped GaN buffer layer as an electrical isolation template grown by molecular beam epitaxy", Solid-State Electronics **49**, 802 (2005).

[106] Y. C. Choi, M. Pophristic, H.-Y. Cha, B. Peres, M. G. Spencer, and L. F. Eastman, "The effect of an Fe-doped GaN buffer on off-state breakdown characteristics in AlGaN/GaN HEMTs on Si substrate", IEEE Transactions on Electron Dev. **53**, (2006).

[107] P. B. Klein and S. C. Binary, "Topical Review: Photoionization spectroscopy of deep detects responsible for current collapse in nitride-based field effect transistors", J. Phys.: Condens. Matter **15**, R1641 (2003).

[108] E. Arslan, S. Bütün, S. B. Lisesivdin, M. Kasap, S. Ozcelik, and E. Ozbay, "The persistent photoconductivity effect in AlGaN/GaN heterostructures, grown on sapphire and SiC substrates", J. Appl. Phys. **103**, 103701 (2008).

[109] X. Z. Dang, C. D. Wang, E. T. Yu, K. S. Boutros and J. M. Redwing, "Persistent photoconductivity and defect levels in n-type AlGaN/GaN heterostructures", Appl. Phys. Lett. **72**, 25 (1998).

[110] M. A. Khan, M. S. Shur, Q. C. Chen, and J. N. Kuznia, "Current/voltage characteristic collapse in AIGaN/GaN heterostructure insulated gate field effect transistors at high drain bias", Electron. Lett. **30,** 2175–6 (1994).

---

[111] S. DasGupta, M. Sun, A. Armstrong, R. J. Kaplar, M. J. Marinella, J. B. Stanley, S. Atcitty, and T. Palacios, "Slow Detrapping Transients due to Gate and Drain Bias Stress in High Breakdown Voltage AlGaN/GaN HEMTs", IEEE Transactions on Electron Dev. **59** (8), (2012).

APPENDIX

JOURNAL PUBLICATIONS of Fei Tong

1. **F. Tong**, K. Kim, D. Martinez, R Thapa, A. Ahyi, J. Williams, D-J Kim, S. Lee, E. Lim, K. K. Lee, and M. Park, “Flexible organic/inorganic hybrid solar cells based on conjugated polymer and ZnO nanorod array”, Semiconductor Science and Technology **27**, 105005 (2012).
2. **F. Tong**, K. Kim, Y. Wang, R Thapa, A. Modic, A. Ahyi, T. Issacs-Smith, J. Williams, H. Ahn, H. Park, D-J Kim, S. Lee, E. Lim, K. K. Lee, and M. Park, “Growth of ZnO nanorod arrays on flexible substrates: Effect of precursor solution concentration”, ISRN Nanomaterials **2012**, 651468, (2012).
3. R. Thapa, S. Alur, K. Kim, **F. Tong**, Y.Sharma, M. Kim, A. Ahyi, J. Dai, J.W. Hong, M. Bozack, J. Williams, A. Son, A. Dabiran and M. Park, “Biofunctionalized AlGaN/GaN high electron mobility transistor for DNA hybridization detection”, Applied Physics Letters **100**, 232109 (2012).
4. Y. Wang, S. Alur, Y. Sharma, **F. Tong**, R. Thapa, P. Gartland, T. Issacs-Smith, A. Ahyi, J. Williams, M. Park, M. Johnson, T. Paskova, E. A. Preble, and K. Evans, “Ultra-low leakage and high breakdown Schottky diodes fabricated on free-standing GaN substrate”, Semiconductor Science and Technology **26**, 022002 (2011).
5. Y. Wang, H. Xu, S. Alur, Y. Sharma, **F. Tong**, P. Gartland, T. Issacs-Smith, A. Ahyi, J. Williams, M. Park, G. Wheeler, M. Johnson, A. Allerman, A. Hanser, T. Paskova, E. A.

Preble, and K.R. Evans, " Electrical characteristics of the vertical GaN rectifiers fabricated on bulk GaN wafer", Physica Status Solidi C **8**, 2430 (2011).

6. **F. Tong**, Y. Chung, J. Goswami, D.-J. Kim, H. Koo, K. K. Lee, and M. Park, "Surface plasmon properties of DC magnetron sputtered Ag nanoparticles on ITO-PET and ITO-glass substrates", (submitted to Materials Science and Engineering: B).
7. **F. Tong**, C. Yang, C.-K. Jiao, M. Khanal, C. Ahyi, S. Dhar, M. Hamilton, G. Niu, G. Chung, and M. Park, "Spectroscopic Photo-IV Diagnostics of Nitride-based HEMT on Si Wafers", (**accepted** to Electronics Letters).
8. H. Park, **F. Tong**, A. Sujan, Y. Chung, M. Park, B. J. Tatarchuk, H. Koo, H. Ahn, Y. S. Yoon and D.-J. Kim, "Growth of nanostructured ZnO on wearable fabrics for functional garment", (Submitted to Materials Letters).
9. **F. Tong**, D. Wang, M. Hamilton, D.-J. Kim, H. Koo, K. K. Lee and M. Park, "The modification of the refractive index of ZnO nanoparticles doped PEDOT:PSS using both Bruggeman and Maxwell-Garnett model", (In preparation).
10. P. Xu, **F. Tong**, M. Park and M. C. Hamilton "Solution-based fabrication of carbon nanotube bumps for flip-chip interconnects", (In preparation).
11. **F. Tong**, C-W Yang, C. Yang, A. Ahyi, M. Hamilton, G. Niu, G. Chung, and M. Park, "High Temperature Operation of Round AlGaN/GaN High Electron Mobility Transistors on Si(111) Substrates", (In preparation).